Pure hydrogen production by chemical looping technology: use of iron as redox element and bioethanol as renewable reductant

PhD in Chemical Processes for the Industry and the Environment: XXXV cycle

Department of Chemical Engineering Materials and Environment, Sapienza University of Rome

PhD candidate: Martina Damizia

Supervisor:
Prof. Paolo De Filippis

Co-Supervisor:
Prof. Benedetta de Caprariis

A.A. 2021-2022

Content

Abstract

The use of hydrogen as an alternative energy carrier is a promising solution to overcome the global warming issues. Hydrogen is light, storable, energy-dense, and when burned it produces no emissions of pollutants or greenhouse gases. However, since it is not naturally available, the environmental impact of hydrogen is closely linked to the type of source used for its production. The 96% of the commercial H_2, mainly used in chemical and petrochemical sectors, is produced from fossil fuels, resulting globally in 900 Mt of CO_2 per years. The study and optimization of alternative hydrogen production technologies based on renewable sources is therefore essential to make hydrogen a green fuel and to achieve the Zero-Net Emissions target of 2050.

One of the most interesting applications of H_2 as alternative and clean fuel is in the in the automotive sector, which up to now contribute for a large part to global CO_2 emissions. The use of H_2 in the sector of automotive is now possible thanks to the development of Fuel Cells zero-emission vehicles. Among them, Proton Exchange Membrane Fuel Cells (PEMFC) are the most promising one, able to converts the chemical energy of H_2 directly into electricity already at low temperatures, with an efficiency value three times higher than internal combustion engine powered by gasoline. However, for their correct functioning, high purity hydrogen stream is required, with a strict limit on CO concentration (CO<10 ppm), a poison of the Pt-based fuel cell catalyst.

Chemical looping hydrogen (CLH) technology allows the direct production of pure hydrogen in a totally green way. The process is based on the ability of iron oxides to transfer oxygen atoms between a fuel and an oxidant, maintaining constant its activity for high number of redox cycles. The process is composed by two steps: the iron oxides is first reduced to the metal form by feeding a fuel and then Fe is oxidized by steam to produce pure hydrogen and to restore the iron oxides, which participate in a subsequent redox cycle. The absence of purification units makes the CLH process suitable for the decentralized small-scale hydrogen production, solving the issues of hydrogen transportation and storage.

The main purpose of this work is to demonstrate the feasibility of producing pure and green H_2 by a CLH process, suitable to be directly fed to PEMFC, using bioethanol as renewable fuel. The experimental work focused on the synthesis of Fe-based materials, having high activity and high resistance to deactivation, evaluating the process efficiency in a fixed bed bench-scale plant. The influence of the operative conditions on the process efficiency was investigated, focusing the attention on the effect of different redox temperature (675°-750°C) at constant pressure (1 bar) and different flow rate of reductant fuel, with the aim of identifying the optimal conditions.

The thesis is structured into 10 chapters. The first part introduces the issues related to global warming and increased energy demand, mainly based on fossil fuel. Then, chemical looping process is presented

as a promising solution to overcome the criticalities of the use of H_2 as fuel. The second chapter reports the recent advances in scientific literature in the field of CLH technology. Then, in Chapter 3 the experimental set-up and the synthesis methods of the iron-based oxygen carrier are described in detail; the characterization of the synthesized particles is reported in Chapter 4. In Chapter 5 the decomposition of bioethanol is studied to evaluate the feasibility of using it as renewable source of reducing agents; furthermore, tests of CLH are performed on commercial Fe_2O_3 powders aimed at the production of pure hydrogen by monitoring the amount of ethanol fed in reduction. Then, the influence of MnO_2 addition on enhancing the iron oxides reducibility and therefore on the maximization of pure hydrogen yields is studied. In Chapter 6 the experimental results on the use of structural promoters (Al_2O_3, MgO and CeO_2) to improve Fe oxides thermal resistance is deeply investigated focusing the attention on the influence of promoter addition on iron oxide redox activity and on the sample morphology. In Chapter 7 a dedicated study of the couple Fe/Al is performed, evaluating the influence of temperature on the process efficiency values and on Fe/Al interaction. The effect of the addition of Mn oxide to enhance the Fe oxides reduction degree and to avoid the production of hydrogen contaminated by CO, when Al_2O_3 is present as a structural promoter, is investigated in Chapter 8. In Chapter 9 Temperature programmed reduction (TPR) profiles of the most active samples are reported aiming to deeply study the influence of promoters in kinetics of iron oxides reduction and on the iron oxides reduction mechanism. At the end, in Chapter 10, based on the promising results obtained with OCs powders, the use of Fe-based foam, a highly porous materials suitable to be used in fixed bed reactor by keeping low pressure drop is studied with the aim of process scalability.

1. Introduction

Fossil fuel have been powered countries 'economies since the Industrial Revolution and have driven the social and technological progress that followed. From the 1800, their consumption has continuously increased over the time, still supplying 80% of the world's energy needs today [1]. The annual consumption (2021) of fossil fuels for each country, expressed in terawatt-hour (TWh), is shown in Figure 1.0. Excluding the countries for which we have no data, the main fossil fuel consumer is China with 36,223 TWh , followed by United States with 21,017 TWh used and Russia with a 7,557 TWh [2].

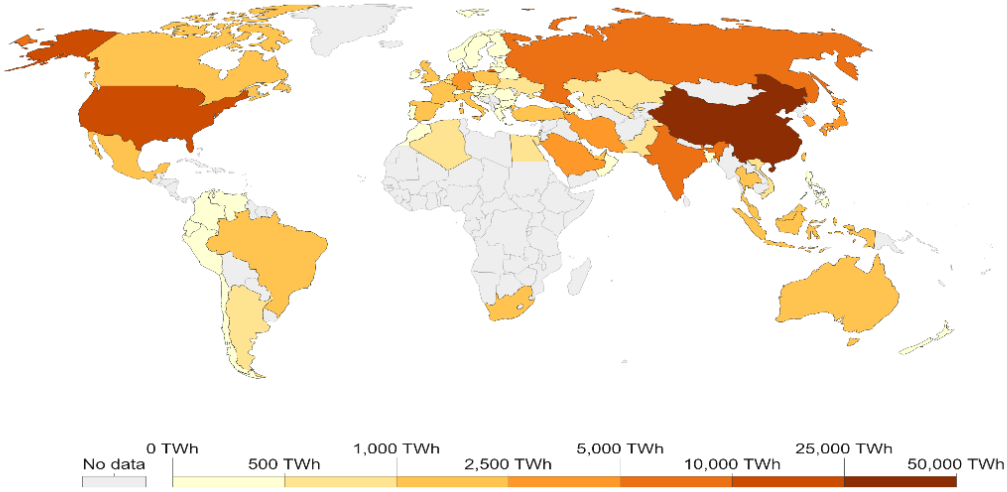

***Figure 1.1**:Annual Fossil fuel consumption in each country, 2021 [1].*

The extensive exploitation of fossil fuels over the last century has led to 2 criticalities which cannot be longer ignored: the shortage of the reserves and the impact of greenhouse gases emissions, resulted from their utilization on the planet [3][4].

The limited aviability of fossil fuels is not only linked to their non renewable nature, but also to the high rate of fossil fuels consumption reached today [5]. The trend of global evolution of coal, oil and gas consumption, in the period of time 1800-2021, is reported in Figure 1.2. In the early 1800s wood , the only energy sources for century, was replace by coal and later by oil and gas. The exploitation rate of fossil fuels was limited until the coal age, but whit the spread over of oil and gases (1950th), there was a rapid increase in consumption of fossil fuels. Today, coal consumption is falling in many parts of the world, but the oil and gas are still growing quickly [6].

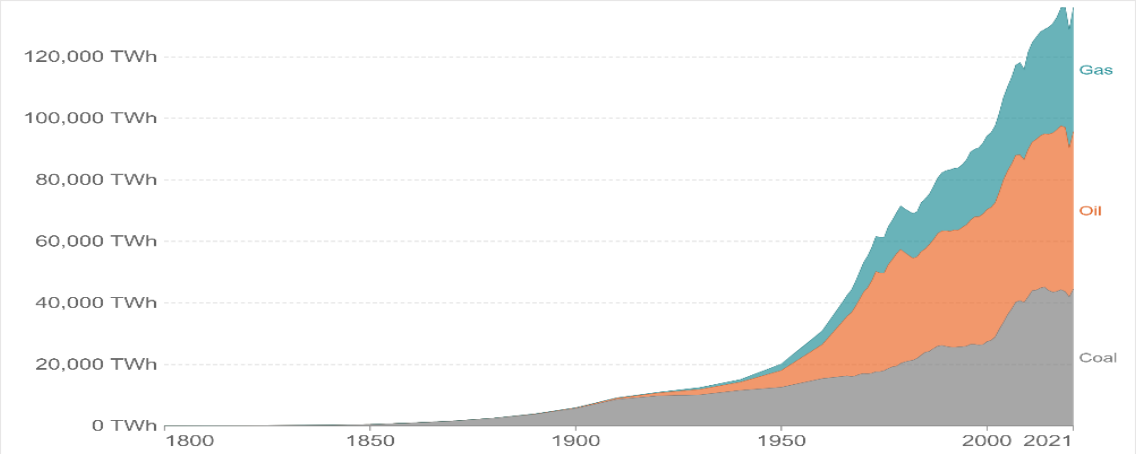

Figure 1.2: *Global fossil fuel consumption, period of time 1800-2021* [5]

Considering this aspect, already in the 1970s some analysts had said that "Peak Oil" would occur, due precisely to the fact that oil extraction could not continue to increase at this rate. The term "Peak Oil" was used as early as 1956 by the US geophysicist Marion King Hubbert, who was looking for a model to predict the temporal evolution of the production of any mineral resources. According to Hubbert's model, Peak Oil is reached when the quantity of oil that can be extracted can no longer increase but slowly declines [7]. However, new drilling techniques and the exploitation of new materials such as "*oil shale*" and "*gas shale*", have made it possible to successfully offset the current low yields of the well-known deposits. These solutions seem promising to overcome the scarcity of oil reserves but they could led to an increase in the cost of production and to a concrete high risk of environmental and ecological impact [8].

The second issue which require an urgent solution is the impact of using fossil fuels on the environment. Fossil fuels combustion is responsible for 3/4 of the total greenhouse gases emissions, with a negative effect on the climate change and human health [9]. The estimated consequences of global warming range from increasing sea levels, greater risks of weather extremes such as tornados or tsunamis, droughts, crop failure and dramatic changes of ecosystems [10].

Figure 1.3 shows the evolution trend of the annual carbon dioxide emissions for the main fossil fuels consumers [11]. The CO_2 emission profile follows the same trend of fossil fuel consumption (Figure 1.2), with the highest emission rate registered in the period 1950-today. United States, Russia and European Union have seen a decrease in CO_2 emission in the recent years while the CO_2 emissions for China are still in growing, with approximately 10 billion of tons of CO_2 produced in 2020.

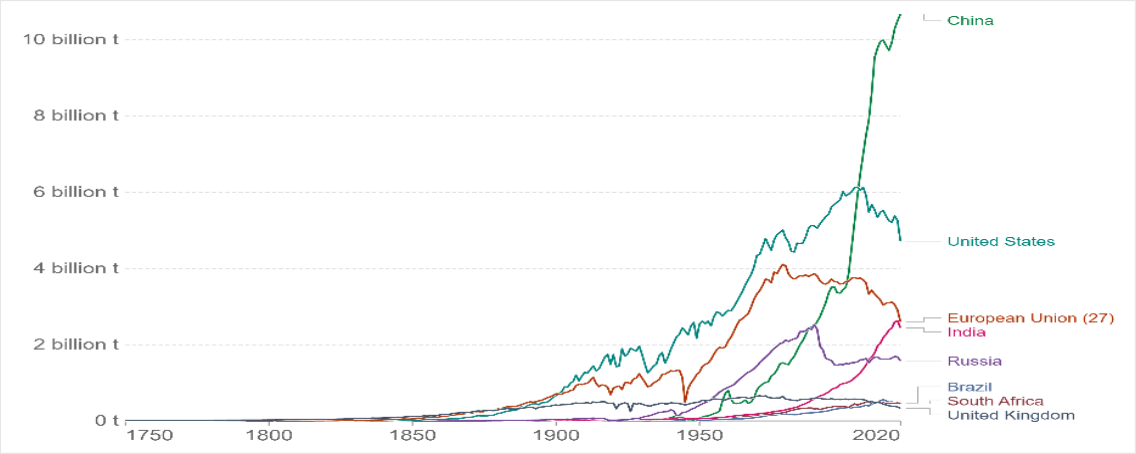

Figure 1.3 *Annual CO_2 emissions by countries (1170-2021)*[11].

To mitigate the effect of global warming, the Intergovernmental Panel on Climate Change (IPCC), the United Nations body for assessing the science related to climate change, has established different ad-hoc objectives and working groups, aimed at reducing global greenhouse gases emissions [12]. Among them, one of the main tasks is to limit the global warming to < 2°C of the preindustrial era.

Two courses of action have been proposed, which can substantially contribute to the reduction of greenhouse gases emissions:

1) the addition of carbon capture units in an energy system still based on fossil fuels.

2) the replacement of fossil fuels with renewable ones, rely mostly on wind, solar and biomass.

Both proposed pathways are not mutually exclusive but instead are intertwined and thus should be pursued jointly.

The construction of an energy system able to work with many types of energy sources like coal, oil, gas, nuclear, hydropower, solar, wind and biofuels is the main challenge of the near future. In fact, if we look back a couple of centuries ago, our energy mixes where relatively homogeneous and the transition from one source to another was incredibly slow. We have seen that, until the mid-19th century, the burning of solid fuels such as wood, crop waste, or charcoal was the dominant source of energy used across the world and only since the Industrial Revolution has come the rise of coal followed by oil, gas. At the early of the 20th century the use of hydropower energy began, and it wasn't until the 1960s that nuclear energy was added to the mix. The 'modern renewables', as solar and wind, were only added much later, in the 1980s. The speed and scale of the energy transition we need today in switching from fossil fuels to low-carbon energy is therefore a new challenge, very different from the past.

Looking at the 2020 energy scenario of the International Energy Agency (IEA) statistics (Figure 1.4) still only 17% (including 4.8% nuclear) of the total energy production currently does not rely on carbonaceous fuels, confirming the huge efforts needed to achieve a decarbonization.

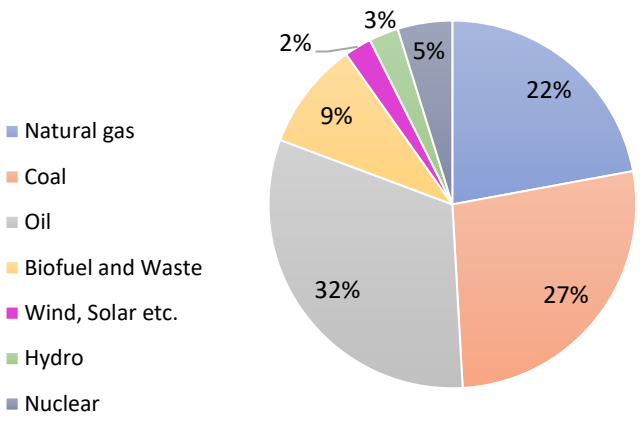

Figure 1.4: *World Primary Energy Supply (2020)* [13][14].

Hydrogen and energy have a long-shared history, powering the first internal combustion engines over 200 years ago and becoming an integral part of the chemical industry, where is used in many processes (Figure 1.5 b)[15][16]. Hydrogen demand in 2020 was approximately 90 Mt, with more than 70 Mt used as pure H_2 in Oil refining/Ammonia production and less than 20 Mt mixed with carbon-containing gases in methanol production/steel manufacturing. Oil refining is the largest consumer of hydrogen today with close to 40 Mt consumed in 2022. The H_2 total estimated value of the market is $ 115 billion, and it is expected that it will only grow, reaching $ 155 billion by the end 2022 [17].

Nowadays, H_2 plays a key role in the energy transition scenario, becoming one of the most promising energy vector to achieve the energy decarbonization, usable in many sectors including automotive [18][19][20]. It recognized as technically viable and benign energy vector useful in many types of application, ranging from small scale off-grid power supply to large scale energy exports. It is light, storable, energy-dense, and when burned it produces no emissions of pollutants or greenhouse gases[21]. Its utilization in the automotive sector is promoted by the development of fuel cells, especially Proton Exchange Membrane Fuel Cell (PEMFC) that allow the conversion of the chemical energy of H_2 pure into electricity with high efficiency (60%, compared to 33% of traditional engines).

However, H_2 does not exist in nature as pure and therefore its environmental impact is defined by the resources used for its extraction (Figure 5.4 a) [22]. The 96% of the commercial H_2 is still produced from fossil fuels, resulting in close to globally 900 Mt of CO_2 emissions per years [17] [23].

a)

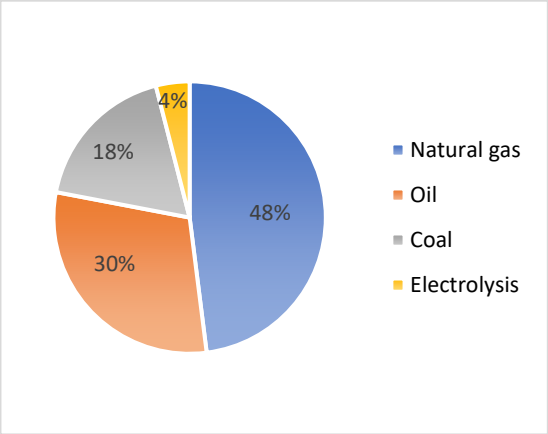

b)

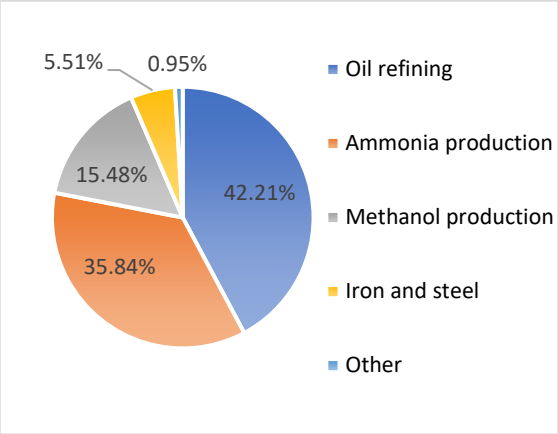

***Figure 1.5**:H_2 production sources (a) and H_2 uses(b)*

The steam methane reforming is currently the most common application used to produce H_2, having the highest hydrogen yield of the three possible ways to produce H_2 at industrial scale (1 steam methane Reforming; 2 Oil partial oxidation; 3 Coal gasification).

The flow diagram of the process aimed to produce H_2 pure is reported in Figure 1.6.

Natural gas and steam are fed to the pre-reformer where the heavies are converted to methane to prevent soot and enhance the efficiency of the process [24]. More steam is added prior to entering the main reactor, where syngas is produced, in an equilibrium-limited endothermic reaction (reaction 1)[25].

The reactor comprises of a radiant and convective section. The radiant segment contains reaction tubes and burners utilizing natural gas and PSA tail gas as fuel. Flue gas leaving the radiant section enters the convection section for heat recovery. To maximize hydrogen production, subsequent equilibrium-controlled, exothermic water-gas shift (WGS, reaction 2) reaction is carried out:

SMR	$CH_4 + H_2O \leftrightarrow CO + 3H_2$	ΔH= +206 kJ/mol	(1)
WGS	$CO + H_2 \leftrightarrow CO_2 + H_2O$	ΔH= -41 kJ/mol	(2)

While the WGS reaction equilibrium favours low temperatures, reaction rates are faster at high temperatures. Therefore, in most industrial applications, WGS comprises of two-steps: high temperature (HT) and low temperature (LT) shift reactions. Shifted syngas undergoes separation to obtain H_2 pure.

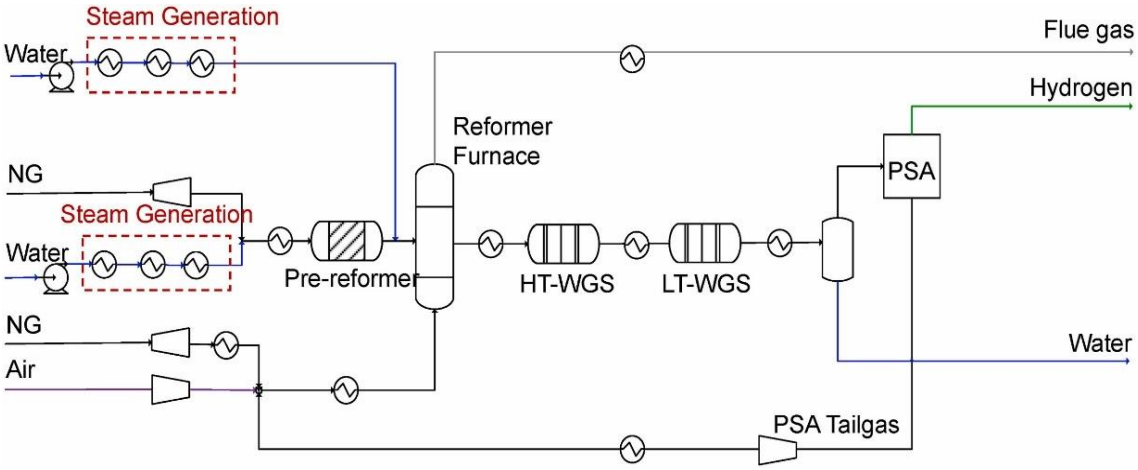

***Figure 1.6** : Steam Methane reforming process, flow diagram*[22]

Small scale H_2 production plants utilize pressure-swing adsorption (PSA) technology for hydrogen separation and purification [26]. This can be attributed to its relatively low capital and operating costs, and high-purity hydrogen production [27]. The PSA consists of parallel adsorbers running under cyclic operation [28]. Hydrogen flows through the adsorption columns, while CO_2 and other impurities are adsorbed. Lowering the pressure inside the column to atmospheric conditions allows impurities to be desorbed, thereby producing high purity hydrogen. PSA tail gas, comprising primarily of unreacted methane, CO and CO_2, is burnt with supplementary natural gas to provide fuel for the reactor furnace[29] .

Thus, to reduce the carbon footprint of H_2 is fundamental to connect its production to renewable sources, moving from grey H_2 (from fossil) to blue (with carbon capture) and green H_2 (from renewable sources)[30].

Global interest in green hydrogen is increasing, especially after the recently concluded 26th UN Climate Change Conference of the Parties (COP26), a climate change summit hosted by UK in Glasgow (2021). Countries that have pledged net-zero carbon emissions look at green hydrogen as the fuel that will help achieve the goal. However, the use of green hydrogen, faces an economic barrier due to its higher cost compared with unabated fossil-based hydrogen. The net H_2 cost is primarily driven by the natural gas prices (Table 1.0), which results in significant deviations between global markets. Hydrogen production cost range from 0.8 €/ kg_{H2} to 2.0 €/kg_{H2}[31][32] .

***Table 1-1**: Levelized H_2 production cost by Steam Methane Reforming [33].*

Resources	**Cost Contribution ($/ kg H_2)**
Natural gas price	$ 0.89
Catalysts	$0.01
Net Utilities	$0.06
Labour and Supplies	$ 0.08
Other Costs	$ 0.33
Net Cost	**$ 1.25**

The recent spike in natural gas prices could have made green hydrogen cheaper than grey hydrogen. For example, the cost of production of grey hydrogen in the United Kingdom has increased from $1.9 per kg in April 2021 to $8 per kg in October 2021, while the cost of green hydrogen remained unchanged at $4.5 per kg[34][35].

With the aim to use H_2 as alternative clean energy vector in sectors traditionally powered by fossil fuels (such as automotive) a significant contribution to the H_2 final cost is also given by the distribution and storage logistic. Actually, H_2 is produced by centralized steam methane reforming plant and therefore is should be transported over long distances by trucks/pipelines and stored on-site in huge quantities For transportation purposes between the production plants and the filling or distribution stations, the gaseous hydrogen (GH_2) is usually compressed up to 500 bars or liquefied (LH_2 at -253°C). However, maintaining LH_2 at such a low temperature is probably the main challenge of cryogenic hydrogen storage. Liquefaction is both time and energy consuming, and up to 40% of energy content can be lost in the process (compared to about 10% energy loss in the compressed GH_2). Thus, this storage method is most often used for medium to large-scale storage and delivery such as intercontinental hydrogen shipping. In the case of GH_2, it is stored and transported by trucks or delivered via pipeline systems at 30 bar. The comparison of GH_2 cost contributions of transportation by trucks or via a pipeline system as function of the distance are reported in figure 1.7[36].

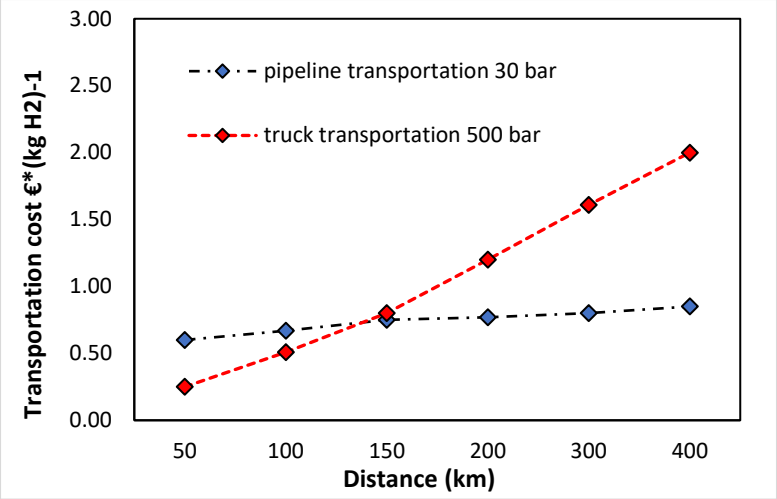

***Figure 1.7**: Transportation cost of GH_2, truck versus pipeline.*

GH_2 delivery by truck transportation is viable only over short distances and in rural areas where the hydrogen demand is low. A pipeline distribution system is the most reasonable solution but requires an initial high investment and high market demand. However, it excels in delivering high amounts of gas over long distances and in areas with a well-developed infrastructure [37].

The costs for gas compression to the final filling pressure of approximately 900 bar lies within the range of 0.5 €·$(kg_{H2})^{-1}$. On-site storage costs are in the range of 0.09 – 0.29 €·$(kg_{H2})^{-1}$, which incorporate a buffer to compensate for potential supply interruption.

Thus, the hydrogen distribution for mobile applications is dominated by two critical segments: the gas distribution and the hydrogen storage systems. According to a study on hydrogen infrastructure for mobility these two segments contribute to more than 60% of the investment costs for hydrogen filling stations, and thus should be the focus for technological improvements[38].

In conclusion, a restructuring of the energy production and distribution logistics can significantly accelerate the market penetration of hydrogen as an energy carrier, enabling a fast transition from the fossil fuels to a sustainable zero carbon emission energy market.

A promising approach to remodelling the fuel distribution infrastructures reducing, at the same time, the GHG emissions, is the decentralized green hydrogen production. A decentralized, on-demand hydrogen production can greatly promote the decarbonized hydrogen production chain, by eliminating the H_2 transposition over long distances and the need to store large amounts of hydrogen on-site [39]. One of the decentralized hydrogen solutions may still rely on conventional steam reforming of local available renewable resources, producing a hydrogen rich synthesis gas, followed by a two-step WGS reaction. However, in this process the produced hydrogen is diluted with CO_2 and, in the ideal case of pure methane as the hydrocarbon feedstock, the produced gas consists of 80 vol% H_2 (15 wt%) and 20 vol% CO_2 (85 wt%). Furthermore, for applications that need H_2 pure (e.g. automotive with PEMFC),

its necessary to implement an additional purification step in the process (PSA). Thus, the decentralization of the traditional steam methane reforming technology suffers from a substantial loss in efficiency, declining from 70 – 85% to 51% in the decentralized purposed, resulting in high production costs.

As an alternative decentralized proposal, small-scale chemical looping hydrogen (CLH) appears as a very promising technology to produce directly pure hydrogen in a totally green way.

The process was subjected to an extensive evaluation of the thermodynamic potential and experimental tests for process development aimed to offers the perspective of a decentralized, on-demand, emission-free hydrogen production starting from renewable feedstock (e.g. syngas from biomass gasification, biogas, bio-oil and bioethanol). Bioethanol is one of the most interesting renewable sources of reducing agents, already produced from sugar or starch- containing crops by an industrially well-established technique. It is a stable and non-toxic liquid at ambient conditions [40] [41] and therefore its distribution, storage, and commercialization are easy and economic.

This technology enables:

- the production of environment-friendly hydrogen utilizing renewable resources, aimed to decrease the global CO_2 emissions
- The direct production of pure H_2 eliminating the purification cost, traditionally present in the SMR plant.
- Decentralized production small scale plant aimed at reducing the hydrogen transportation and storage demand, lowering the total production costs.

CLH is a cyclical process that allows the direct production of pure H_2 exploiting the redox activity of transition metals. The metal oxide is first reduced to the metal form by a fuel, which is oxidized with the lattice oxygen of the metal oxide. Later, the reduced metal reacts with steam producing H_2 and restoring the metal oxide, which participates in a new redox cycle. The chemical looping system can be composed by two or three interconnected reactors with fluidized or fixed reactive bed, composed by the transition metal. When Iron is used, the process is also called Steam Iron Process (SIP). The raw iron oxides, generally hematite (Fe_2O_3) is reduced by syngas/carbon action to Fe through several reactions (reaction 3-10).

$3Fe_2O_3 + H_2 \rightleftarrows 2Fe_3O_4 + H_2O$ $\Delta H_{900°C}$ = -7.175 kJ/mol (3)

$3Fe_2O_3 + CO \rightleftarrows 2Fe_3O_4 + CO_2$ $\Delta H_{900°C}$ = -41.09 kJ/mol (4)

$3Fe_2O_3 + C \rightleftarrows 2Fe_3O_4 + CO$ $\Delta H_{900°C} = +50.09$ kJ/mol (5)

$Fe_3O_4 + H_2 \rightleftarrows 3FeO + H_2O$ $\Delta H_{900°C} = +\ 50.61$ kJ/mol (6)

$Fe_3O_4 + CO \rightleftarrows 3FeO + \ CO_2$ $\Delta H_{900°C} = +15.70$ kJ/mol (7)

$Fe_3O_4 + C \rightleftarrows 3FeO + CO$ $\Delta H_{900°C} = +40.61$ kJ/mol (8)

$FeO + H_2 \rightleftarrows Fe + H_2O$ $\Delta H_{900°C} = +15.03$ kJ/mol (9)

$FeO + CO \rightleftarrows Fe + CO_2$ $\Delta H_{900°C}$ = -19.88 kJ/mol (10)

$FeO + C \rightleftarrows Fe + CO$ $\Delta H_{900°C} = +30.61$ kJ/mol (11)

At the end of the reduction step steam is fed to iron, aimed to produce magnetite (Fe_3O_4) and H_2 pure (reactions 11-12). The oxidation of Fe_3O_4 by steam to the original oxide (Fe_2O_3) is not thermodynamically feasible and required the introduction of an additional air oxidation step (reaction 12).

$Fe + H_2O \rightleftarrows FeO + H_2$ $\Delta H_{900°C}$ = -95.6 kJ/mol (11)

$3FeO + H_2O \rightleftarrows Fe_3O_4 + 4H_2$ $\Delta H_{900°C}$ = -55.6 kJ/mol (12)

$4Fe_3O_4 + O_2 \rightleftarrows 6Fe_2O_3$ $\Delta H_{900°C}$ = -485.2 kJ/mol (13)

SIP is one of the oldest commercial methods for producing hydrogen and it was practiced from the early 1900s until about 1930, to produce small quantities of pure hydrogen, intended for use of aerospace. Later this technology was supplanted by the more efficient steam methane reforming process.

Today SIP is attracting new interest for the green H_2 production thanks to the increasing of pure H_2 demand and to the development of Proton Exchange Membrane Fuel Cells (PEMFC), efficient device to produce electricity, intended for automotive applications.

The main drawbacks of pure H_2 production by CLH system is the low thermal stability of iron at repeated redox cycle and the carbon deposition during the reduction step when a carbonaceous reductant

is used. The reduction of iron oxides by carbon is favoured by thermodynamics at the operative conditions needed for the process but own very low kinetics in the range of temperature of 650-900°C; if carbon is not fully consumed during the reduction, at the beginning of the oxidation step, it reacts with steam producing additional H_2 but also CO, producing H_2 contaminated by CO.

Several works are already published about the hydrogen production by CLH process focused on the use of renewable reductant to produce environmental-friendly H_2 and on the tailored synthesis of Fe-based material able to resist at high temperature. However, most of them prove the feasibility of the technology without produce H_2 pure. Furthermore, the use of bioethanol as a renewable reductant is still not fully exploited. Thus, the literature lacks a comprehensive knowledge on the pure H_2 production from bioethanol from experimental and modelling point of view.

1.1 Thesis objectives

The main goal of this work is to demonstrate the feasibility of producing pure and green H_2 by a Chemical Looping Process, with a hydrogen purity compatible to the use in PEMFCs (CO<10 ppm). Iron is chosen as low cost and environmentally safe redox material while bioethanol as renewable fuel. Bioethanol is already produced at industrial scale from renewable sources (biomass) through a mature technology (alcoholic fermentation). Furthermore, it is liquid and stable at ambient conditions and therefore easily to transport and to store. These features contribute to the success of the proposed technology especially for a possible scale-up as the renewable source used is already efficiently produced and commercialized.

The experimental work focused on the synthesis of new and high resistance Fe-based materials having high activity and high resistance to deactivation and on the evaluation of the process feasibility in a fixed bed bench scale plant. The influence of the operative conditions on the process efficiency was investigated, focusing the attention on the effect of different redox temperature (675°-750°C) at constant pressure (1 bar) and on the different flow rate of reductant fuel with the aim of identifying the optimal conditions.

The specified objectives of the study are presented below:

- Production of pure hydrogen from ethanol and commercial $Fe_2O_{3,,}$ optimization of the iron oxides reduction degree to avoid the carbon deposition during the reduction step.
- Synthesis of Fe-based oxygen carriers owing high resistance to deactivation for several consecutive redox cycles in high temperature conditions. Investigation of the chemical interaction between Fe and the structural promoters (Al_2O_3, MgO and CeO_2).

- Optimization of the process temperature (675°C-750°C) to obtain high Fe-based particles activity with high thermal stability to maximize the pure H_2 yields.
- Addition of Mn_xO_y to the Fe redox system to enhance Fe-based material activity avoiding coke deposition.
- TPR analysis of the Fe-based samples aimed to investigate the influence of the structural promoters in the kinetic of iron oxides reduction.
- Evaluation of Fe-based foam activity in the system to be used in a possible scale-up of the process.

The work presented in this thesis has been published in peer-reviewed journals as follows:

- *de Caprariis, B., Damizia, M., De Filippis, P., Bracciale, M.P*.

The role of Al_2O_3, MgO and CeO_2 addition on steam iron process stability to produce pure and renewable hydrogen (2021) International Journal of Hydrogen Energy, 46 (79), pp. 39067-39078.

- *De Filippis, P., D'Alvia, L., Damizia, M., de Caprariis, B., Del Prete, Z.*

Pure hydrogen production by steam-iron process: The synergic effect of MnO2 and Fe2O3(2021) International Journal of Energy Research, 45 (3), pp. 4479-4494.

- *Damizia, M., Bracciale, M.P., de Caprariis, B., Genova, V., De Filippis, P*.

High thermal stability Fe_2O_3-Al_2O_3 system to produce renewable pure hydrogen in steam iron process (2021) Chemical Engineering Transactions, 86, pp. 547-552

- Damizia M, Bracciale M.P. de Caprariis B., De Filippis P.

Efficient utilization of Al_2O_3 as structural promoter of Fe into 2 and 3 steps chemical looping hydrogen process: pure H_2 production from ethanol (submitted to Fuel).

- *Bracciale M., Damizia, M., De Filippis P., de Caprariis B.*

Clean Syngas and Hydrogen Co-Production by Gasification and Chemical Looping Hydrogen Process Using MgO-Doped Fe_2O_3 as Redox Material (2022), Catalyst, 12(10), 1273.

2. Recent Advances in Chemical Looping technologies for H_2 production

2.1 Introduction

Chemical looping hydrogen represents a promising technology enables the direct production of H_2 pure in a totally renewable way. The process is based on the ability of a metal oxides to be reduced and oxidized cyclically maintaining constant its activity for high number of redox cycles. Specifically, CLH consist into 2 spatially and temporary separated steps: the metal oxide is reduced by a fuel and then oxidized by steam producing H_2 and restoring the metal oxides, useful in the next redox cycle. Considering the role of the metal oxide in the process, it is generally called Oxygen Carrier (OCs). The OCs are usually applied to transfer oxygen from the gaseous oxygen source to the fuel, avoiding the direct contact of these two reactants and hence decreasing the energy penalty of separation.

The concept of chemical looping was introduced in the 19th century (Figure 2.1) with the development of an air separation process by Quentin and Arthur Brin [42]. In the Brin process, the equilibrium of the couple BaO/BaO_2 ($BaO+½\ O_2 \rightleftharpoons BaO_2$) is variated by temperature and pressure swings. During 1886–1906, the Brin's Oxygen Company used this method to isolate O_2, although it was later superseded by the fractionation of liquid air [43].

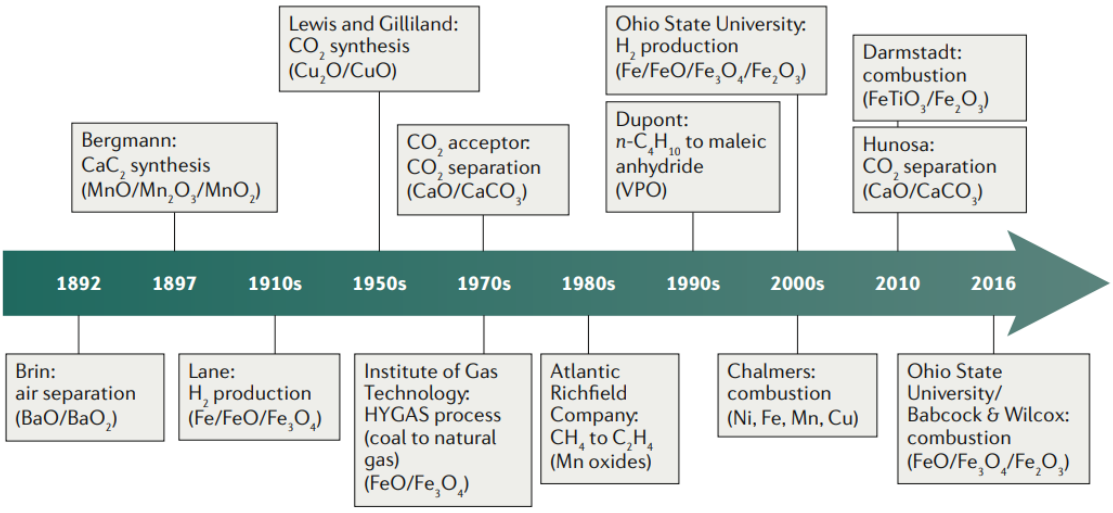

Figure 2.1 *Development in chemical looping technologies* [44].

The chemical looping process for hydrogen generation was first introduced by Howard Lane as the "Lane Hydrogen Producer" in 1903, which used syngas from coal gasification as reducing agent and iron as redox element, in a fixed bed reactor. The process enables the production of 200 m^3 of H_2 per

ton of coke in a cyclical operation mode at 750°C, with an H_2 purity in the range of 95.0-99.0 %. This system was filed for patent in 1911 by Messerschmitt under the name "steam-iron process" (SIP)[45][46]. The steam-iron process was successfully used for the commercial hydrogen supply in the first quarter of the 20th century but eventually it was replaced by the more cost competitive steam reforming process of methane. Although the technology never again reached a commercially competitive status in the second part of the last century, researches on the technology of hydrogen production by redox reaction of solid OCs continued successfully. Encouraging results were published, however due to economic considerations the SIP never again progressed beyond testing operation. Today the "steam-iron process", it is usually referred to as a modification of the chemical looping combustion process (CLC) and is thus named "chemical looping hydrogen" (CLH), "chemical looping water splitting" (CLWS) or "cyclic water gas shift" (CWGS).

Chemical Looping Combustion (CLC) is considered one of the most promising loop cycle, widely studied because of its ability to perform an efficient fuel combustion easily capturing the CO_2 emissions [47]. The fuel combustion is broken down into 2 spatially and temporary separated steps : the reduction of the metal oxide via reaction with the fuel and the oxidation by air of the reduced metal (reactions 2.0 and 2.1, respectively) [48]. The fuel oxidation performed in the fuel reactor (FR) produces CO_2 and H_2O, and a clean CO_2 stream can be achieved by steam condensation, without the use of additional energy for separation. The oxidation step performed in the Air reactor (AR) produces a nitrogen stream and restore the metal oxide, needed for the subsequent fuel oxidation [44][48][49]. A simplified scheme of a chemical looping process is reported in Figure 2.2.

FR $$\left(2x+\frac{y}{2}-z\right)MO + C_xH_yO_z \rightarrow \left(2x+\frac{y}{2}-z\right)M + xCO_2 + \frac{y}{2}H_2O \quad (2.0)$$

AR $$M + Air \rightarrow MO + N_2 \quad and\ unreacted\ O_2 \quad (2.1)$$

Overall Reaction $$C_xH_yO_z + Air \rightarrow xCO_2 + \frac{y}{2}H_2O + N_2 \quad and\ unreacted\ O_2 \quad (2.2)$$

Looping media: M⇋MO where M is a transition metal oxide.

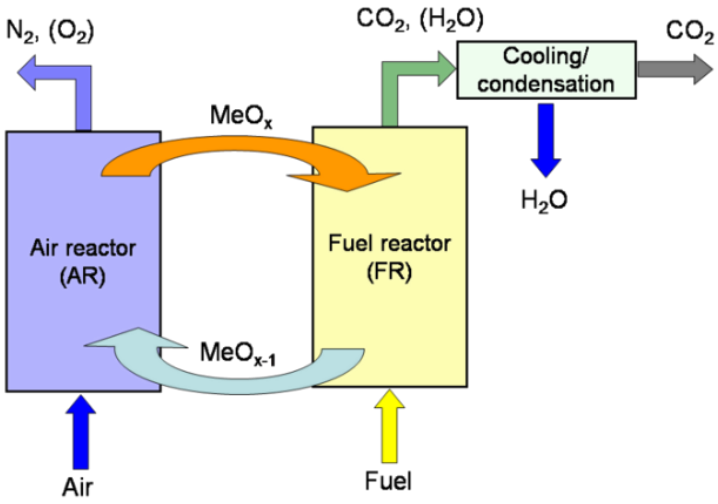

***Figure 2.2**: Simplified scheme of CLC with CO_2 capture.*

Chemical Looping reforming (CLR) utilizes the same basic principles as chemical-looping combustion, with the difference that the desired product is not heat but syngas (i.e. a gas mixture consisting mainly of H_2 and CO). In the CLR system, the fuel is partially oxidized into CO e H_2 by the lattice oxygen of the metal oxides, which is restored in the subsequent oxidation step by air (Figure 2.3). Steam or CO_2 could be added to the fuel to enhance the relative importance of steam reforming (reaction 2.5) or CO_2 reforming reaction (reaction 2.6), respectively. This could be useful if synthesis gas with a H_2/CO ratio that does not correspond to the H/C ratio of the fuel is desired. The addition of Steam or CO_2 also suppress the formation of solid carbon via reactions 2.7 and 2.8., which potentially could become an obstacle at under stoichiometric conditions

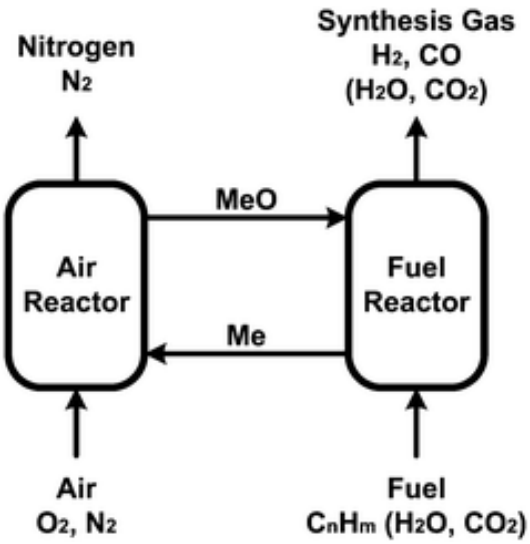

***Figure 2.3**: Simplified scheme CLR process.*

Steam reforming	$C_nH_m + nH_2O \rightleftarrows nCO + (n + \frac{1}{2}m)H_2$	(2.5)
CO_2 reforming	$C_nH_m + CO_2 \rightleftarrows 2nCO + \frac{1}{2}mH_2$	(2.6)
Boudouard	$2CO \rightleftarrows C + CO_2$	(2.7)
Cracking	$C_nH_m \rightleftarrows nC + \frac{1}{2}mH_2$	(2.8)

Over the last decades, the increased pure H_2 demand involved a renewed interest on CLH process. Currently, several configurations of the CLH system were proposed which includes fluidized and fixed bed configuration. In CLH system the steam oxidation step follows the metal reduction in order to produce a pure H2 stream by water splitting. The addition of an air oxidation step at the end of the steam oxidation is also widely studied to improve the fuel conversion into CO_2 and H_2O and to solve the issues of carbon deposition in the presence of carbonaceous reductants (Figure 2.4).

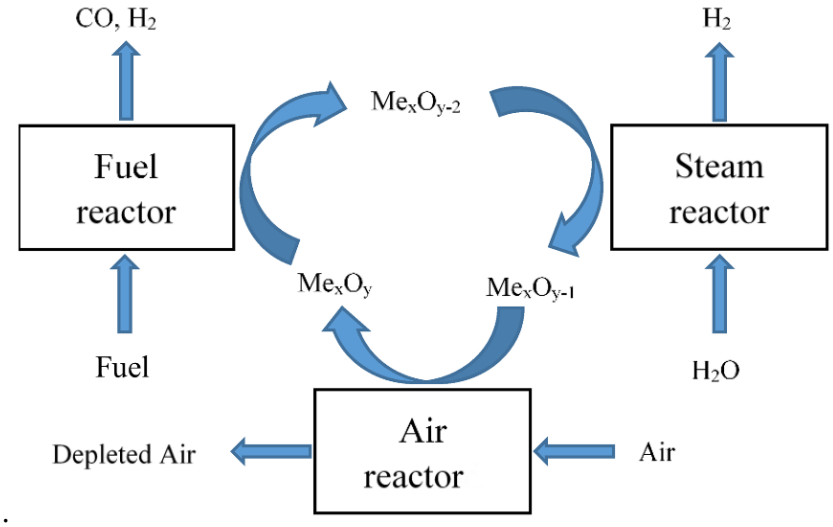

***Figure 2.4**: Process schematic of CLH with the addition of an air oxidation step.*

This chapter surveys the very recent research data and scientific achievements presented in literature about hydrogen production by Chemical looping technologies aimed to produce H2 pure (CLH) or a mixture of H_2 and CO (CLR). The publications results were divided into five main sections: OCs design, reactor design, process development, process simulation and kinetic studies

2.2 OCs Design

The oxygen carrier functions as a transport intermediate to deliver pure oxygen from the oxidizing stream (air or water) to the fuel. The utilization of a suitable oxygen carrier is of great importance in chemical looping systems for hydrogen production. Thus, numerous studies in the literature are aimed at optimizing the metal performance mainly implemented by varying the chemical composition or the particle morphology.

The key properties of OCs for industrial application should be: high oxygen exchange capacity, favourable thermodynamics properties, fast reaction kinetic, good fluidization properties and resistance to attrition (for fluidized bed configuration), excellent resistance to agglomeration/sintering and to carbon deposition, environmental friendly nature and low cost.

Generally, the main OCs studied are Fe, Ni, Zn, Mn, and Cu [50] but the more recent work almost exclusively investigated iron based oxygen carrier. However, Fe as pure metals do not completely satisfy the listed requirements and additives such as ZrO_2, TiO_2, SiO_2 and Al_2O_3 are needed to improve its mechanical and chemical properties.

Oxygen exchange Capacity (Ro)

The Oxygen exchange capacity, generally reported as Ro, gives an indication about the lattice oxygen which can be exchanged by the OCs in a loop cycle (equation 1). This parameter significantly affects the size of the reactor and the global efficiency of the process.

$$Ro = \frac{m_{ox} - m_{red}}{m_{red}} \quad (1)$$

Where m_{ox} and m_{red} are the weight of the OCs in the fully oxidation and fully reduction state, respectively.

The Ro value of different OCs redox couples are reported in Table 2.0. For each redox couple, the ΔH value is reported for 3 different reductants (H_2, CO and CH_4).

***Table 2-1** : Oxygen Transport Capacity (Ro) and ΔH_{900} (kJ/mol) of different redox couples*[51].

OCs	***Ro***	$\Delta H_{900°C}$ ***(kJ/mol)***		
		H_2	CO	CH_4
Iron				
Fe_2O_3/Fe_3O_4	0.03	-7.915	-41.047	160.903
Fe_2O_3/FeO	0.10	28.105	-5.027	304.982
Fe_2O_3/Fe	0.43	20.597	-12.535	274.729
Fe_3O_4/Fe	0.38	14.231	-20.781	121.0
Fe_2O_3*$2Al_2O_3$ / $FeAl_2O_4$	0.04	-92.544	-125.676	-147.364
Copper				
CuO/Cu_2O	0.10	-117.718	-150.841	-278.278
CuO/Cu	0.20	-100.008	-133.140	-207.470
Nickel				
NiO/Ni	0.21	-14.007	-47.200	136.200
Cobalt				
Co_3O_4/Co	0.27	-24.516	-57.648	94.501
CoO/Co	0.21	-15.791	-48.924	129.393
Manganese				
Mn_3O_4/MnO	0.07	-22.316	-55.446	103.298
Calcium				
$CaSO_4/CaS$	0.47	-12.419	-45.551	142.334

The Ro of the couple Fe/Fe_xO_y increases with the reduction degree of Fe_2O_3. When it is reduced to Fe_3O_4, the Ro is only 0.03, the lowest one in the list. However, a deeper iron oxides reduction at least to FeO phase is needed in the case of hydrogen production by chemical looping technology. For the redox couple Fe_2O_3/FeO the Ro increase until 0.1 and when the Fe_2O_3 is fully reduced to Fe, the Ro is 0.43, second only to $CaSO_4$/CaS (0.47).

Several studies have been performed with different categories of OCs synthetized by various preparation methods and having different compositions of active metals and inert supports [52][53]. The following chapters report the main recent results on OCs performance in the loop cycles aimed at the H_2 production.

Nickel based oxygen carriers

Nickel based OCs are usually used in CLR system because of its strong catalytic activity of hydrocarbon conversion into syngas in reforming processes. Given the high performance of Ni based OCs into many chemical reactions, they have numerous disadvantages for use in commercial scale processes such as high price, safety and health risk. Furthermore, Ni is very sensitive to S poison, which if presents in high concentration in the fuel, leads to a totally catalyst deactivation. In both small laboratory units and pilot plants, Ni-containing OC particles prepared using wet impregnation, sol-gel and co-precipitation methods showed good H_2 yield but carbon deposition on the OC surface is regarded as a concern. The results demonstrated that the carbon formation can be monitored by decreasing the nickel content or by promoters addition [54].Table 2-2 shows a list of Ni OCs used for chemical looping cycles aimed at hydrogen production and the main results obtained.

Effects of Ce and La doping in NiO/Al_2O_3 on H_2 generation by chemical looping steam reforming of ethanol was analysed by Isarapakdeetham et al. [55]. The results demonstrated that the addition of Ce^{4+} and La^{3+} in Ni based OC decreased Ni crystallite size and enhanced the Ni dispersion, resulting in larger active surface area of the OC. Furthermore, the addition of rare earth oxides on NiO/Al_2O_3 helped decrease both carbon deposition and duration of the OC regeneration in the air combustion step. This was likely due to an increased oxygen storage capacity by a redox property of Ce^{3+}/Ce^{4+} and an increased oxygen mobility in the formed La_2O_3–CeO_2 solid solution by a lattice distortion of La^{3+} introduced into fluorite structure of CeO_2. The formation of this modified structure facilitated oxygen lattice diffusion through the OC bulk favouring the conversion of carbon into CO and CO_2 in the fuel reactor. However, the synthetized OC demonstrated to be low thermal stability when tested in loop for 5 consecutive cycles. Stable H_2 yields with Ce modified NiO as redox material are obtained by Jiang et al.[56] that evaluate the activity of 0.5 CeNi-PSNT (phyllosilicate nanotube) in CLR of glycerol. the results confirm the positive effect of Ce on Ni dispersion and reducibility at the reaction temperature of 650°C while the PSNT structure had a strong confinement effect. The hydrogen yield, calculated as the ratio of mass of H_2 produced on mass of fuel consumed, is equal to 12.5%, stable for 10 consecutive cycles. Zhifeng et al.[52] studied the separated production of H_2 and syngas streams by chemical looping steam methane reforming starting form natural ores as redox materials (calcite, maifanite, hematite, dolomite and volcanics). The work is based on Ni/Fe modification of natural ores in order to prevent sintering and to improve their reactivity and selectivity. The results indicated that the modified calcite enhance the calcite performance and inhibits particles agglomeration. Moreover, high ratio of Fe/Ni favour sintering and decline the OC performance. In addition, the influence of different steam /OC and CH_4/OC ratios are studied in terms of H_2 concentration, H_2 yields and CH_4 conversion; the highest value is obtained with steam/OC equal to 0.05 and CH_4/OC of 0.04 when the redox temperature is 800°C. At these operative conditions the lowest carbon deposition on OC surface of 3.23% (based on

the OC mass), is registered. However, the carbon deposition increased with the increase of CH_4 flow rate. After a long-time chemical looping process (6 cycles), the Ni/Fe modified calcite showed a consistently stable performance with average H_2 concentration of 93%.

Li et al.[57] tested the performance of Ni/CeO_2 nanorods OC in a fixed bed configuration of CLR system using ethanol as fuel at constant reaction temperature of 650°C. H_2 selectivity of 80% was achieved by Ni/CeO_2-NR in 10-cycle stability test. The small particle size and abundant oxygen vacancies contributed to the water gas shift reaction, improving the catalytic activity. The covered interfacial Ni atoms closely anchored on the underlying surface oxygen vacancies on the (111) facets of CeO_2-NR, enhancing the anti-sintering capability. Moreover, the strong oxygen mobility of CeO_2-NR also effectively eliminated surface coke on the Ni particle surface.

The redox mechanism of the OC $NiFe_2O_4$ in decomposing steam to produce H_2 in CLSR process was investigated by Huang et al.[58]. The findings revealed that the $NiFe_2O_4$ is more suitable for the CLSR than pure Fe_2O_3 because it has the strongest oxidation performance, facilitating deep reduction of OC in a relatively short reaction time. However, the use of a support is fundamental to give stable activity to the active material. The reactivity of $NiFe_2O_4$ in fact decreases as the Fe/Ni spinel structure weakens and the OC particles sinter. After cycle 1, H_2 production is around 330 ml/g of OC, but in the 20th cycle, it is only 60 ml/g. the addition of the inert Al_2O_3 inhibit collapse of the particle's structure. In this case the H_2 yield measured as mL H_2/g_{OC} was constant at 400 for 10 consecutive cycles.

***Table 2-2**: Recent results of Ni OCs for CL technologies*[59].

Ni OCs	**Promoter**	**Synthesis**	**Process**	**Fuel**	**Reactor**	**T(°C)**	**N. cycles**	**H_2 Yield***	**REF**
NiO	CeO_2 La_2O_3	Wet impregnation	CLR	ethanol	FBR	500°C	-	-	[55]
NiO	ZrO_2	Homogeneous precipitation	CLR	Glycerol	FBR	650°C-850°C	-	-	[60]
$NiFe_2O_4$			CLR	CO		850	20	6.75	[58]
$NiFe_2O4$		Sol-gel	CLH	CO H_2 CO_2	FBR	850	20	24.81	[60]
NiO	Al_2O_3	Wet impregnation	CLR	CH_4	FBR	650(Red) 800 (Ox)	20	38.62	[61]
NiO	CeO_2		CLR	ethanol	FBR	650°C	-	-	[57]

*measured as: mmol/gOC

Iron Based Oxygen Carriers

The high Ro value of the Fe-based oxygen vectors (Table 2-1) makes it one of the most promising materials for CLH technology. However, when iron oxides are used in looping reaction ,without the addition of a support, its reactivity degrades quickly after a few redox cycles, due to the low thermal resistance of the reduced iron oxides form (FeO and Fe), making it unsuitable for long-term cyclic action. Cho et al. [62] studied the mechanism of Fe-based particles agglomeration in a laboratory scale fluidized bed, under cyclic oxidation and reduction. The defluidization of the bed is investigated as a function of the length of the reduction step. Based on the results, agglomeration of Fe-OC particles occurs due the formation of a significant amount of FeO during reduction, which exhibits low thermal resistance.

The lower availability of the lattice oxygen and the low thermal stability of the reduced iron form are the 2 main factors that also affect the hydrogen purity in CLH technologies. The thermal resistance and carbon resistance property varies significantly with different support materials due to the difference on oxygen transfer capacity[63]. Zhu et al.[63] investigated the carbon formation behaviour of iron oxide with $MgAl_2O_4$, CeO2, ZrO_2, and $CeZrO_4$ through methane decomposition reaction. It was found that the incorporation of $MgAl_2O_4$ performed the best carbon resistance at the initial redox cycles. While after 10 redox cycles, the Fe_2O_3/$CeZrO_4$ oxygen carrier still showed a better performance than other supports. When SiO_2 is used as support material, the reactivity Fe_2O_3 decreased significantly as a function of the number of redox cycles because of the formation of unreactive iron silica. Iron-based OCs with Al_2O_3 and $MgAl_2O_4$ support were studied by De vos et al.[64]. The Al_2O_3-supported OC deactivated after 9 cycles of steam regeneration due to the accumulation of an in-situ $FeAl_2O_4$-phase produced by an irreversible reaction between the support and the active phase. By replacing the Al_2O_3 support with $MgAl_2O_4$ the OC deactivation was successfully prevented. The use of MgAl2O_4 make the support inert in the Fe redox path making the OC regenerable by steam and therefore active in H_2 production.

The activity of binary ferrites in CLR and CLH is widely studied in literature[65] [66]. The effect of different dopant elements (Co, Cu and Ni) on the ferrite reducibility is deeply studied by Qiu et al. [66]. The reducibility of each OCs is evalueted by Temperature Programmed Reduction (TPR) performing the OCs reduction with a strem of 5%vol of CO in N_2 in the tempearture range of 100°C to 900°C (Figure 2.5). For all the OCs, 2 stage of reduction are detected: first the reduction of the iron oxides to Fe and then the reduction of the dopant (Co, Cu and Ni) from the oxide to the metallic form. The dopant significantly affects the iron oxide reduction stage: the complete iron oxides reduction is reached only when Ni or Co are added to iron oxides at temperatature of 900°C. in the case of Cu addition the Fe_3O_4 was not fully reduced to FeO at 900°C, demostrating its negative effect on the iron oxides reduction rate, always increase by Cobalt and Nickel dopants.

The activity of binary ferrite spinel with chemical composition of $A_{0.25}Fe_{2.75}O_4$ (where A = Co, Zn, Ni, Cu, Mn) were investigated by Li et al. [65]. At 550°C the modified Co ferrite had the maximum H_2 stored capacity of 62.47 $g*L^{-1}$ with an H_2 flow rate of 132 $molg^{-1}min^{-1}$. The better performance of the materials in chemical looping redox cycles was explained by their combination of high reduction degree and reversible phase changes.

The effect of Co addition into ferrite structure is also evaluated by Li et al.[65]. The synergistic effects of Co and Fe enhance the reactivity of the ferrite structure, principally decreasing the activation energy of reduction reactions. The main function of impurities is to reduce both the oxygen vacancy formation and oxygen diffusion energy barriers, increasing the reducibility of materials, according to density functional theory (DFT) calculations. The Co dopant OC produces the maximum H_2 yield (11.9 mmol g^{-1}) and the fastest H_2 output rate (0.051 mmol $g^{-1}s^{-1}$) of the study at constant redox temperature of 650°C.

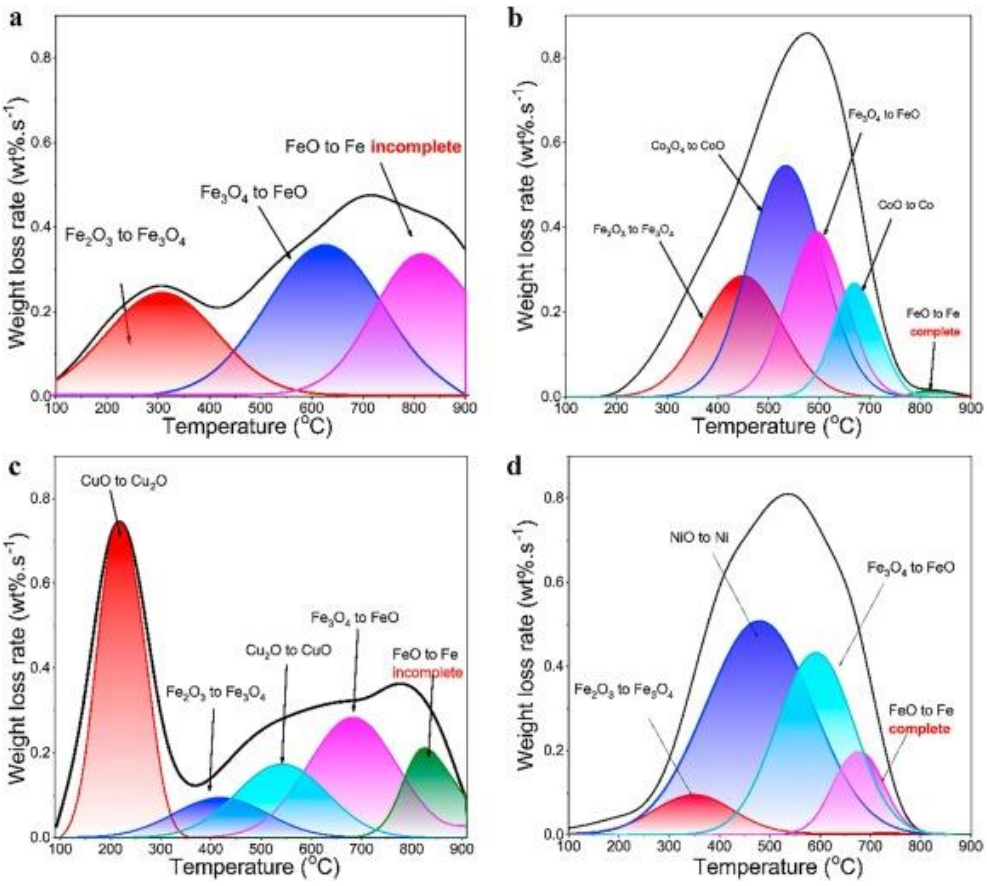

Figure 2.5*: TPR profile of different dopant ferrites: reduction with 5vol% of CO in N_2 stream; (a) Fe_2O3 pure; (b) Co modified, (c) Cu modified; (d) Ni modified* [66].

The use of Mg dopant in Fe-Al based OC materials for CLR of methane aimed at syngas production is studied by Hafizi et al.[67]. The operating conditions of a chemical looping steam methane reforming process were investigated using the response surface method (RSM) based on Box-Behnken design. For investigation and optimization of methane conversion, H_2 yield, and CO/CO_2 molar ratio using RSM, independent variables such as reaction temperature (550°C - 750 °C), Mg loading (0-10%), and OC preparation process (co-impregnation and sequential impregnation) were chosen. The best optimized condition was obtained by using a reaction temperature of 650°C and 5% Mg in an OC prepared using a sequential impregnation method ($15Fe/5Mg/Al_2O_3$) to achieve 98% methane conversion, 83.7% H_2 yield, and a CO/CO_2 molar ratio of 16.5. The addition of Mg to the OC prevented the development of $FeAl_2O_4$ by creating the more stable $MgAl_2O_4$ spinel. This stable spinel also serves as a support for the active Fe_2O_3. Furthermore, the findings show that adding Mg promoter to the OC improves the OCs operation and long-term stability.

The use of CaO modified Fe_2O_3 OCs synthesized by mechanical mixing for CLC and CLH processes was investigated by Ismail et al. [68]. A Thermogravimetric analyzer and a fluidized bed were used to test the mechanically mixed OCs. The material with 57.3 mol% CaO performed the best among the synthesized OCs, according to the results. The enhanced performances are related to the formation of calcium ferrites such as $Ca_2Fe_2O_5$.

The performance of K-modified iron oxide as OC in a fluidized bed reactor was explored by Lui et al. [65]. The addition of KNO3 increased the rate of reduction and hydrogen production, according to the results. The carbon conversion and H_2 production in the reduction process accelerated as the KNO_3 loading in iron ore increased from 0% to 10%. Carbon deposition may be reduced by using 10% K-modified iron ore.

Table 2.3 illustrates a list of the Fe-based OCs for H_2 generation using chemical looping method.

***Table 2-3**: Fe-based Ocs for H_2 production by CL technologies.*

Fe OCs	**Promoter**	**Synthesis**	**Process**	**Fuel**	**Reactor**	**T(°C)**	**N. cycles**	**H_2 Yield***	**REF**
Fe_2O_3	-	Sol-gel	CLH	CO	FBR	650	10	5.9	[66]
Fe_2O_3	Al_2O_3		CLH	CH_4	MBR	850	-	-	[69]
Fe_2O_3	Al_2O_3	Spray drying	CLR	CH_4	FBR	900	-	-	[64]
15%Fe-5%Mg/Al_2O_3		Co-precipitation	CLR	CH_4	FBR	550-750	-	-	[67]
Fe_2O_3	Al_2O_3	Mechanical mixing	CLH	CO	FBR	900	10	5.39	[70]
90%Fe_2O_3-5%Al_2O_3-5%CeO_2		Co-precipitation	CLH	H_2 CO CO_2	FBR	750	11	5.92	[71]

*measured as: mmol/gOC

Fe-based Waste and natural iron ores as OCs

Numerous alternatives low-cost metal oxide oxygen carriers (OCs) have been proposed by various researchers for hydrogen production via chemical looping method. Besides using pure transition metal oxides for the chemical looping technologies, other low value materials such as steel converter slag, low grade ores, and mining wastes can also be considered as potential OCs candidates, enhancing the sustainability of the looping system. These works proved that industrial waste could be a cost-effective OC for the chemical looping processes [72–74]. Xu et al. [72] tested the reactivity of waste products or side stream from the steel production, demonstrating their higher reactivity with respect to the natural ilmenite, tested as reference material. The performance of Incineration Bottom Ashes (IBA) as an oxygen carrier is evaluated by Yin et al. [75] with the aim to realize the syngas combustion by CLC cycle. The promising results confer a high potential to the CLC process, suitable for the use of cost-effective OCs by providing a sustainable application of IBA.

The use of industrial off-gas with high concentration of syngas as reducing agent in CLH process and of Fe_xO_y powder obtained after acid pickling treatment of steel making slag is studied by Cho et al. [76]. The results showed that industrial off-gases can reduce iron oxides to wustite, despite the presence of CO_2 in the off-gases.

An ASPEN Plus simulation study based on the production of syngas and metal oxides from electronic waste (PCB) by CLR and gasification methods was reported by Rai et al.[77]. They demonstrated that gasification and CLR method with CO_2 capture and storage can efficiently produce value added goods from e-waste. The results showed that 47.3% active metal oxides are found in the oxidized metals produced from Air reactor (Fe_2O_3, CuO, and NiO). The remaining metal oxides, such as SiO_2, Al_2O_3, and TiO_2, are inert and can help maintain the reactive OCs thermal stability. The levelized costs of producing energy, hydrogen, syngas, and metal from e-waste were estimated to be 92.28 $/MWh, 3.67 $/kg, 0.0034 $/kWh, and 24.32 $/ton, respectively. Under the co-feed conditions of PCB syngas-PP, the cost of producing H_2 is found to be the lowest at 2.90 $/kg.

The use of natural iron oxide as OCs in CLH is also widely investigated. The reactivity of modified iron ore with biomass ash as OCs in CLH process is studied by Gu et al. [129]. The effect of amount of ashes added, variation of temperature and type of ash used is investigated. Based on the results the OCs activity is very influenced by the type of ash added to iron. In the case of ash with high concentration of Silicon (rice stalk ash) a rapid decline of OCs activity is registered due the low thermal stability of the redox material, suggesting that the presence of Si promotes iron particles sintering. On the contrary a positive effect on iron activity is conferred by the presence of Potassium in the ash, which led to a deeper iron oxides reduction enhancing the H_2 yields. However, an increase in the amount of ash content in the OC (more than 10 wt % in the case of rape stalk ash and wheat stalk ash) resulted in adverse

effects on OC reduction and H_2 generation. The sample with the addition of 15 wt% of sunflower ash shown the best performances, producing H_2 with a purity of 99.57% at 900 C, with an H_2 yields higher than the unmodified iron ores (Average H_2 yield of 0.24 mol and 0.08 mol, respectively).

Ma et al. [78] investigated the performance of natural hematite modified with different amounts of CeO_2. It was reported that CeO_2-modified hematite showed significantly higher H_2 yield and purity than unmodified hematite. The highest reactivity and carbon deposition resistance are registered with the 20 wt% of CeO_2 reached thanks to the higher oxygen lattice mobility of the material. The cubic fluorite CeO_2 and the resulting $CeFeO_3$ perovskite increase the redox performances offering a different oxygen mobility and preventing the Fe migration outward to the particles surface, enhancing the resistance to sintering. With 20 wt% of CeO_2 added, the H_2 yields are 110% higher than the value obtained without CeO_2. Differences are also relieved in term of H_2 purity; in the presence of CeO_2 a 99.71% pure hydrogen is produced while only a purity of 98.78% was obtained with pure hematite.

The effect of rare earth (Ce-doped and La doped) on iron ores activity is investigated by Gu et al.[79]. According to the results, both Ce- doped and La-doped iron ore as OC showed a better reduction reactivity than the undoped iron ore and a comparatively steady redox performance at 900 C after the primary activation process, improving hydrogen generation. Furthermore, the La-doped iron ores shown higher performances because of the chemical interaction between Fe and La forming $LaFeO_3$, very active in a water-splitting reaction; the La-doped sample produces 2.56 L of H_2 compared to the 2.28 L obtained with Ce-doped iron ores.

Wang et al. [80] investigated the influence of K and Cu addition to iron ore on carbon deposition in H_2 production using the chemical looping method. The outcomes showed that the OC loaded with K and Cu have an exceptional endurance to carbon depositions. The results concluded that the decrease in carbon deposition was reached thanks to the lower concentration of the active Boudouard reaction sites and due to the physical and chemical changes introduced by Cu and K addition.

Various other ores and industrial residues are also utilized as OCs in chemical looping processes such as copper ore[81], ilmenite[82], iron ore [83] and bauxite residue (Red Mud) [84].

The above-mentioned ores and industrial residues have shown excellent stability and reactivity in different chemical looping techniques but, among these low-cost OCs very few have been found to be active in the water-splitting reactions for hydrogen production.

The production of hydrogen using natural ores and industrial wastes with high Fe concentration as oxygen vectors can be a scope for future studies.

2.3 Reactor design

Two main reactor types are successfully operated in CL technologies both in laboratory and in pilot plant scale: fixed bed and fluidized bed reactors.

The fixed bed reactor configuration (FBR) works by feeding alternatively the fuel in reduction and the steam in oxidation, while the OCs is placed inside the tubular reactor. The redox cycles are performed consecutively in a batch mode, enabling a system design with a low degree of complexity due to the absence of moving parts.

In the fluidized or moving bed reactor the oxygen carrier circulates between separated reactors or reactor sections. The moving solid material increases the system complexity and the mechanical strain of the OCs needed while the gas slip between the 2 reactors caused a low degree of purity of the products streams (reduction and oxidation). However, the higher technological complexity enables several beneficial properties.

- The production of a continuous separated streams of reduction and oxidation products.
- An optimized reactor layout (materials, design, operative conditions) for reduction and oxidation reactors.
- The OCs can be replaced in normal operation mode without interrupt the feeds.
- The OC actively participates to the heat integration management system as they deliver the heat from the exothermic reactions to endothermic ones, reducing the external heat demand.

A 25 kWth sub-pilot syngas for syngas chemical looping (SCL) composed by a system of three fluidized bed reactors was introduced by Sridhar et al. [85] (Figure 2.6). The continuous pilot plant is one of the first demonstration unit for H_2 production by capturing the 100% of CO_2 emissions. The experiments are conducted using syngas produced by coal gasification as fuel and Fe-based OC as reactive fluidized bed. The fuel reactor and the steam reactor were operated in a co-current moving bed system and a fluidized bed air reactor, which acted as a riser. The reactors were separated by a system of two ball valves. The solid flow rate was controlled with a rotary disc feeder. Experiments were performed with syngas (CO/H_2 = 2/1, flow rate 15 $L \cdot min^{-1}$) at 900 °C and a solid flow of 150 $g \cdot min^{-1}$.

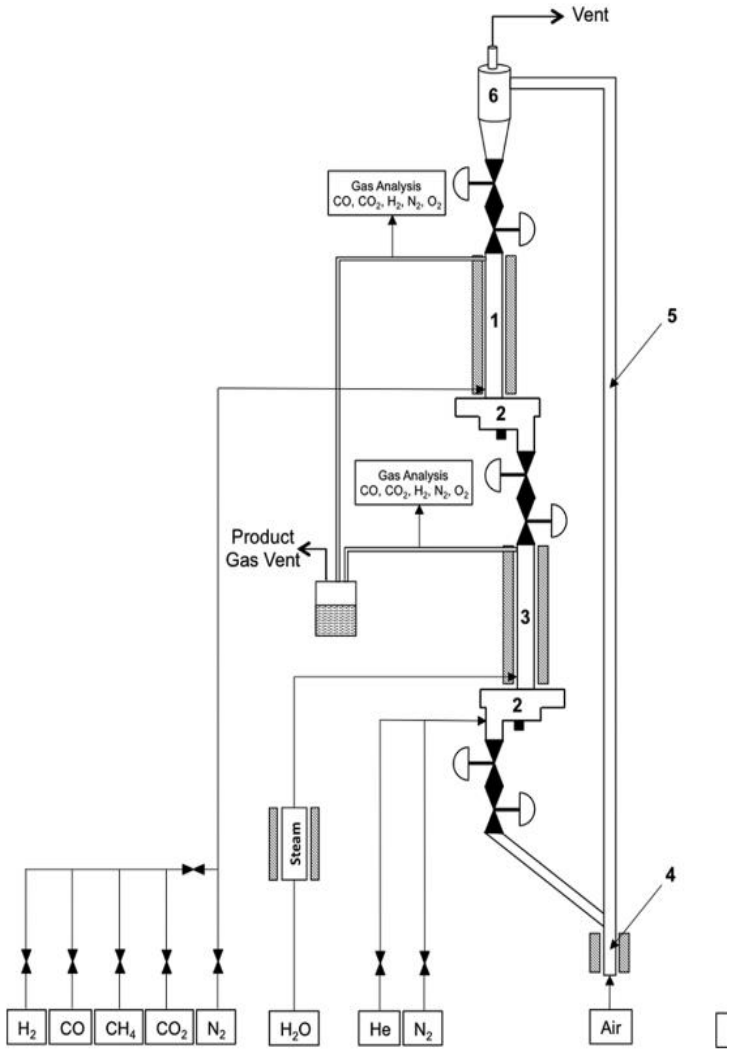

Figure 2.6*: Schematic diagram of 25 kWth subpilot plant for hydrogen production by SCL. Ohio State University. Sections 1, 3, and 4 represent the moving-bed reducer, moving-bed oxidizer, and the fluidized-bed combustor, respectively. Section 2 is the rotary solids feeder. Section 5 is an entrained bed riser, and section 6 is as cyclone-solid−gas separation device*[85].

The production of an H_2 stream with purity in the range 94.4% to 98.4% when the conversion of the OC at the reducer exiting is 35.54%.

Tong et al [86] optimized operation parameters and investigated the redox performance of two iron-based OCs having different particles sizes (2 mm and 4.5 mm of diameter) during a total operation of 300 hours. Experiments were conducted in the same 25 kWth sub-pilot plant. Both samples provided sufficient high cycle stability, whereas the smaller particles possessed a faster reaction rate, probably due to the higher surface area. Both samples performed similarly well regarding syngas conversion and hydrogen purity. The smaller particles had a lower fluidizing velocity and required less air in the rise to be transported. Hence, smaller oxygen carriers are expected to show better flow properties and a higher

resistance to attrition. System improvements by reducing gas leakage between the reactors were achieved by replacing mechanical seals with a non-mechanical valve consisting of a standpipe with injected nitrogen. Furthermore, a gas preheater for the synthesis gas feed was installed to prevent carbon deposition at lower temperatures and a dual syngas injection was added to optimize the axial gas concentration profile and increase the syngas conversion from 78.34% to 92.23%. A final hydrogen purity > 99% at steady conditions was obtained. The system was also operated using methane with a feed conversion of 99.99% while maintaining a high oxygen carrier conversion of 32.50%. A reduced solid flow rate increased the reduction degree to 48.82%, however the CH_4 conversion dropped to 80.35%. The results suggested that a complete fuel conversion is predefined by a critical solid/gas flow ratio. Flow ratios that exceed this ratio result in a non-reacting zone in the top of the moving bed. The counter-current moving bed used in this system is expected to increase the oxygen carrier conversion by up 5 times compared to a co-current fluidized bed system with 11%. In an experimental investigation lasting 2 hours, an oxygen carrier conversion in the reducer reactor of 35.54%, related to the theoretical value of 39.6%, was achieved, while maintaining a syngas conversion of > 99%.

Based on previous results with a syngas feed, the 25 kWth sub-pilot unit was utilized for the coal direct chemical looping process (CDCL) in continuous operation lasting 200 hours. A coal conversion ranging from 90 – 99% with an average conversion of 99.7% was obtained. These experiments were not combined with the steam oxidizer; hence no conclusion can be drawn on the possible hydrogen purity, however, combustor gas analysis for carbon sequestration indicated a CO_2 purity of 99.7% with CO 0.2% and CH_4 0.1% as the main impurities.

A 30-kWth moving-bed chemical looping system for hydrogen production was development at the Industrial Technology Research Institute (ITRI) of Taiwan (Figure 2.7). The experimental results published by Chen et al.[87] is on the H_2 production by using methane as reducer of iron oxides, which are pneumatically transported in the system. The steam oxidized iron oxides are then fully oxidized in an air combustion step which repristinate Fe_2O_3 phase, leading to a temperature increases of 120°C. An iron-based oxygen carrier containing 40 wt% Fe_2O_3 on Al_2O_3 (particle diameter of 2.5 mm) was pneumatically transported in the closed circulation loop with a circulation rate of 2100 g/min. The oxygen carrier was delivered forward through a venturi flow control valve, which was purged by nitrogen (250 L/min) to control the circulation rate of the oxygen carrier. The oxygen carrier was directly sent upward through a riser with the outlet diameter of 0.05 m, using an airflow produced by a fan. In order to transport oxygen carrier in the riser, the carrying gas velocity in the riser should be larger than terminate velocity of oxygen carrier particle. The air flow rate was controlled at 1000 L/min at the bottom of the riser. Combined with the nitrogen flow rate from the venturi valve, the gas velocity to transport oxygen carriers at the bottom of the riser was calculated to be 10.3 m/s. The carrier subsequently entered the cyclone at the top of the system, which separated the fine particles and dusts from normal oxygen carriers. The fine particles and dusts were collected in the dust collector, and the

normal oxygen carriers were then dropped into the combustor. For the 10 m high riser, the residence time of oxygen carriers in the riser was approximately 0.78 s. This time is insufficient for the fully magnetite oxidation to hematite and therefore an additional combustor was placed between the cyclone and reducer in the 30 kWth system. The moving-bed combustor ensured that the oxygen carriers had an adequate residence time for their complete oxidation to hematite. This oxidation resulted in the release of heat which led to an increase of the OC temperature. After that, the fully oxidized oxygen carriers moved downward to the reducer by gravity for the next circulation.

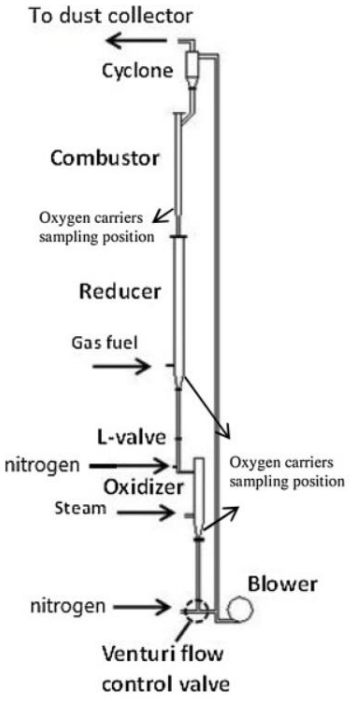

Figure 2.7*:Scheme of 30 kWth of CLH system*[87].

For a steady state operation, the concentration of carbon dioxide produced in the reducer was 95 %, and the concentration of hydrogen produced in the oxidizer reached 90 %.

An integrated test unit of 0.3 kWth was constructed by the Chen et al. [88] aimed at generate a separated high-purity H_2 and CO_2 streams using ZrO_2 supported Fe_2O_3 as OC and methane as a feedstock (Figure 2.8). All together the unit was operated for 27 h includes start-up (6.6 h) period, steady state (13 h) operation and carbon formation (8.0 h) operation.

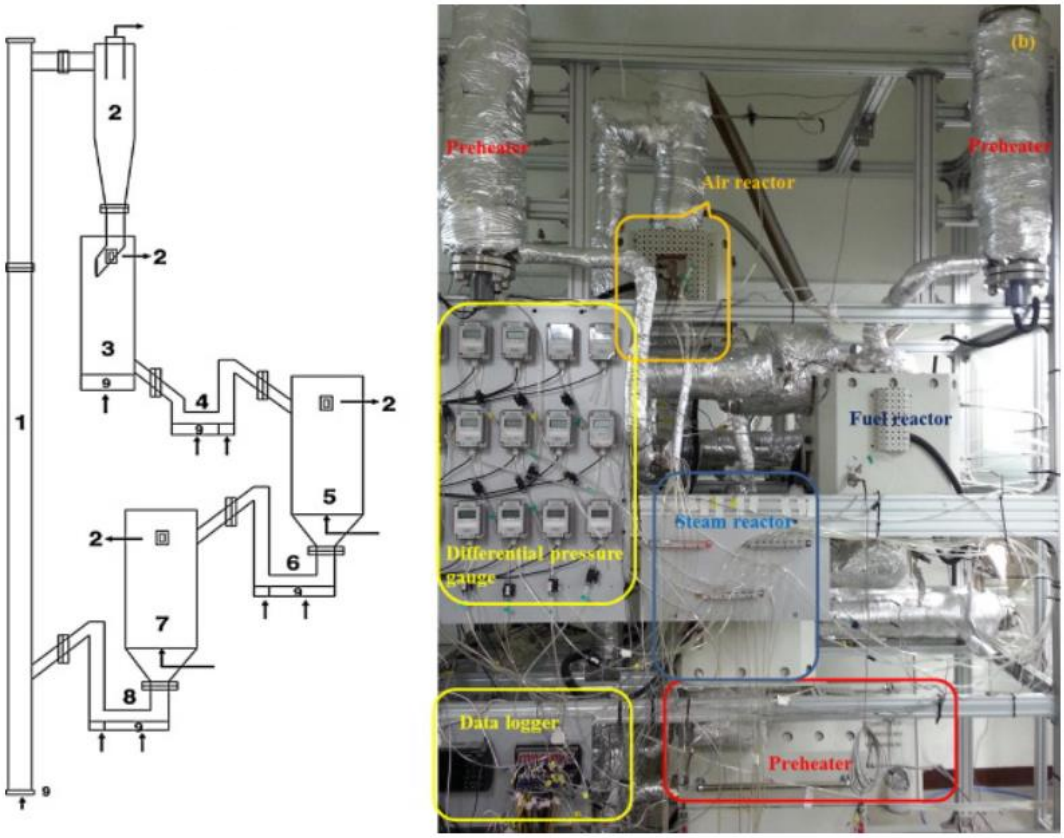

***Figure 2.8**:Scheme (left) and picture (right) of the CL system*[88]. *1) Riser, (2) cyclone, (3) air reactor (AR), (4) AR loop-seal, (5) fuel reactor (FR), (6) FR loop-seal, (7) steam reactor (SR), (8) SR loop-seal, and (9) distributor*

The OCs showed no agglomeration and only small signs of thermal sintering, which suggested a high durability. An average methane conversion of 94.15% at 900 °C was achieved. Fuel flow analysis indicated that a high methane conversion is possible as long as a moving bed regime is maintained.

A transition to a fluidized bed reduced the methane conversion to below 90%. When the reduction of the OCs is limited until the FeO phase, the purity of the produce H_2 stream is of 99.15% at the redox temperature is 800 °C with minor CO contaminations. CH_4 was not detected, which suggested that gas leakage into the steam reactor was negligible. The main responsible of H_2 contamination is the carbon deposition during reduction step, catalysed by the iron formation.

Xue et al.[89] developed a three-reactor fluidized-bed system in the range of 50 kW (figure 2.9) . The system was constructed and operated as a cold-flow model, widely used to study the process fundamentals such as: pressure drop, solid fraction and solid circulation rate and to improve the operation and tackle the problem by troubleshooting. The cold flow experiments performed in long-term operation steps were conducted by using air or helium in all the reactor and with glass beads as solid particles at constant pressure. By varying the gas flows and changing the fluidizing conditions,

the solid circulation rate was manipulated. It was found that the solid circulation rate influenced the gas leaks between the reactors, which is of high importance regarding hydrogen purity and CO_2 emissions. The main design values were an operation temperature of 900 °C, methane as fuel, a particle size of 100 – 305 µm, a solid inventory of 5 kg and gas flows between 24 – 31 $Nm^3 \cdot h^{-1}$.

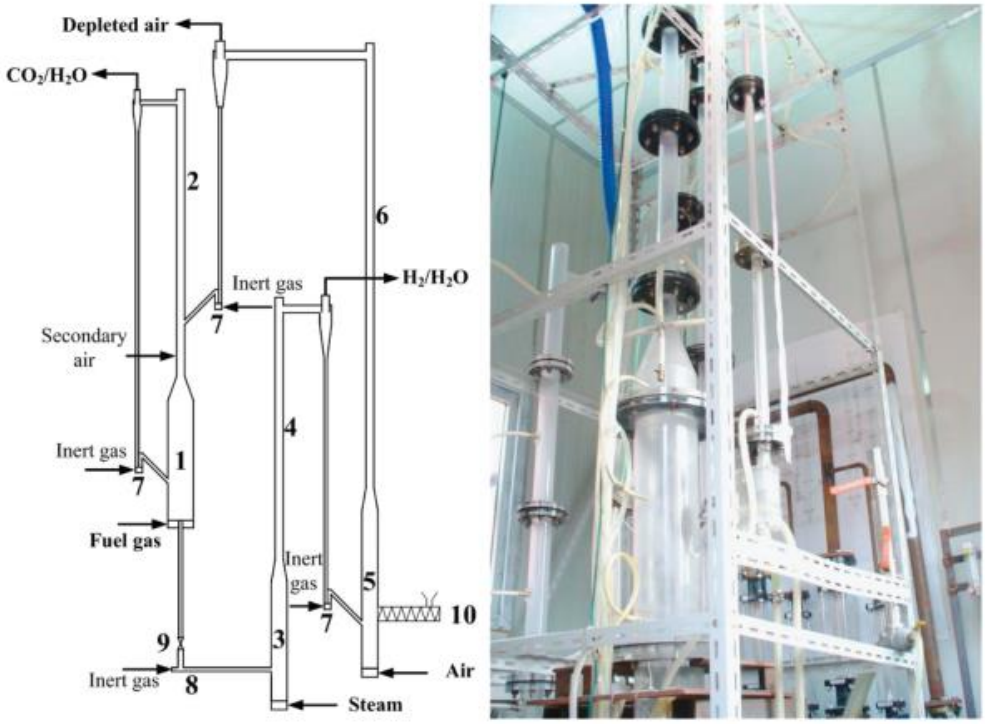

***Figure 2.9**: simplified scheme of the CL system*[89] *(1) lower fuel reactor, (2) upper fuel reactor, (3) low-velocity zone of the steam reactor, (4) riser of the steam reactor, (5) low-velocity zone of the air reactor, (6) riser of the air reactor, (7) loop seal, (8) L-type loop seal, (9) ball valve, (10) screwed feeder.*

***Table 2-4**: Continuous looping hydrogen pilot plant.*

Unit Scale (kW_{th})	**Fuel**	**H_2 purity**	**Location**	**OCs**	**T(°C)**	**Reactor**	**year**	**REF**
25	Syngas	94-98 %	Ohio	Fe	900	MBR	2012	[85]
50	CH_4	-	Nanjing	Fe	900	FBR	2012	[89]
30	CH_4	90 %	Taiwan	Fe	650-950	MBR	2020	[87]
0.30	CH_4	99.15%	Korea	Fe	800	MBR	2014	[88]
25	Syngas	99.99 %	Ohio	Fe		MBR	2014	[86]

2.4 Process Development

Based on the promising results obtained in the numerous studied in literature, the chemical looping system was also exploited to unconventional aims such as for the selective separation of a gaseous species or for the green hydrogen production by renewable unconventional feedstocks. Generally, the use of renewable sources in CL technologies requires first the conversion of the complex renewable source into syngas through different methods (such as partial oxidation, steam reforming etc.), increasing the complexity of the total system.

CLH as gas separation method

The study conducted by Herguido et al. [90] proves that the redox properties of the transition metal oxide can be successfully exploited also to perform the selective separation of H_2 from a gaseous stream that contain it. The work is focused on the separation of pure H_2 from a mixture of CH_4 and H_2 exploiting the higher reducibility power of H_2 with respect methane. A reactor with two interconnected fluidized beds and an iron-based oxygen carrier were used for the fuel processing. Reactions were executed in a temperature range of 500 – 550 °C and with different hydrogen concentration in the mixture (from 35% to 65%). The operation at low temperature is fundamental to avoid CH_4 cracking, which involves solid carbon formation and therefore the H_2 contamination during the oxidation step. The results demonstrated that the operation conditions enabled a reduction of iron oxide with hydrogen, and methane and other impurities appears as inert. However, the complete conversion of hydrogen during reduction is not reached but an average hydrogen conversion of 20% was obtained with little influence of the varied parameters (gas velocity, relative velocity and hydrogen content), which suggested that the separation performance is mainly limited by thermodynamic restrictions. The separations system was tested for 44 h producing pure hydrogen without carbon contaminations. Small amounts of solid carbon were found in the reactor after the operation suggesting that coke remained inert during the experiments at the selected oxidation conditions (500°C).

Biogas as source of reducing agents

The feasibility to produce green H_2 by CLH is recently studied in literature. The production of renewable reducing agent able to efficiently convert the iron oxide into iron and to guarantee the production of a stream of pure H_2 in the oxidation step is the crucial phase.

With the aim to use biogas to produce the reducing agent needed for the process, Plou et al.[91] and Herrer at al.[92]combined the catalytic dry reforming with the CLH by using as redox material a solid mixture of 98 wt%Fe_2O_3-1.75 wt% Al_2O_3- 0.25 CeO_2 and NiO/$NiAl_2O_4$ with an excess of NiO of 10

wt% (with a OCs/Ni-based catalyst of 85/15 wt%). The iron-based material is active in H_2 production while the NiO based one acts as catalyst from the conversion of biogas into syngas, able to reduce iron oxides to iron. Experiments were performed with different biogas compositions (50%vol CH_4 and 65wt% CH_4 in CO_2) in the range of temperatures 600°C – 750 °C. Three stages were visible in the fixed bed reductions, which were analysed in detail. The reaction started with a high methane conversion directly followed by a conversion minimum. This phase was initially dominated by the reduction of Fe_2O_3 to Fe_3O_4 and the full oxidation of the feed to CO_2 and H_2O. After the consumption of the lattice oxygen of Fe_2O_3 the reduction of NiO to Ni occurred, which was indicated by the appearance of H_2 and CO. The NiO reduction to Ni is fundamental to catalyse the dry methane reforming, producing a stable fraction of CO and H_2. At this stage also a complete iron oxides reduction to iron is reached. Once the oxygen carrier was completely reduced, the solely catalytic dry reforming of biogas was observed.

An increasing reaction temperature enhanced the reaction rates and the transition to the stable reforming stage (methane conversion into CO and H_2) whereas an increased CH_4 ratio slightly accelerated the transition between the stages. The comparison of experimental data with theoretical data showed good accordance for the dry reforming but a constant deviation regarding the iron oxide reduction reaction, which suggests diffusion limitations hindering the mass transfer. The formation of coke by CH4 decomposition indicated by a too high amount of measured hydrogen and thus the deactivation of the catalysts by blocking of active catalytic sites was observed. The effect was enhanced with increasing CH4 fractions. Post reaction analysis reported the presence of graphitic carbon and highly amorphous carbon. Coke was only present on the nickel particles, which explained the catalytic degradation. During the purging phases with inert gas a mass loss was observed, which increased with higher temperatures. This suggested a solid-solid decoking reaction between the incompletely reduced oxygen carriers and the solid carbon and explained the absence of coke on the oxygen carrier in the post experimental analysis. The oxidations with steam at 500 °C produced hydrogen with a purity of > 99% with carbon dioxide as impurity but a fraction of carbon remain on the solid particles surfaces and thus accumulates over consecutive cycles without a regeneration step.

A combination of a catalytic methane steam reforming and the chemical looping hydrogen process in one reactor with two adjacent fixed bed was investigated by Nestl et al. [93]. Investigations of methane reforming were executed, varying temperature, pressure and the S/C-ratio, emphasizing a high conversion of CH_4, the avoidance of carbon depositions and a reformate-gases with a sufficient reduction potential. The results suggested that high CH4 conversion of > 99% is possible, however higher system pressures require a significantly greater S/C ratios, and thus yield synthesis gas with increased water content and a lower reduction potential. It was concluded that the reforming in combination with the reduction step of an iron based oxygen carrier should be performed at ambient pressure. The oxidations with steam were executed at elevated pressure up to 8 – 11 bar to produce

hydrogen with a purity > 99%. Small amounts of CO2 were detected, which implied the formation of solid carbon during the reduction, although not predicted by the simulations.

Pyrolysis gas as reducing agent

Xu et al. [94] studied the activity of modified iron ores on chemical looping hydrogen by using a simulated biomass pyrolysis gas (BPG) as reducing agent. The carbon capture efficiency, hydrogen yields and H_2 purity are optimized. BPG composition was 10% H_2 + 10% CO + 5% CH_4 + 75% N_2 balance. The experiments are performed in a three-fluidized bed reactor CLH system consisting into a fuel reactor (reduction) a steam reactor (steam oxidation) and an air reactor (air oxidation). Several modified iron ores were tested as redox material (M_xO_y–iron ore, M = Ni, Cu and Ce) in order to find the optimal one. The active role the metal added is visible in figure 2.10 where is reported a comparison of the hydrogen purity as function of the reduction temperature and the carbon efficiency/H2 yields at consecutive cycles at 900°C

a) b)

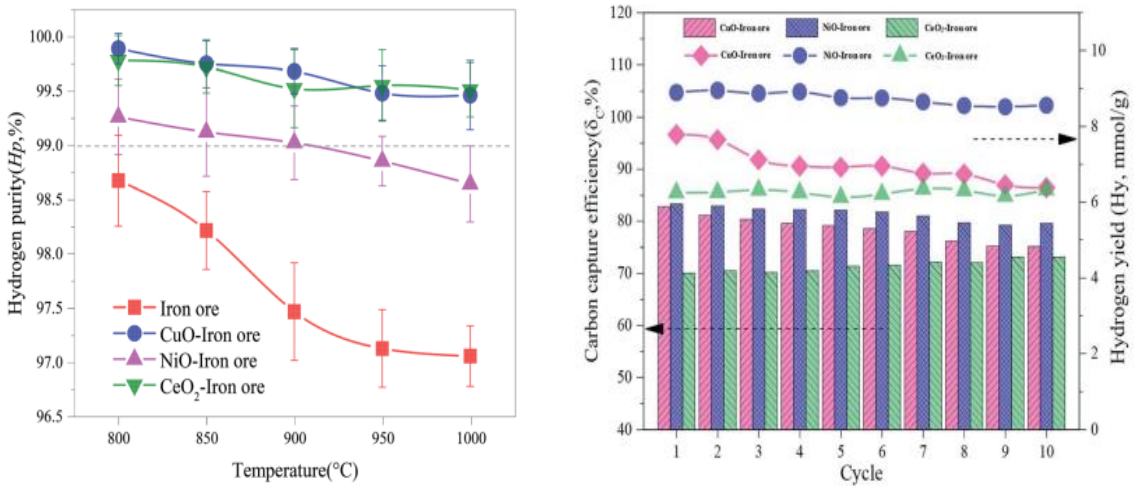

***Figure 2.10**: H_2 purity at different reduction temperatures(a); carbon capture efficiency and H_2 yields at cyclic redox operation at 900°C* [95].

The hydrogen purity changes with the metal addition, with a slower decrease at higher reduction temperatures. The higher resistance to carbon is reached by the NiO and CuO iron ores modification. Among the materials tested, the NiO-iron ores demonstrated to be the more active in terms of hydrogen yields and hydrogen purity, equal to 8.89 mmol*g^{-1} and 99.02%, respectively (figure 2.10). The carbon capture efficiency was equal to 83.29% when the reduction temperature is 900°C and a length of reduction of 40 minutes, operative conditions for which the hydrogen yields are the highest.

Heavy fraction bio-oil as feedstock

Zeng et al.[96][97] investigated the reduction behaviour of a bio-oil heavy fraction from a cotton stalks pyrolysis unit with a water content of 18.54 wt%. Ilmenite was selected as the proper oxygen carrier in a fixed bed redox reaction for its resistance to carbon depositions and reducibility at temperatures > 950 °C. Preliminary experiments yielded a carbon conversion in the range of 57% – 82%, which was enhanced by an increasing temperature with an optimum at 950 °C. In several consecutive cycles, the ilmenite sample achieved a stable hydrogen yield of 93 – 96 $Nm^3 \cdot kg\text{-}1$ within the first 10 cycles. However, after 10 cycles, sever sintering, which led to a lower active surface and average pore diameter, and a drop in released hydrogen was observed. Significant amounts of carbonaceous contaminations were detected with a hydrogen purity below 85%. The gasification of solid carbon with steam was identified as the source of contaminates. The heavy fraction of the used bio-oil contained a high amount of phenolic compounds, thus increasing the tendency towards carbon deposits. In order to improve the hydrogen purity steam was added during the reduction process. A steam/oil ratio of 2.0 improved the carbon conversion of the fuel to > 99% and enhanced the hydrogen purity to > 99%. However higher amounts of steam decreased the oxygen carrier reduction degree, thus lowering the amount of produced hydrogen.

H_2 production by Fe oxidation in hydrothermal conditions

Hydrothermal hydrogen generation by the oxidation of iron enables the operation at very mild temperatures in the range of 100 – 200 °C. This reduces the complexity of the oxidation process significantly compared to conventional chemical looping water splitting, which usually requires temperatures > 600 °C. Feasibly studies were performed by Tsai et al.[98] in an autoclave by measuring the pressure profile and gas phase at different reactor temperatures. Reference tests were performed with solely water as reactor filling. The supplement of iron powder led to a constant pressure increase, which was further raised by the amount of iron, the reactor temperature and smaller particle sizes. After oxidizing the iron powder, the pressure remained at a constant level. The gas phase consisted of pure hydrogen with a low water content of 0.525% at 120 °C. Michiels et al.[99] further enhanced the hydrothermal process by using a 1 molar potassium hydroxide solution. The system was put under CO2 pressure, which dissolved in the aqueous solution and formed potassium carbonate in the presence of potassium hydroxide. The reactor was heated to temperatures up to 200 °C. Iron in the presence of carbonate was oxidized with water to magnetite, H_2 and CO_2 within a reaction time of 16 h. After cooling down, hydrogen was measured in the gas phase with a purity of > 99 mol%. Experiments focusing on the role of compressed CO_2 in the system revealed that the dissolved carbon dioxide was critical for the process by forming carbonate ions to promote the oxidation of iron to hematite. The absence or deficit of CO_2 resulted in a reduced amount of produced hydrogen. An excess of CO_2 caused

the formation of siderite instead of magnetite, thus a lower amount of hydrogen with significant CO_2 contaminations. The presence of potassium hydroxide was vital in the system to promote the solubility of CO_2 and the formation of CO_3^{2--} ions. The absence of potassium carbonate resulted in a lower amount of hydrogen. The system did not suffer from a net-carbonate-ions loss within one complete cycle. Hence, the aqueous solution can be reused in the sequential cycle by adding the amount of consumed water

2.5 Process simulation

The process simulation of the biomass-based reductant in the chemical looping system are required to optimize the configuration in terms of process efficiency. The main chemical looping configuration studied is the three-step system because of its superior total efficiency. This configuration owns several advantages and all of them are connected to the carbon conversion into CO and CO_2 during the reduction or fuel stage. The presence of an air combustion at the end of the redox cycle solves all the issue related to solid carbon accumulation which are responsible of low degree of H_2 purity and low OCs reactivity at repeated cycles. Furthermore, the restore of Fe_2O_3 before the reduction step makes possible to convert the fuel into CO_2 and water, fundamental to allow an easily CO_2 capture.

3 steps CLH system offer the possibility of a high carbon capture rate with low energy penalties, which makes the technology promising for renewable and fossil feedstocks alike. Particularly emphasizing renewable sources, different feedstocks were considered and analyzed, focusing the attention on their hydrogen production capabilities and system efficiencies. The systems were optimized with the defined specifications of :

- High solid conversion
- Low concentrations of H_2 and CO in the fuel reactor outlet,
- No carbon deposition
- Minimized wt% of support material
- Minimized external heat input,
- Low solid flow rates
- Maximized product gas yield

Three-reactor chemical looping systems

Cormos et al.[100] performed a techno-economic evaluation of direct biomass chemical looping conversion for both hydrogen production and power co-generation . The process is studied in a three-reactors chemical looping system (fuel-steam oxidation and air oxidation). Sawdust is chosen as biomass because of its low ash content, necessary to minimise the alkali corrosion problems always presents in the case of direct biomass combustion. Ilmenite is used as low-cost OC.

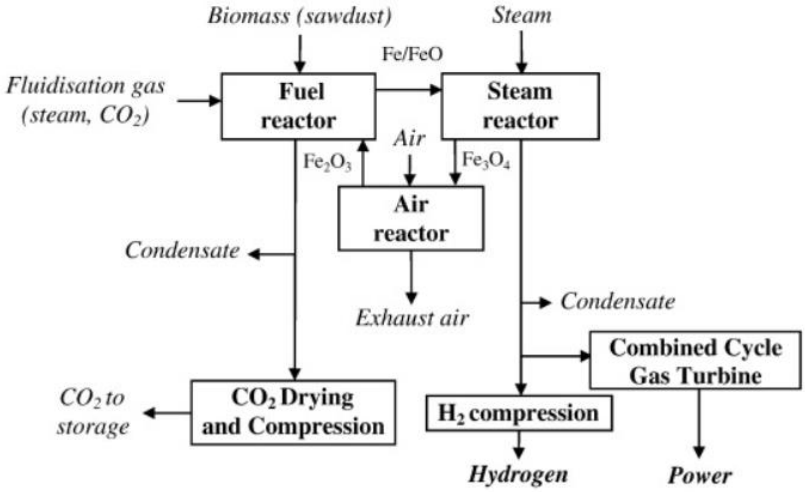

Figure 2.11*: scheme of H_2 and power generation by biomass direct chemical looping*[100]

Four cases were considered, which differences in their heat integration strategy.

Case 1 : Biomass direct chemical looping for hydrogen production and cogeneration of power (BDCL)

Case 2 : IGCC power plant without carbon capture using coal and sawdust as fuel

Case 3 : IGCC power plant with pre-combustion capture based on gas–liquid absorption (Selexol®) using coal and sawdust as fuel

Case 4 : IGCC power plant with pre-combustion capture based on gas–liquid absorption (Selexol®) using coal and sawdust as fuel.

The carbon capture energy penalty for BDCL configuration is 3.5 net electricity percentage points, significantly lower than the results of Selexol®-based gas–liquid absorption configuraton (with 9.2 points) and syngas-based chemical looping (8 points). The overall energy efficiency of BDCL concept is significantly higher compared to the benchmark cases (5.7 net percentage points compared to gas–liquid design and 4.5 points compared to syngas-based chemical looping design). The carbon capture

rate of BDCL concept is almost total (> 99%) in comparison with gas–liquid absorption option (90%). The syngas-based chemical looping design has also an almost total carbon capture rate. Moreover, the economic evaluation shows that the BDCL concept has a reduced carbon capture capital cost penalty than the benchmark carbon capture cases (6.4–7 percentage points lower specific investment cost). O&M costs show an opposite result (8.1 to 13.4 percentage points increase for BDCL concept compared to the benchmark cases) because of the OC make up stream needed for ash removal. The cost of electricity is lower than gas–liquid design (about 3.7%) and higher than syngas-based chemical looping case (5.7%).

The application of bioethanol (12% ethanol and 88% water) from fermentation processes was examined by Cormos [101] to assess its use in the hydrogen production chain at industrial scale (100000 Nm^3/h hydrogen, equivalent to 300 MW thermal) with carbon capture units. High system efficiencies were achieved in two system variations; In the Case 1 ethanol is first reformer to produce syngas, useful in the iron loop while in the Case 2 bioethanol is directly fed in the chemical looping system(Figure 2.12). The total energy efficiencies were 59.78% with an electric power output of 13% and 63.66% with an electric power output of 7%. The carbon capture rate was > 99% in both plant simulations. The conventional reforming system with a gas-liquid absorption as a benchmark yielded efficiencies in the range of 53 – 58%, while enabling a carbon capture efficiency of > 99%.

a)

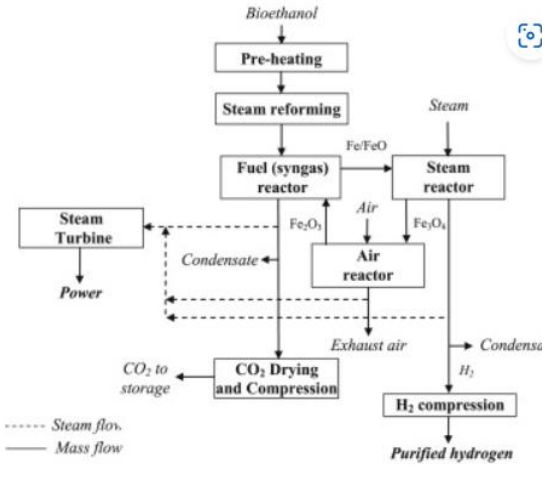

b)

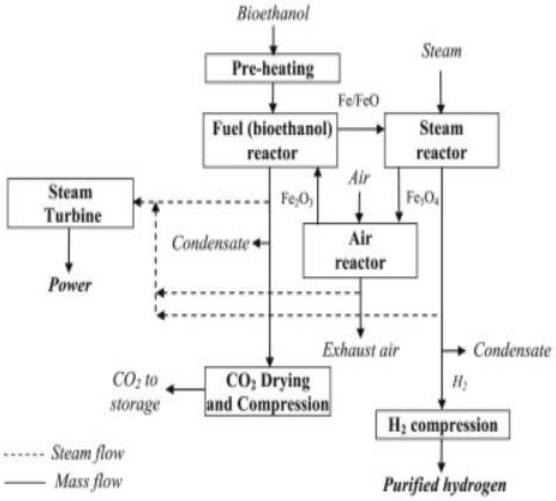

Figure 2.12*:Case 1 (a) and Case 2(b)* [101].

Gopaul et al.[102] investigated the conversion of unconventional biomass. Three types of biomass were evaluated, assuming the absence of sulphur and nitrogen components. Poultry litter was chosen over wood pellets and oak pellets because of the higher hydrogen yield. Tar products formed during the biomass gasification process were not separated but fed into the chemical looping fuel reactor. Reduced iron and remaining tars were separated from the gaseous products and fully oxidized in the steam reactor. Both reactors yielded a hydrogen rich synthesis gas (H_2, CO_2, CO, CH_4, H_2O), which was utilized in a reformer at 500 °C to oxidize the residual methane and maximize the hydrogen output. A hydrogen yield of 1.60 $kmol \cdot kmol_{feed}^{-1}$ diluted with 34% CO_2 and 2.3% H_2O with a final hydrogen purity of 63% was obtained. A reference water-gas-shift system generated 0.97 kmol·kmolfeed-1

Yan et al.[103] added a SOFC unit to the biomass-fed three-reactor chemical looping hydrogen system using coal and wheat straw. Post combustion of the anode off-gas, a steam turbine for power generation and CO2 sequestration were considered. The amount of hydrogen and the total thermal efficiency were raised by increasing the gasification temperature, which improved the carbon conversions efficiency. Upon reaching a complete biomass conversion no further positive temperature effects were visible. The same behavior was found regarding the S/C ratio in the gasification unit. Below the ratio for a complete biomass conversion an increased amount of steam indicated positive effects on the plant performance, while an excess of steam lowered the total efficiency. The increased oxygen carrier circulation rate raised the amount of produced hydrogen per mass biomass. However, upon reaching the point of full oxidation of CO to CO2, only hydrogen was consumed for the reduction reaction in the fuel reactor, which lowered the plant performance. The system evaluation yielded a total energy efficiency of 39.9% and total exergy efficiency of 37.6 % with a carbon capture rate of 96%. The comparison of a three-reactor system and a two-reactor system using the same feed gas conveyed the main difference in the behaviour of the fuel reactor temperature. Higher temperatures in a three-reactor system increased both the total thermal efficiency as well as the amount of hydrogen per mass of feed. The endothermic reduction reaction was thermodynamically promoted at higher temperatures and enabled a greater reduction degree of the oxygen carrier. In the two-reactor system the absence of the air oxidation step needed to supply the necessary heat of the proposed scheme, had to be substituted by the combustion of biomass. Thus, the thermal efficiency and the amount of hydrogen per mass feed decreased. Both systems enabled a carbon capture rate of > 95%. The two-reactor system had a higher cold gas efficiency of 60% compared to 54% and a higher hydrogen production capability of 0.76 $Nm^3 \cdot kg_{biomass}^{-1}$ compared to 0.66 $Nm^3 \cdot kg_{biomass}^{-1}$. A calcium-based sorption enhanced looping system used as reference had a higher cold gas efficiency of 72% with 0.73 Nm³·kg-1 of hydrogen but a lower carbon capture efficiency of 92%.

Edrisi et al.[104] proposed a three-reactor chemical looping technology to produce pure streams of hydrogen and nitrogen as feed for an ammonia production plant and a third stream of pure carbon dioxide for sequestration. In the fuel reactor an iron-based oxygen carrier completely converted CH_4 to

CO_2 at 726 °C. In the steam reactor a pure hydrogen stream was produced by partially oxidizing iron with steam at 723 °C. In the air reactor, a pure nitrogen stream was generated at 880 °C by fully consuming oxygen in the air stream and completely oxidizing the solid material. The fuel and air fed and the oxygen carrier fed were varied to optimize the operation conditions of the product streams. The ratio OC/CH_4 of 4.0 and the ratio air/CH_4 of 3.206 were found to enable the production of pure streams, while maximizing the reduction degree of the solid material. $MgAl_2O_4$ was added as support material with a ratio of $MgAl_2O_4/CH_4$ of 6 to improve the heat integration of the system.181 The simulation yielded a hydrogen production efficiency of 80.2%.

Yang et al.[105] integrated a three-reactor system into a Fushun-type oil shale retorting process (OSR-CLH)). In conventional oil shale plants, a retorting gas with a low heating value is produced and converted to electricity via an internal combustion engine. The chemical looping process instead utilizes this retorting gas for hydrogen production. The process heat provided by the off-gas from the three reactors was used for power generation. The oil retorting reactor was operated at 520 °C to maximize the hydrogen and shale oil yield. The Fe_2O_3 solid flow rate was adjusted to enable a complete conversion of the retorting gas to H_2O and CO_2 and the steam flow was regulated to fully re-oxidize the iron-based oxygen carrier. An exergy comparison and techno-economic analysis was performed between the conventional plant and the OSR-CLH system in a realistic production scale of 375 $t \cdot h^{-1}$ oil shale. The conventional plant suffered from a larger exergy destruction within the combustion engine, meaning that the OSR-CLH system had a higher total plant efficiency of 7.3% points. However, the economic analysis indicated higher capital costs and higher production costs for the chemical looping system of approximately 23% caused by the additional system units and by the oxygen carrier as second material

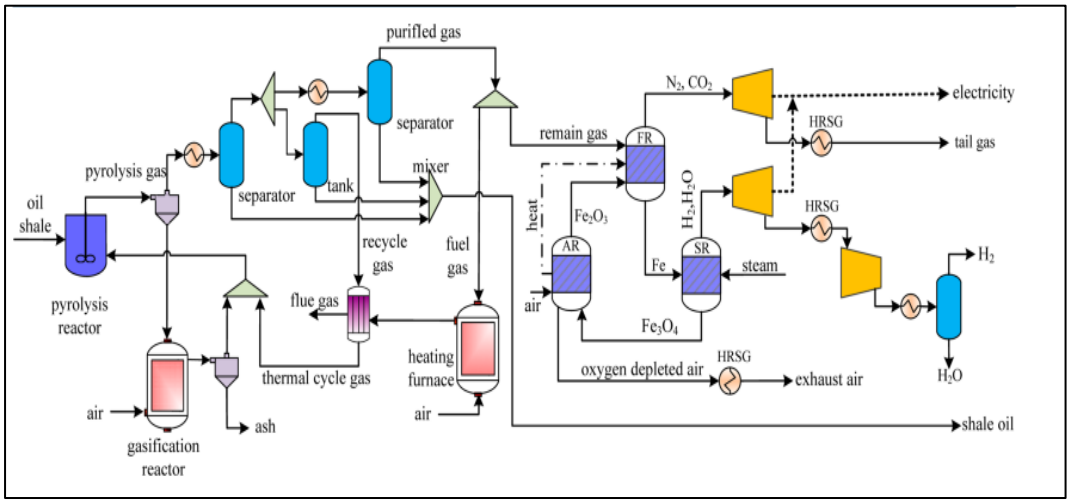

***Figure 2.13**: Simplified Flow diagram of OSR-CLH system*

Zeng at al.[106] simulated a direct coal three-reactor chemical looping plant solely for hydrogen generation using iron oxide. The fuel reactor temperature was operated at 900 °C with a solid conversion of 56.3%. Two pressure conditions 30 atm and 2 atm with a Fe_2O_3/coal flow rate ratio of 1.38 enabled a complete coal conversion. A pressure increases beyond 30 atm reduced the coal conversion efficiency. In the steam reactor, a temperature of 700 °C and a steam/Fe ratio of 1.9 ensured a complete oxidation to magnetite while optimizing the steam conversion irrespective of the selected system pressure. The two operation conditions, pressurized and atmospheric, yielded total efficiencies of 79.69% and 71.36% respectively with carbon capture rates of 99%. The operation at atmospheric pressure had a lower efficiency, however, the absence of gas compressors and expanders significantly lowered the plant investment cost and its complexity. A third case, which considered kinetic limitations with a lower carbon conversion of 95% yielded a total efficiency of 77.24%. The lower coal conversion led to carbon impurities in the produced hydrogen. Hence, a higher purification effort and a larger amount of tail-gas had to be taken into account. The formation of pollutants, which originated from the coal feed were considered. Chlorine was converted to HCl, whereas mercury stayed in elemental form in the fuel reactor. Both pollutants exited the system with the CO_2 stream. Sulphur formed $Fe_{0.877}S$ in the reducer and was mainly carried over to the steam and air reactor where it was re-oxidized, resulting in both H_2S and SO_2 being present in the system.

Chen et al [107] simulated the integration of a three-reactor chemical looping hydrogen system with a SOFC/gas turbine system for power generation. A shell gasifier was selected to convert bituminous coal to a synthesis gas. The reduction gas was utilized to convert an iron-based oxygen carrier to wustite at 950 °C in the fuel reactor. Pure hydrogen was generated in the steam reactor at 750 – 800 °C and supplied to a SOFC. The SOFC anode off gas, which contained 10 – 25% of hydrogen, was burned in a gas turbine. Heat recovery steam generator systems were installed downstream after the fuel reactor and the gas turbine. The combination of a CLH system with a SOFC and the utilization of pure hydrogen was expected to show advantages regarding (i) better electrochemical kinetics, (ii) the complete prevention of solid carbon formation, (iii) a better heat distribution by avoiding endothermic reforming reactions and (iv) the complete sequestration of carbon from the fuel. The plant analysis yielded an electrical efficiency of 43.53% with complete CO_2 sequestration. A higher system pressure was found to be beneficial for raising the total efficiency, while increasing reaction temperatures in the chemical looping plant had only limited effects on the overall plant efficiency. The variation of the steam reactor temperature raised the power output of the gas turbine but lowered the power output of the steam turbine, hence the two effects annulled each other.

Two-reactor chemical looping systems

Sanz et al.[108] calculated the hydrogen production cost using a two-reactor chemical looping system. A syngas stream with a mass flow of 27820 $kg \cdot h^{-1}$ produced by biomass gasification was assumed as feed. The feed stream contained high amounts of steam and a low reducing potential, thus the stream was cooled down to condense the water before entering the fuel reactor. A total of 12 reactors for handling the used feed stream was considered assuming two reactors in reduction mode per each reactor in oxidation mode. The system calculations were based on thermodynamic considerations of the Baur-Glaessner diagram. The reduction off gas was burned to provide heat for the system. Under the consideration of equipment costs, amortization and operation costs a hydrogen production of 4786 $t \cdot y^{-1}$ with production costs of 2.13 $€ \cdot kg^{-1}$ hydrogen was obtained. Comparative data based on a conventional water-gas-shift system resulted in production costs of 1.76 $€ \cdot kg^{-1}$. The techno-economic evaluation indicated higher investment, operation and maintenance costs (O&M) for chemical looping hydrogen systems compared to state-of-the art technology. The high degree of technological complexity and the small number of large-scale applications are the two main cost factors. However, under the consideration of costs per energy output the direct biomass chemical looping system has the lowest costs due to the high system efficiency and low carbon capture energy penalty.

Chen at al. [109] combined an iron oxide based two-reactor cyclic water-splitting system with a nickel oxide based chemical looping combustion unit[108]. Syngas, produced by coal gasification in a shell gasifier, was used as a feed. The oxygen carrier was cycled between magnetite and wustite, thus syngas was not fully converted in the Fe fuel reactor. This lean gas reduced the nickel oxide in a second fuel reactor. The Ni-looping cycle was closed by oxidation with air. A pure hydrogen stream was generated in the iron cycle, while the nickel cycle yielded a pure carbon dioxide stream. Both streams were expanded separately for power generation and heat recovery. Two cases were investigated, the first using a supplementary firing unit to increase the turbine inlet temperature of the oxygen deplete air gas stream. Hence, carbon emissions were produced with a carbon capture efficiency of 69.54%. The second cases omitted the supplementary firing unit and enabled a complete carbon sequestration. The total equivalent efficiency for both cases were 70.75% and 57.9% respectively. Operation parameters were varied to optimize the electrical power efficiency and the hydrogen yield for co-generation. A flexible production ratio of hydrogen and electricity was achieved by varying the iron oxide solid flow rate. The hydrogen production efficiency was optimized by raising the steam flow and the temperatures in the steam reactor and air-reactor. The addition of an inert support to the nickel oxide improved the heat integration in the system and the hydrogen efficiency. Generally, a trade-off between hydrogen production efficiency and total efficiency was visible, hence a raised hydrogen yield was accompanied by a reduction in power efficiency. Both efficiencies were elevated with higher iron fuel reactor temperatures but at the cost of dropping carbon capture rates.

Evaluation of operation parameters on the OCs performances

Kathe et al.[110] analyzed CH_4 as fuel in a three-reactor chemical looping hydrogen system using an iron oxide as oxygen carrier supported by Al_2O_3. Sensitivity analyses were executed to maximize the hydrogen production efficiency. Initial thermodynamic simulations explained the benefits of a counter-current moving bed of reactants and solid material compared to a co-current fluidized system. This operation mode reached the thermodynamic constraints of redox cycling more efficiently, thus lowering the required steam/solid ratio to reach a defined solid conversion. Additionally, a higher fuel/solid ratio was possible, while maintaining a complete fuel conversion. An increase of support material increased the reactor outlet temperature and the solid conversion at a fixed solid/CH_4 ratio, which enabled a full conversion of methane without the risk of coking. A value of 50 wt% Al_2O_3 was found to be optimum.

The sensitivity analysis of Kang et al.[111] based on a linear empirical kinetic model suggested a content of 20 wt% of Fe2O3 on ZrO2 as suitable content. The reaction temperatures in the steam and fuel reactor reactors were key to minimize the bed material input. In both reactors, an increase in the temperature reduced the required solid inventory to an optimum temperature value. Beyond the optimum, a contrary behaviour was observed in the steam reactor, which was related to the exothermic nature of the reaction and the unfavourable equilibrium.

Kathe et al.[110] analysed the steam conversion and outlet temperature, based on the oxygen carrier composition by adjusting the steam/solid ratio, steam conversion and outlet temperature. A re-oxidation to 11% of solid conversion yielded the highest amount of heat released at a high steam conversion efficiency. To complete the looping cycle, re-oxidation with air and a split of the solid flow was used, which bypasses the steam reactor and is directly transferred to the air reactor. The operation parameter air flow/fuel and split ratio of solid to oxidizer/bypassing-oxidizer were specified to facilitate auto-thermal operation conditions. The final plant layout for the simulation used a solid stream split of 0.15, which bypassed the steam reactor and was directly fed into the air reactor. In addition, 9% of the natural gas feed was directly injected into the air reactor to deliver the required heat duty. Hence, the process enabled a carbon capture rate of only 90%. A hydrogen production rate of 25711 $kg \cdot h^{-1}$, while utilizing 6196 $kg \cdot h^{-1}$ natural gas and a solid conversion of 60%, was calculated and utilized in several case studies. The highest system efficiencies were obtained by performing the process at a system pressure of 10 atm and exploiting a comprehensive energy recovery, which included gas expanders and a heat recovery steam generation system (HRSG). A cold gas efficiency of 77.6% and a thermal efficiency of 75.1% was obtained compared to 72.1% and 69.7% of the reference case (a conventional SMR system). The chemical lopping system required 8% less natural gas and had a lower cooling demand and water requirement than the SMR case.

Sanfilippo et al.[112] reported that an increase in the solid circulation rate required an external electric power input, but could further enhance the hydrogen production capacity and increase the total efficiency. The simulation results indicated a total system efficiency in the range of 78 – 79%, while maintaining a full carbon capture rate. The system variation can alter the process design and capabilities significantly. For instance, an increase in thermal efficiency was obtained by reducing carbon capture capabilities, while omitting the heat recovery units and lowering the operation pressure reduced the system complexity and the capital system costs at the expense of a lower thermal efficiency.

2.6 Kinetic Studies

Several studies on the redox kinetic of the OC for chemical looping technologies were published. The kinetic modelling gives important information needed to optimize the process parameter at large scale. As previously reported, iron does not own high thermal stability and the addition of promoter and/or support is fundamental to fully exploit the OCs redox performances. However, supports and promoters actively participate in the redox system forming spinel structures which change the reduction and oxidation path of iron. Furthermore, redox kinetic activity is strongly linked to the particle's size, to the percentage of promoter added and to the method used for the OCs synthesis.

Three are three main kinetic modelling used to study the gas solid reactions: (a) diffusion-controlled models, (b) phase boundary-controlled models, and (c) nucleation and growth models.

Zhang et al. [113] analysed the reduction kinetics Al_2O_3 dopant Fe_2O_3 with different Al_2O_3 loading (25 wt% and 45 wt%) with a low concentrated CH_4 feed of 0.5%. The reduction step of $Fe_2O_3 > Fe_3O_4$, with a phase change of rhombohedral to cubic, was described with the 2D growth of nuclei, up to solid conversions of 0.7. At a higher solid conversion, a 3D nuclei growth Avrami Erofeev mechanism yielded better fitting results[113]. The reduction for magnetite to $FeAl_2O_4$ was significantly slower and described by a diffusion-controlled reaction mechanism. The 3D diffusion Jander reaction mechanism fitted best and indicated a strong correlation between the iron content of the sample and the reduction reactivity.

Nasr et al.[114] studied the reduction kinetic of a natural iron ore with CH_4. Reactions were performed in a TGA in the temperature range of 800°C – 950 °C. Based on the Hancock and Sharp method, a phase boundary-controlled mechanism was used to describe the solid conversion. The impurities in the natural ore, mainly SiO2, CaO, MgO and Al_2O_3 were expected to lower the activation energy which resulted in a value of 215 $kJ \cdot mol^{-1}$ for the reduction reaction.

Zhu et al.[115] analysed the reduction stage distribution in a fixed bed reactor under fuel breakthrough operation. Reductions were performed at 900 °C with a mixture of CO and CO_2 in a tubular reactor divided into 10 separated segments by quartz cotton. The oxygen carrier analyses indicated an uneven solid conversion caused by the reaction front with their different reduction kinetics moving through the reactor (Figure 2.14). The first two layers contained Fe and FeO with a mass percentage of 85 wt% and 7 wt% respectively, while FeO and Fe_3O_4 were found in the remaining 8 layers. In the consecutive steam oxidation, the segments 1 – 6 contributed to 90% of the produced hydrogen. The reaction rates of the reductions Fe_2O_3/Fe_3O_4 and FeO/Fe possessed similar characteristics with a rapid increase to a stable maximum. Both steps ended with a fast decline until the conversion rate dropped. Fe_2O_3 was completely reduced, while 36% of FeO remained unreacted after step 3. The second step Fe_3O_4/FeO had the slowest reduction rate, approximately one order of magnitude lower than the other two, with a continuous linear decrease and a reaction stop at a solid conversion of roughly 38%, meaning that it should be the focus of material optimization. The reaction front velocities were in the order Fe_2O_3/Fe_3O4 > FeO/Fe > Fe_3O_4/FeO. Reduction simulations of Fe_2O_3 with CO in a temperature range of 973 K – 1173 K were executed with the phase boundary kinetic model. However, the addition of 50 wt% Al_2O_3 revealed a transition from a phase boundary to a diffusion controlled kinetic model to better match the experimental results. An explanation was provided by SEM analysis. Larger pores were found in the reduced pure sample, whereas the supported oxygen carrier possessed grain clusters with reduced porosity, which are expected to hamper the gas diffusion. Kang et al.186 performed an extensive isothermal kinetic investigation on iron oxide supported with 80 wt% ZrO_2 at temperatures of 740°C – 900 °C. The reduction with methane was separated into two steps Fe_2O_3 -> FeO and FeO -> Fe, while the reduction with H_2 and CO was considered a one-stage reaction. According to the Hancock and Sharp method the phase-boundary controlled mechanism was suitable for describing all reduction and oxidation reactions except the second step of the methane reduction, which showed a linear behaviour.

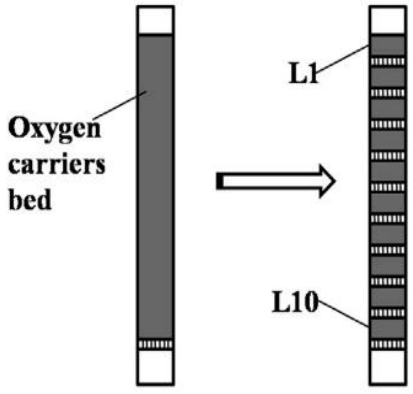

***Figure 2.14**: Simplified diagram of separated fixed bed [115].*

Hertel et al.[116] identified the two zones with a stable conversion which corresponded to the reduction zones of Fe_3O_4/FeO and FeO/Fe described by the Baur-Glaessner diagram. Stable zones were separated by transition periods, which are induced by limited gas-solid reaction rates. The simulation results indicated that the travel time of the reaction zones is 3–4 orders of magnitude of the gas phase movement.

Monazam et al.[114] analysed the reduction kinetics of Fe_3O_4 particles to FeO with 20% hydrogen in a thermogravimetric analysis system. Changing values were obtained for the activation energies, depending on the solid conversion initially decreased from 23 to 8 kJ·mol-1 (0.025 < solid conversion < 0.1) followed by an increase to 47 kJ·mol-1 (0.1 < solid conversion < 0.33) and finally declined to 30 $kJ \cdot mol^{-1}$ (0.33 < solid conversion < 1), suggesting a double-step reduction kinetic. In a temperature range of 700 – 800 °C a 1D nucleation growth model including an induction period was used to describe the reaction process. At temperatures beyond 900 °C the induction period diminished, and the single-step nuclei growth reaction became dominant. A similar approach was used for the reduction kinetics of Fe_2O_3 with CH_4 (15 – 35 vol%) in a temperature range of 973-1090 K. However, the kinetic models did not properly describe the reaction. The analysis of the activation energy corresponding to the solid reduction degree indicated a descending trend from 56 to 36 kJ·mol-1 with the conversion progressing from 0.1 to 0.5. Hence, a multi-step parallel model with a superposition of a first order reaction and a nucleation model was applied. Activation energies for the two reaction steps of 34.4 ± 0.5 kJ·mol-1 and 39.3 ± 1.6 kJ·mol-1 were obtained.

Ksepko et al.[117] compared the reduction of Fe_2O_3 supported on 20 wt% TiO_2 with a bimetallic sample of Fe_2O_3/CuO supported on Al_2O_3 (60/20/20 wt%) with hydrogen in the temperature range of 600 – 950 °C. The reaction model of a first order reaction and a phase boundary-controlled mechanism was found to be suitable for the Fe_2O_3 sample, whereas the 3D diffusion Jander equation and the first order reaction yielded better results for the reduction of the bimetallic oxygen carrier.

Jeong et al.[118] investigated the redox kinetics of iron oxides with three different main iron phases FeOOH, Fe_2O_3 and Fe_3O_4 with initial surface area of 93.5, 7.5 and 1.7 $m^2 \cdot g^{-1}$. Hence, the transformation to bulk Fe_3O_4 with a homogenizing of the different grain sizes was observed. The Jander equation was used to determine the kinetic parameter of the redox reaction. It was suggested that the reduction and oxidation of magnetite led to the highest reaction rate and lowest activation energy. Liu at el.194 investigated the reduction kinetic of wustite particles in a fluidized bed using H2 and CO. The solid reduction and the formation of metallic iron were divided into three separated conversion stages. The first stage with a solid conversion of $0 < X < 0.05$ was identified as the partial depletion of oxygen in wustite. In the second stage $0.05 < X < 0.2$ surface nucleation and the formation of isolated Fe grains took place. The reaction mechanism was controlled by dissociative adsorption and described by a linear reaction model. The final stage $0.2 < X < 1$ was identified as the thickening of the iron particle with a

final formation of a uniform Fe product layer and the changing of the reaction rate to a diffusion limiting system. The random pore model was able to describe the solid conversion reactions. The three stages were also measured when mixtures of H_2 and CO were applied resulting in a superposition of their non-interacting reduction rates. The hydrogen reduction rate was significantly faster than the CO reduction rate but the overall reduction rate was dominated by the slow diffusion of oxygen atoms in the solid particle.

3. Materials and Methods

3.1 Introduction

The optimization of the OCs properties aimed to improve both redox performances and thermal resistance of the active metal is still one of the key issues in the field of pure H_2 production by CLH technology. The ideal OCs should own high reactivity, fast reaction kinetics, high thermal stability and environmentally safe nature. Furthermore, the choice of the OCs is also strictly connected to its cost, which directly affects the hydrogen final price. Based on the published research works, Fe-based materials seems to be the most promising candidate [119][120]. The main advantages of using iron are its high redox activity, low cost and its safe nature. However, the poor thermal stability of pure Fe makes its use on high temperature redox processes not trivial. Fe particles, in fact, suffer from sintering/agglomeration undergoing to a fast deactivation after few redox cycles when the reaction temperature is higher than 600°C. This deactivation reduces the capability of the material for uptake and release of oxygen, basically due to the loss of specific surface area [121]. Additionally, Fe owns catalytic activity towards many side reactions that produce carbon when carbonaceous reductants are used[122]. As a consequence, the presence of Fe increases the risk of carbon deposition on the reduced Fe particles during the reduction step, favouring the production of hydrogen contaminate by CO[123] during the oxidation step[122] .

One of the objectives of this work is to synthetize Fe-base materials able to resist to a high number of redox cycles without losing efficiency. Therefore, structural promoters, Al_2O_3, MgO and CeO_2, are added to the Fe-based OCs, synthetized by coprecipitation. In the case of Al_2O_3 and MgO, the influence of the ratio between Fe and promoters on the OCs redox activity is deeply investigated, adding different promoter weight percentage (40 wt% and 2wt% of the sample mass).

To improve the resistance to carbon deposition and increase the yields of pure H_2, the influence of MnO_2 on iron oxide redox performances was also studied. The effect of the MnO_2 addition on the redox activity of Fe-based materials were investigated first using a fixed bed of powders of MnO_2 and commercial Fe_2O_3 physically mixed. However, due to the showed low resistance to high temperature of Fe_2O_3 powders, the MnO_2 was included in the Fe-based material by the synthesis of triple oxides such as Fe_2O_3-structural promoter-MnO_2, where MnO_2 was added in a weight percentage of 1 wt%.

The last part of the study was dedicated to the tests using doped Fe_2O_3 Foam (98wt% Fe_2O_3-2wt% Al_2O_3) manufactured by Freeze- casting (FC) technique, a highly porous material, suitable for a possible scale-up of the fixed bed system. The doped Fe_2O_3 foams were synthetized at the Department of Science of Materials and Transportation, University of Seville, by the research group of Prof. Sepulveda.

3.2 Synthesis methods

Co-precipitation method

The Fe-based OCs were prepared by co-precipitation method. The metal precursors, Fe $(NO_3)_3$*$9H_2O$, Ce $(NO_3)_3$*$6H_2O$, $Al(NO_3)_3$*$9H_2O$, $Mg(NO_3)_4$*$6H_2O$, $Mn(NO_3)_3$*xH_2O, were dissolved in deionized water. All the metal nitrates salts were supplied by Sigma Aldrich. The solution was heated using a magnetic stirrer until the temperature reached 70 °C. For the sample with CeO_2, Al_2O_3 and MnO_2, a 30% ammonia solution was gradually introduced into the mixture to increase the pH of the solution to 9. Whereas for the sample with MgO a solution of 37% wt of NaOH was used as precipitating agent in order to reach the pH value (pH =13) required for the complete precipitation of magnesium hydroxide [124]. The solution was then aged for 12 h at room temperature. Afterward, the resulting precipitate was washed with distilled water until neutrality, filtered and finally dried at 110°C for 24 h. The solids particles were calcined in a muffle furnace at 350 °C for 2 h followed by other 2 h at 900 °C. Finally, the particles were crushed and sieved to get powders in the size range of 20-125 μm.

Citrate method

The doped Fe_2O_3 foams were synthetized by citrate method (sol gel) followed by Freeze Casting Technique. In the citrate method, a concentrated solution of the metal nitrates was mixed with an aqueous solution of citric acid by fixing at unity the molar ratio of citric acid to the metal cations. Water was evaporated from the mixed solution at 80 °C until a viscous gel was obtained. The gel was kept at 100 °C overnight, ground and finally calcined at 800 °C for 5 h [125]. The resulting powders were later crushed and sieved to separate particles within 160–200 μm in diameter.

Freeze casting technique

The FeFOAM samples were synthetized by Freeze Casting Technique, the method needed a further reduction of the particle size by ball milling down to 0.2 μm in diameter. A 5 vol.% powder suspension in camphene (Sigma Aldrich, Spain) was then obtained by ball-milling at 60 °C for approximately 12 h. First 3 wt% of dispersant agent KD4 (oligomeric polyester provided by CRODA Ibérica) was mixed for 30 min in camphene, and the powder was subsequently incorporated and ball-milled for 8 h. Finally, 20 vol.% polystyrene (Sigma Aldrich, Spain) with a MW = 350,000 g mol−1 was added as a binder and mixed for another 3 h. Both organic additives were formulated according to the initial powder load and were incorporated sequentially to aid in the proper particle dispersion. The camphene suspension was then poured into a 30 mm in diameter by 15 mm in height PFTE mould, preheated at 60 °C placed inside an incubator. Directional solidification was promoted by running water at 42.5 °C through the mould base and gradually reducing the incubator temperature until reaching complete sample

solidification. A slow solidification rate was employed to enhance pore enlargement during the Freeze Casting process. Finally, after demoulding, and a 3-day camphene sublimation process at ambient conditions under forced airflow, the sample is sintered in air at 600 °C for 2 h for organic-specimen burn-out, plus a sintering of 1100 °C for 2 h for particle sintering. After the sintering, the sample as-fabricated measures approximately 10 mm in height by 24 mm in diameter[126]. Later, the diameter is reduced to 10 mm to match the diameter of the tubular fixed bed, where it is tested in CLH.

3.3 Oxygen Carrier Characterization

The obtained Fe-based particles were characterized by X-ray powder diffraction (XRPD) superficial and morphological analysis. XRD patterns were acquired using a Philips Analytical PW1830 X-ray diffractometer, equipped with a Ni β-filtered Cu Kα (1.54056 Å) radiation, in the 2θ range from 5 to 90° with a step size of 0.02° and a time for step of 3.5 s. The data were collected with an acceleration voltage and applied current of 40 kV and 30 mA, respectively. The crystalline phases in the resulting diffractograms were identified through the COD database (Crystallography Open Database – an open access collection of crystal structures)[127] .

Surface area and porosity were determined by N_2 adsorption–desorption isotherms acquired at −196 °C using a Micromeritics Triflex analyzer (Micromeritics Instrument Corp.). The adsorption-desorption isotherms were acquired in the p/p 0 range from 0.01 to 0.99. Isotherm analyses were performed using the 3Flex Version 4.05 software. Samples were previously outgassed at 300 °C for 4 h. The BET equation was used to determine the specific surface area.

A morphologic investigation of samples was performed using a High Resolution-Field Emission Scanning Electron Microscope (HR-FESEM, AURIGA Zeiss).

The amount of carbon on particle surface was evaluated by elemental analysis (Eurovector EA3000).

The sample names, their mass composition and the synthesis method used are summarized in Table 3-1

***Table 3-1**: List of samples synthetized in this thesis.*

Sample	**Mass composition**	**d_p particles**	**Synthesis method**	**Type of Fe-based material**
Fe_2O_3	100% Fe_2O_3	< 5 µm	**Commercial**	Powder
Fe_2O_3	100% Fe_2O_3	150-20 µm	Co-precipitation	
Al_2O_3 promoter				
60Fe40Al	60 wt% Fe_2O_3 40wt%Al_2O_3	150-20 µm	Co-precipitation	
98Fe2Al	*98 wt%* Fe_2O_3 2 wt% Al_2O_3	150-20 µm	Co-precipitation	
FeFOAM	*98 wt%* Fe_2O_3- 2 wt% Al_2O_3	d_p=1 cm, H=1 cm	Citrate method Freeze Casting	Foam Cylinder
MgO promoter				
60Fe40Mg	*60 wt%* Fe_2O_3 40 wt% MgO	150-20 µm	Co-precipitation	Powder
98Fe2Mg	*98 wt%* Fe_2O_3- 2 wt% MgO	150-20 µm	Co-precipitation	
CeO_2 promoter				
60Fe40Ce	*60 wt%* Fe_2O_3 40 wt% CeO_2		Co-precipitation	
Al_2O_3 and Mn_2O_3 promoters				
98Fe1Al1Mn	*98 wt%* Fe_2O_3 1 wt% Al_2O_3 1wt% Mn_2O_3	150-20 µm	Co-precipitation	
97Fe2Al1Mn	98wt% Fe_2O_3 2 wt% Al_2O_3 1wt% Mn_2O_3	150-20 µm	Co-precipitation	

3.4 Experimental Set-Up

The experiments were conducted in a fixed-bed reactor (quartz, ID 9 mm, length 300 mm) heated by an external electric heater at the desired temperature (675 °C-700°C-750°C). Both the reduction and oxidation steps were conducted at ambient pressure. All tests are performed with a constant carrier gas flowrate (Argon flowrate = 250 mL/min). Ethanol and water flowrates are set to 4 mL/h and fed at the top of the reactor by syringe pumps (KD Scientific); before entering in the reactor, both ethanol and water are vaporized in an evaporator heated at 230 ° C. In the reduction phase the ethanol is fed for different reduction times while in the oxidation phase distilled water was fed until complete oxidation of the solid bed particles. Between the reduction and oxidation phase, the reactor was purged with a flow of pure argon. Liquid products were separated by condensation and analysed through GC-MS (Agilent 5973) while gas composition was detected in an on-line mass spectrometer (Hiden QGA, Quantitative Gas Analyser); the analysis method used measure H_2, CO_2, CO, CH_4, C_2H_4 and Ar concentrations in terms of molar percentage. A non-dispersive infrared sensor (Comet) was also used to detect the CO content in the oxidation step when concentration was less than 10 ppm, value required for PEMFC application. Figure 3.1 shows a simplified scheme of the laboratory plant used

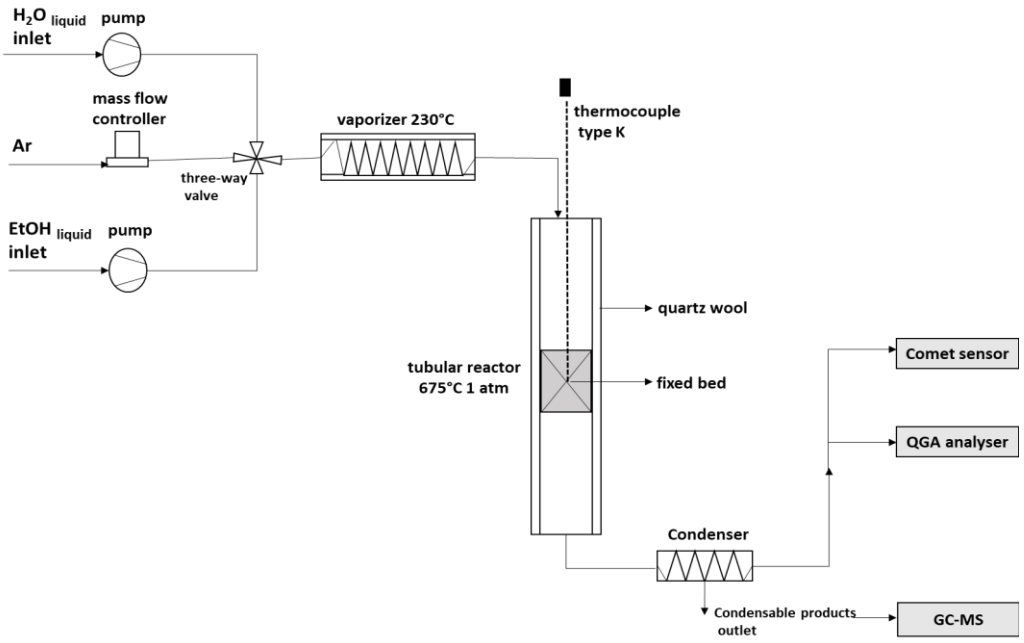

Figure 3.1 *Schematic process diagram adopted for the experiments*

Experimental data evaluation

The volumetric flow rate of Argon ($F_{Ar,}$ NL· min^{-1}) fed to the system is constant and equal to 0.250 NL· min^{-1}. Therefore, the flow rate of the total gaseous stream (F_{tot}, NL· min^{-1}) in each step of the process, can be calculated according to equation 3.1:

$$F_{tot} = \frac{F_{Ar}}{1 - \sum y_i} \tag{3.1}$$

Where y_i represents the volumetric fraction of the compound detected in the gaseous stream (i = H_2,CO, CO_2, CH_4,C_2H_4). Knowing F_{tot}, the flowrate of each compound F_i (NL· min^{-1}) is calculated according to equation 3.2:

$$F_i = F_{tot} * y_i \tag{3.2}$$

Finally, the total volume V_i(NL) of the compounds produced in each step is calculated as:

$$V_i = \int_{t1}^{t2} F_{tot} * y_i \, dt \tag{3.3}$$

Where the difference between t_1 and t_2 correspond to the duration of the reduction/oxidation step.
The amount of H_2 produced in oxidation is strictly connected to the reduction degree of the solid particles. In order to have an indication about the reduction degree of the Fe-based particles and about the real amount of the samples that participate at the redox system, it is also introduced the efficiency of the process, E(%) (equation 3.4):

$$E_p(\%) = \frac{V_{H2}}{V_{H2\ theoretical}} * 100 \tag{3.4}$$

Where $V_{H2\ theoretical}$ is the maximum amount of H_2 that can be produced. $V_{H2\ theoretical}$ is calculated considering that Fe_2O_3 is completely reduced to Fe in the reduction step and Fe is fully oxidised to Fe_3O_4 in oxidation. V_{H2} represents the measured amount of H_2 in the experimental oxidation step.

3.5 Thermogravimetric analysis (TGA)

TGA tests were carrier out to evaluate the oxygen transport capacity of the synthetises OCs focusing the attention on their redox kinetic properties and their cycle stability.

The redox tests were performed both in isothermal and in temperature programmed reduction modes, placing 10 mg of the sample in a platinum crucible in the TGA system. The small mass of the sample is needed to avoid mass transport phenomena. The simplified scheme of the TGA system used for the analyses is reported in Figure 3.2.

In a Temperature programmed ramp, the OCs is heated from 100 °C to 900°C with a heating rate of 10°C min^{-1} by feeding 100 $mL \cdot min^{-1}$ of 5 vol% H_2, diluted in Argon flow.

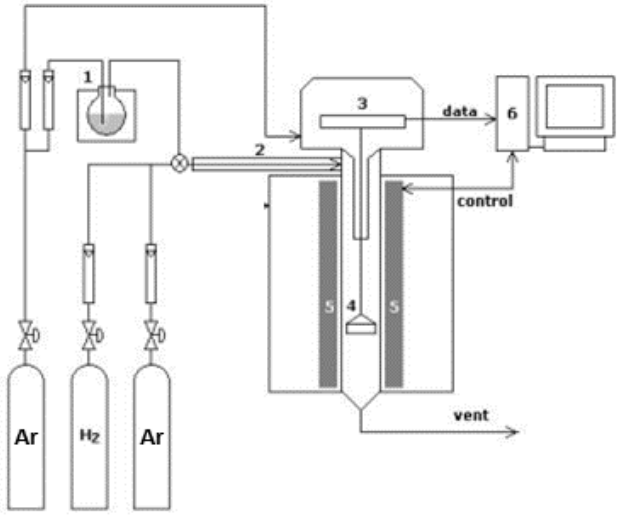

***Figure 3.2**: Schematic diagram of thermal gravimetric analyser (TGA) system:1) water reservoir and bubbler.2) gas pre-heater.3) Electric balance.4) Sample crucible.5) Heater.6) Computer of control*

The deconvolution of the TPR profiles is also performed in order to identify the effect of the promoter in the mechanism and kinetics of reduction of iron oxides. In fact, deconvolution allows to break down every single OC reduction step, providing useful information to deepen the properties of the material.

The deconvolution of TPR results is performed according to the Gaussian–Lorentzian Cross Product expression as a fitting function (E.q.3.0) using PeakFit software (Systat Software Inc.)

$$y = \frac{a_o}{1 + a_3\left(\frac{x - a_1}{a_2}\right)^2 exp\left[(1 - a_3)^{1/2}\left(\frac{x - a_1}{a_2}\right)^2\right]} \quad (3.0)$$

where a_0 is the amplitude, a_1 is the centre of the curve, a_2 is the width ($a_2 > 0$), and a_3 is related to the shape of the curve ($0 \leq a_3 \leq 1$, the pure Lorentzian occurs with $a_3 = 1$ and the pure Gaussian occurs with $a_3 = 0$).

4. OCs characterization

Before tests, the synthetized samples are fully characterized by XRD, BET and SEM analyses in order to evaluate the influence of promoters on the final chemical composition of the sample and on the sample morphology. In this chapter the characterization results are showed briefly; a deep analysis of the sample composition and morphology is reported in the subsequent chapters, where the effect of the addition of the promoter on sample activity is studied.

4.1 XRD and BET analyses

The results of XRD and BET analyses of the synthetized samples are summarized in Figure 4.1 and in table 4-1, respectively. Table 4-1 reports also the main crystalline phases detected by XRD analysis.

A) Commercial and synthetized Fe_2O_3

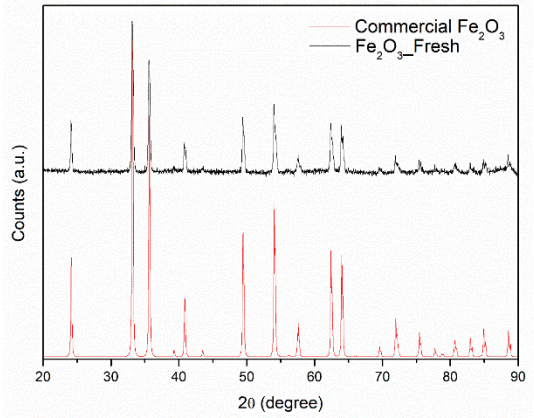

B) 60Fe40Al and 98Fe2Al

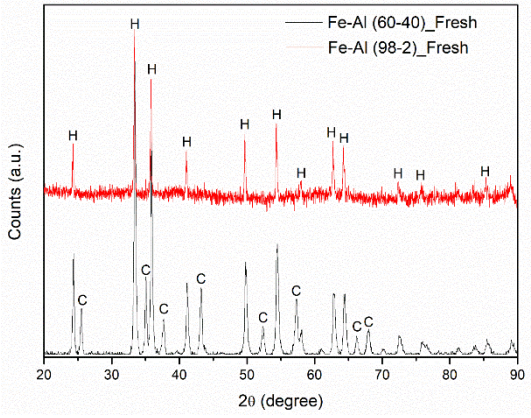

C) 60Fe40Mg and 98Fe2MgO

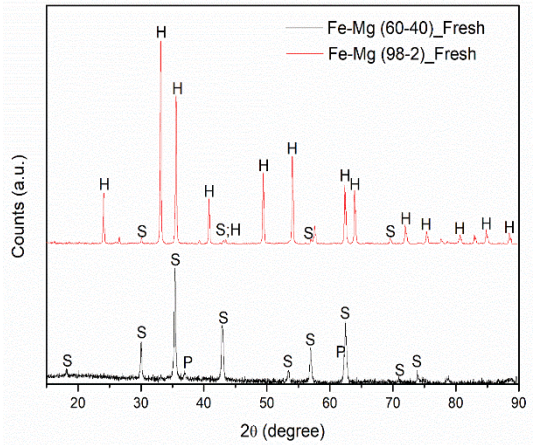

D) 60Fe40Ce

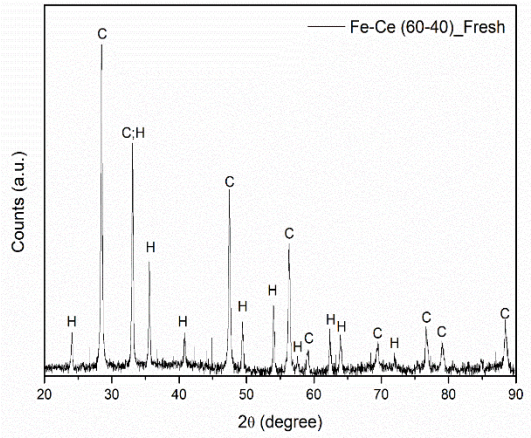

E) 98Fe2Al1Mn and 97Fe2Al1Mn

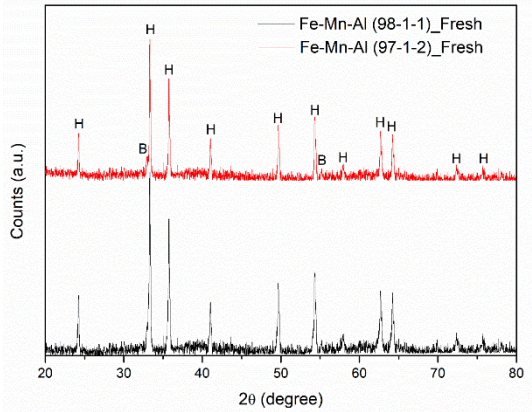

***Figure 4.1**:XRD analysis of the sample examined in this study (H: Fe_2O_3, C: Al_2O_3, S: $MgFe_2O_4$, B: Mn_2O_3).*

***Table 4-1**: Main crystalline phases relieved by XRD analysis and BET values of all samples.*

Sample	**Main Crystalline Phases**	**BET value (m^2*g)**
Commercial Fe_2O_3	Fe_2O_3	50
Fe_2O_3 (synthetised)	Fe_2O_3	0.74
60Fe40Al	Fe_2O_3, Al_2O_3	9.00
98Fe2Al	Fe_2O_3	1.58
60Fe40Mg	$MgFe_2O_4$, MgO	9.76
98Fe2Mg	Fe_2O_3, $MgFe_2O_4$	1.32
60Fe40Ce	Fe_2O_3, CeO_2	2.79
97Fe2Al1Mn	Fe_2O_3, Mn_2O_3	0.13
98Fe1Al1Mn	Fe_2O_3, Mn_2O_3	0.21
FeFOAM	Fe_2O_3	0.61

The XRD the BET results highlight the key role played by the structural promoters in the CLH process. Based on BET results (Table 4-1), the promoter addition changes the sample's morphology, increasing the BET surface area of the sample in different proportion depending on the amount of promoter added. Except for the sample of commercial Fe_2O_3 which has very low particles dimension (< 5 µm), the highest BET surface area is obtained with the sample having the 40 wt% of MgO added, equal to 9.76 m^2·g which decreases to 1.32 $m^2 \cdot g^{-1}$ when only 2 wt% of MgO is present in the sample (98Fe2Mg).

The pure Fe_2O_3 synthetized by the same method and having the same particles dimension has a BET of only 0.74 m^2·g. Similar behaviour is registered when Al_2O_3 is added to the sample; the presence of 40 wt% of Al_2O_3 in the sample mass increases the BET surface area up to 9.00 $m^2 \cdot g^{-1}$ while a reduced amount of 2 wt% shows a BET value of only 1.58 $m^2 \cdot g^{-1}$.

For the sample 60Fe40Mg a chemical interaction between promoter and iron oxides is detected, suggesting that MgO addition affects not only the sample morphology but also the iron oxides redox mechanism, interacting with iron forming spinel structures namely magnesium ferrite ($MgFe_2O_4$).

In the following chapter the promoters/iron interaction and its influence on the sample reactivity will be deeply discussed.

4.2 SEM analysis

SEM of commercial Fe_2O_3 and OCs synthetized by coprecipitation

SEM analyses on the fresh samples are conducted to evaluate the influence of promoters on Fe_2O_3 morphology. Figure 4.2 reports the SEM images of the fresh samples tested in this work.

A) Commercial Fe_2O_3

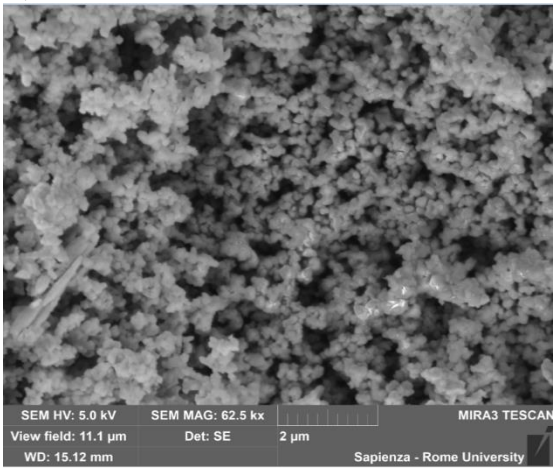

B) Fe_2O_3

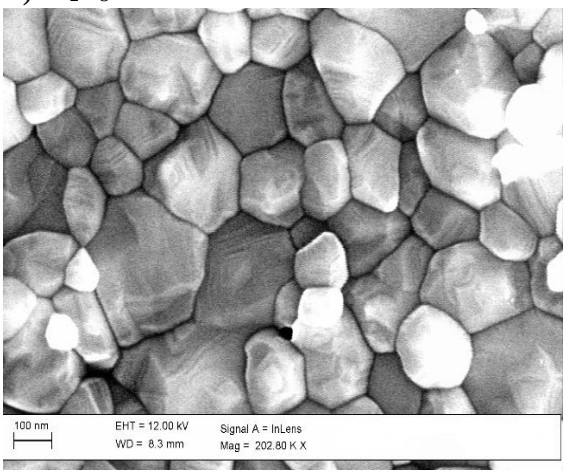

C) 60Fe40Al

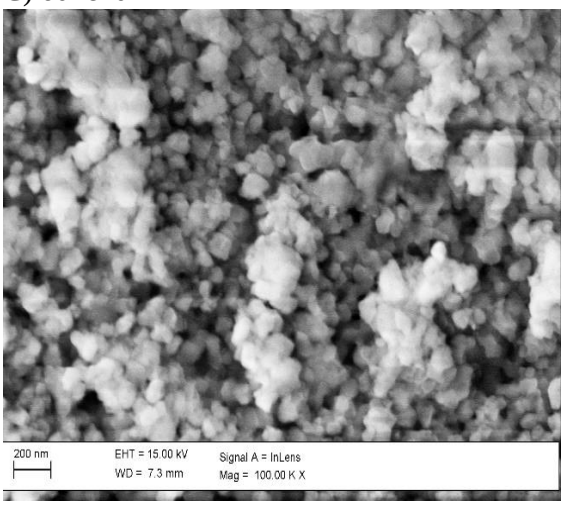

D) 98Fe2Al

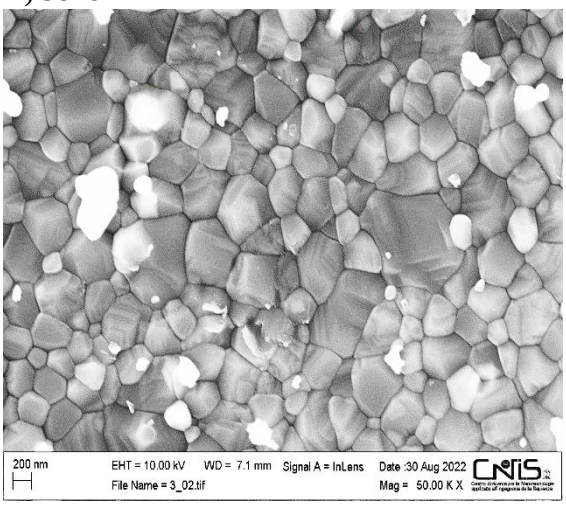

E) 60Fe40Mg

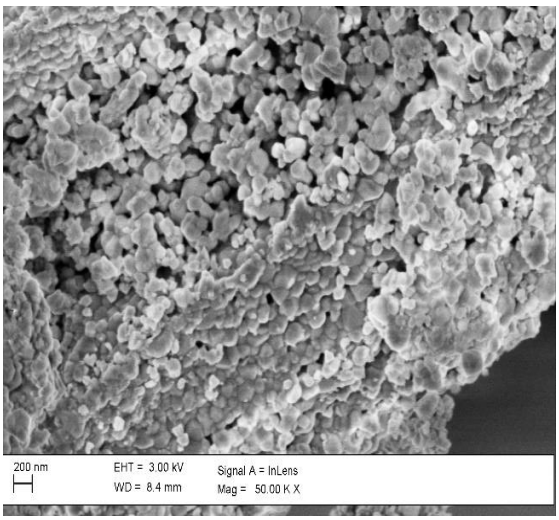

F) 98Fe2Mg

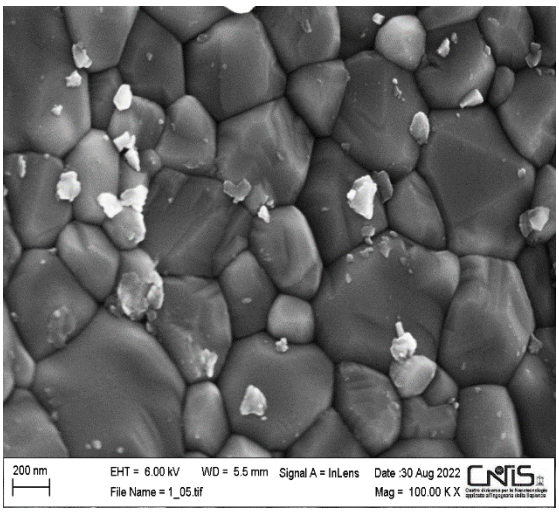

G) 60Fe40Ce

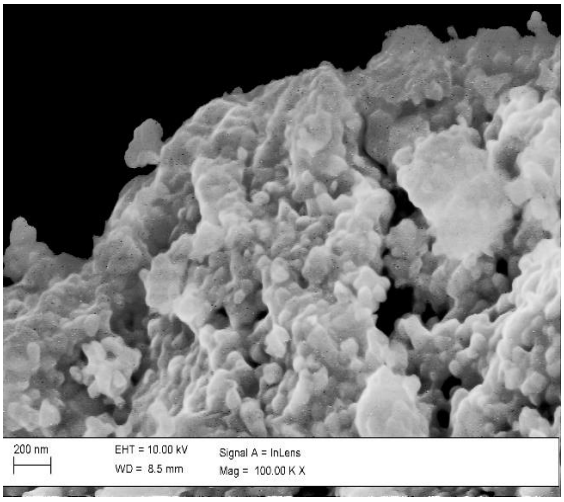

H) 98Fe2Al1Mn

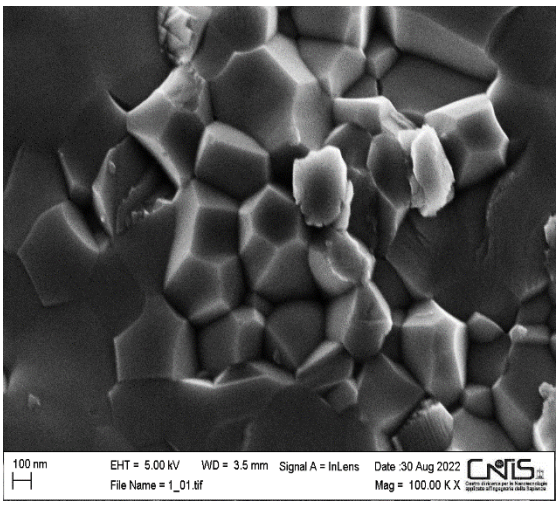

I) 97Fe2Al1Mn

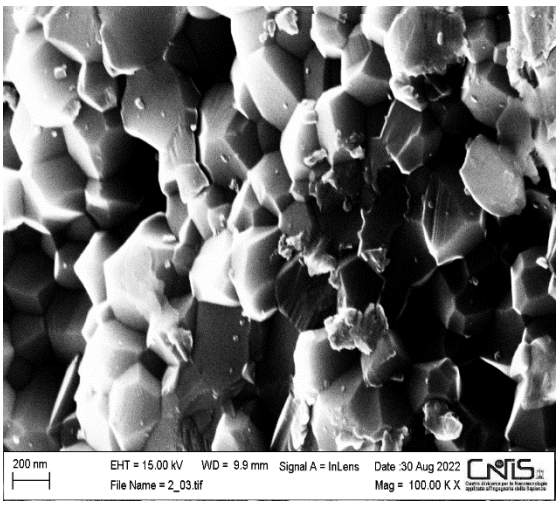

***Figure 4.2**:SEM images of the commercial Fe_2O_3 (a) and fresh samples synthetized by coprecipitation technique (B-I).*

The effect of promoter addition on sample morphology is confirmed also by SEM analyses. The pure synthesized Fe_2O_3 (Figure 4.2 B) appears as no-porous material while with the addition of 40 wt% of promoters (Al_2O_3, MgO and CeO_2) a clearly increases of sample's porosity is always visible (Figure 4.2 C, E and G, respectively). However, at lower promoter concentrations in the sample mass (2 wt %, figure 4.2 D, E, H and I) the positive effect on the sample porosity introduced by promoter disappears.

SEM analysis FeFOAM sample

The SEM images of the fresh FeFOAM at different section are reported in figure 4.3.

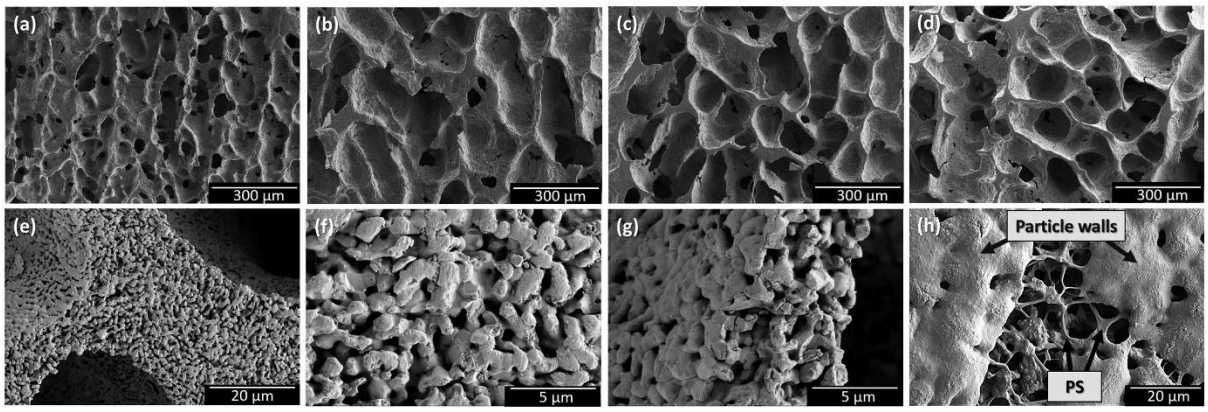

Figure 4.3*: SEM images of fresh FeFOAM sample at different sample height: 0 mm (a), 3 mm (b), 6 mm (c) and 9 mm (d). Details of porous cell wall (e)(f), cross section (g). (h) the FeFOAM before sintering*[126]

The SEM images confirm the feasibility to produce a highly interconnected porous structure by the freeze casting technique. However, looking at the figures 4.3 (A-D) a pore size decreasing is detected from the top to the bottom of the foam.

The average pore size of the FeFOAM sample is 29 µm at 0 mm, 100 µm at 3 mm ,117 µm at 6 mm and 127 µm at 9 mm.

5. Pure H_2 production using bioethanol as sources of reducing agents: commercial Fe_2O_3 and effect of MnO_2 addition

5.1 Introduction

To assess the process performances and understand the feasibility of using bioethanol as renewable reductant in the production of pure H_2, preliminary tests using commercial Fe_2O_3 were performed. The temperature and pressure are maintained constant and equal to 675°C and atmospheric pressure, respectively. The redox temperature is chosen based on thermodynamics and kinetics evaluation of iron oxides reductions, easily extrapolated by the Bauer Glasser diagram (figure 5.1). The Bauer Glasser diagram describes the thermodynamics of iron oxides reduction with H_2 and CO (Figure 5.1) [128]. The diagram shows the stability area of different iron oxides as a function of the reaction temperature and on the gas oxidation degree (GOD). The GOD is the ratio of the oxidized gas species over the sum of the oxidized and oxidable components and it gives an indication about the reducing power of the gaseous stream: low GOD value corresponds to a high force reducing stream.

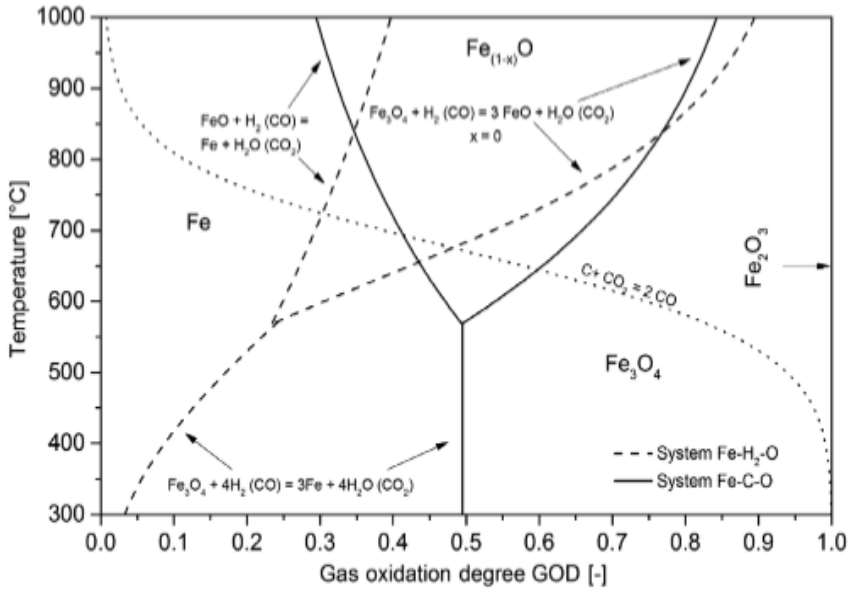

Figure 5.1:*Bauer Glassner diagram for the Fe-O-H_2 (dashed lines)and Fe-O-C systems(plain line), including the Boudouard equilibrium for 1 bar and a carbon activity equal to 1*[128].

As reported in the diagram (figure 5.1), when the aim is the complete iron oxides reduction to Fe, the reduction by H_2 should be performed at the highest possible temperature, as the stable area of the Fe

metal increases linearly (temperature range 550°C-1000°C (dashed line)). This leads to an increase in theoretical gas utilization. The Fe–O–C system (plain lines) shows an opposite trend, the iron region decreases with temperature. However due to kinetic limitations, the reduction with CO is usually performed at high temperature, otherwise, the reduction progress would be very slow and cannot be done economically.

According to these thermodynamic evaluations, the experiments are conducted at 675°C with the aim to make possible to obtain the complete reduction to metallic Fe and, at the same time, to increase the energetic efficiency of the process by working at the lowest possible temperature ensuring high pure H_2 yields. However, the elevated temperatures needed for the efficient iron oxides reduction to Fe is in contrast with the characteristic of the produced Fe to acts as cracking catalyst, promoting the solid carbon formation when a carbonaceous reductant (i.e ethanol) is used. If carbon is not completely consumed by iron oxides reductions, it reacts with steam at the beginning of the oxidation step, producing H_2 contaminated by CO due to the occurring of gasification reaction. Thus, aiming at the pure H_2 production, the ethanol decomposition pathway and the reducibility of iron oxides with solid carbon must be key issues for the process and need to be carefully addressed.

In this chapter, the thermal ethanol decomposition is studied at the same operative condition adopted for the redox tests (675°C and 1 bar), feeding ethanol on an inert SiO_2 bed. Once examined the data on ethanol decomposition and once the carbon formation mechanism was understood, Fe redox tests, aimed to reduce the carbon deposition phenomena, are performed. The deposition of carbon on the iron surface was attributed to the lack of oxygen on the OC during the reduction step, that occurs when all the Fe is in metallic form. To control this phenomenon different ethanol amounts were fed by changing the duration of the reduction step to prevent the presence of ethanol when all the particles are completely reduced and so the carbon deposition. The tuning of the ethanol amount fed is fundamental to produce a pure H_2 stream in oxidation. The catalytic activity offered by iron in the ethanol decomposition pathway is also discussed.

The last part of the chapter is dedicated to CLH tests of mixed Fe_2O_3 and MnO_2 powders, with the aim of increasing the H_2 yields and thus the process efficiency. Commercial MnO_2 powder is added to Fe_2O_3 to improve the carbon consumption in the reduction step exploiting the high oxygen lattice mobility of manganese oxide. Furthermore, as explained later in the chapter, the efficiency is increased when MnO_2 is added also due to the redox capacity of MnO_2 which will be reduced and oxidized by steam producing additional H_2.

5.2 Experimental procedures

The experiments were conducted in a fixed-bed reactor (quarz , ID 9 mm, length 300 mm) heated by an external electric heater at a constant temperature of 675 °C. Both the reduction and oxidation steps were conducted at ambient pressure. The solid bed is constituted by a powder mixture of Fe_2O_3 (Sigma-Aldrich, dp< 5 μm, ≥ 99%), silicon dioxide SiO_2 (Sigma-Aldrich, granular ≥99.9%) and manganese dioxide MnO_2 (Sigma-Aldrich dp< 10 μm, 99.9%). SiO_2 was added to avoid iron particles agglomeration and to uniform temperature profile in the bed; In a typical test, 1,59 g of Fe_2O_3 and 0.53 g of SiO_2 were used, while in the experiments with MnO_2, an amount of powder of 10 wt% and 40 wt% to Fe_2O_3 was added. In the reduction phase, three different ethanol feeding times, keeping constant the ethanol flowrate, were considered (25 min, 9 min and 7 min) corresponding to different amount of ethanol, while in the oxidation phase, distilled water was fed until complete oxidation of the solid bed particles. The blank experiments for the evaluation of thermal ethanol decomposition pathway are conducted feeding only ethanol at 675 °C for 2 h loading the reactor with inert SiO_2 (2 g). At least three redox cycles were considered in each test.

The bench scale plant used for the experiments is described in detail in Chapter 3.

5.3 Experimental results

Thermal Ethanol Decomposition

At the operating conditions adopted in the reduction step (675 °C and 1 atm), ethanol participates in a complex system of reactions. In order to evaluate the main compounds resulting from its thermal decomposition and the feasibility of its use as a source of reducing gases (H_2 and CO and C), a blank experiment was carried out feeding only ethanol in a SiO_2 bed. The several compounds resulting from ethanol decomposition are grouped based on their physical state (gas, liquid and solid) to understand the influence of the different reactions in which ethanol is involved.

The typical molar composition of the gaseous mixture produced as a function of time is reported in Figure 5.3 while the carbon balance and the yields of each phase (gas, liquid and solid) are reported in tables 5-1 and 5-2, respectively.

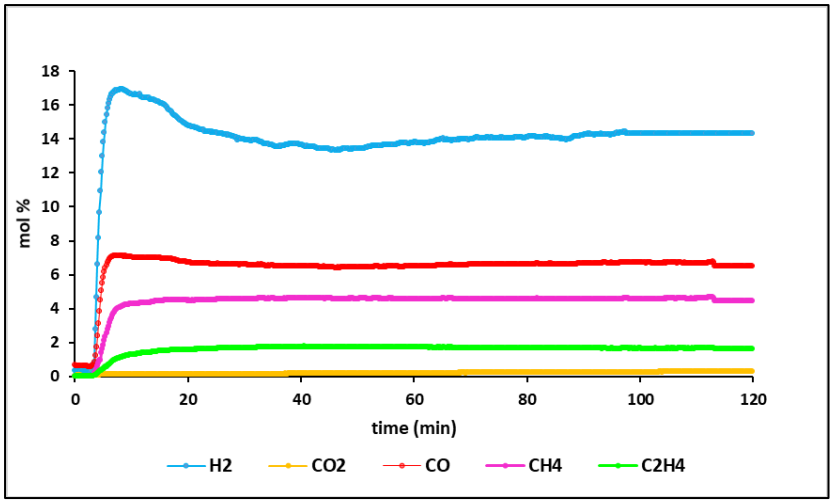

***Figure 5.2**: Molar concentration of the principal gaseous compounds resulted from thermal ethanol decomposition at 675 °C and 1 atm.*

As shown in figure 5.3, a gaseous mixture mainly constituted by H_2 (15.06%), CO (7.13%), CH_4 (4.51%) and by traces of C_2H_4 (1.7x%) and CO_2 (0.22%) is produced from thermal ethanol decomposition. The concentration of each species remains constant throughout the test. This result confirms that ethanol can be successfully used as a source of reducing agent in the proposed system.

At the end of the test, the condensable products were collected, weighted and finally analysed; from GC-MS analysis, only water is detected in the condensate, suggesting that ethanol is completely converted. Traces of carbon deposits on the silica bed were also detected. The amount of coke produced was quantified, heating the sample at 750 °C for 2 hours in a muffle furnace in the presence of air, and then calculating the difference in weight of the sample before and after the treatment.

Table 5-1 shows the carbon balance of the ethanol decomposition calculated considering all the three phases (gas, liquid and solid) produced. The carbon balance confirmed the validity of the results, although a difference of 0.87% between the input and output carbon moles was identified; nevertheless, being this deviation within the error range of the instrument, it is considered negligible.

***Table 5-1**: Carbon balance for thermal ethanol decomposition experiments at 675 °C and 1 bar pressure.*

	IN	OUT			
	C_2H_5OH	**Gas**	**Liquid**	**Solid**	**Δmol C**
mol C*	0.274	0.237±0.001	0.000	0.028±0.002	0.009
% mol C	100.00	86.86±0.10	0.000	10.34± 0.15	

* The measurements are repeated three times; dispersion evaluates through semi-dispersion.

Where:

mol C_{C2H5OH} = total mols of carbon fed with ethanol;

% mol C_{Gas} = 100*mols of carbon in the gaseous compounds/mol C_{C2H5OH};

% mol C_{liquid} = 100*mols of carbon in the condensable products/ mol C_{C2H5OH};

% mol C_{solid} = 100*mols of carbon of coke on the SiO_2 bed/ mol $C_{C2H5OH;}$

Δmol C = mol C_{C2H5OH} - sum of mol C products

Table 5-2 shows the gas, liquid and solid yields obtained from ethanol decomposition (molar basis). These data are reported to understand better which is the predominant phase in which ethanol is decomposed. As desired, looking at the results in table 5-2, ethanol is principally converted into gaseous products (95.13 mol%). At the same time, condensable (H_2O) and solid compounds (coke) are obtained only in a very low amount (0.86 mol% and 4.05 mol%, respectively) and can be considered by-products. However, despite the low coke yield detected (4.05 mol%), to use ethanol in this technology, the reactions leading to coke formation should be totally inhibited.

Table 5-2*:Molar yields of products resulting from thermal ethanol decomposition at 675°C and 1 bar pressure.*

	$C_2H_5OH_{in}$	Products	Gas	Liquid	Solid
mol*	0.137	0.698 ± 0.011	0.664 ± 0.010	0.006 ± 0.001	0.028 ± 0.001
Yield (mol%)	0.00	100.00 ± 1.10	95.13 ± 1.01	0.86 ± 0.05	4.05 ± 0.15

* The measurements are repeated three times; dispersion evaluates through semi-dispersion.

Where:

mol $_{C2H5OH}$ = total mols of ethanol fed;

mol $_{products}$ = total mols of products obtained;

Gas Yield (mol%) = 100*sum of the mol of gaseous products/ mol $_{products}$;

Liquid Yield (mol%) = 100* mols of water/ mol $_{products}$;

Solid Yield (mol%)= 100* mols of coke / mol $_{products;}$

Based on the results obtained and considering the mechanisms proposed in the literature [129], a simplified thermal decomposition scheme is reported. At the operating condition adopted in this work (675 °C and 1 atm), ethanol starts to decompose mainly in H_2, CO and $CH_{4,}$ according to equation 5.01 [130]. However, ethanol also undergoes in dehydration reaction producing ethylene (equation 5.02) and water, although with low yields. Furthermore, due to the high-temperature, methane undergoes cracking reaction (equation 5.03), producing additional H_2 and carbon deposits.

$$CH_3CH_2OH \leftrightarrow CO + H_2 + CH_4 \qquad \Delta H = +49\ kJ/mol \qquad (5.01)$$

$$CH_3CH_2OH \leftrightarrow C_2H_4 + H_2O \qquad \Delta H = +45\ kJ/mol \qquad (5.02)$$

$$CH_4 \leftrightarrow C + 2H_2 \qquad \Delta H = +74.35\ kJ/mol \qquad (5.03)$$

Several studies about the use of ethanol report two additional reactions which can be responsible for the coke formation:

$$2CO \leftrightarrow CO_2 + C \qquad \Delta H = -173\ kJ/mol \qquad (5.04)$$

$$C_2H_4 \rightarrow carbonaceous\ polymeric\ compounds\ (coke) \qquad (5.05)$$

The proposed set of equations, except for Boudouard reaction (equation 5.04), are all endothermic reactions, and thus thermodynamically favoured at high temperatures. Therefore, it is worth underlining that, at the high temperatures adopted, the conversion of CO into carbon according to Boudouard reaction is thermodynamically less favoured.

The formed carbon can be converted into gaseous products according to equation 5.06 and 5.07, reacting with water coming from ethanol dehydration reaction (equation 5. 02).

$$C + H_2O \leftrightarrow CO + H_2 \qquad \Delta H = +131\ kJ/mol \qquad (5.06)$$

$$CO + H_2O \leftrightarrow CO_2 + H_2 \qquad \Delta H = -41\ kJ/mol \qquad (5.07)$$

Determination of the optimal reduction time of iron oxides

In order to make possible the use of ethanol in this process, the study of the operating conditions that inhibit coke formation during the reduction step is essential. As said before, the deposition of carbon takes place when the carbon cannot react anymore with Fe oxides and so the ethanol feeding time becomes a key parameter. For this purpose, tests at different reduction time, ranging from 7 to 25 minutes, for one redox cycle and in the presence of Fe_2O_3 are performed. Figure 5.3 reports the flow rate of analysed species: the first peak regards the reduction step, while the second the oxidation step.

A)

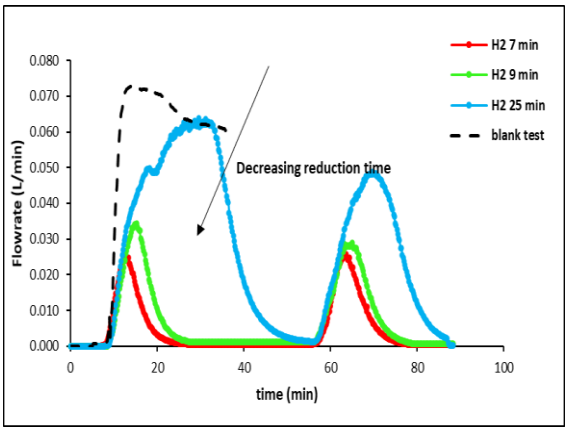

B)

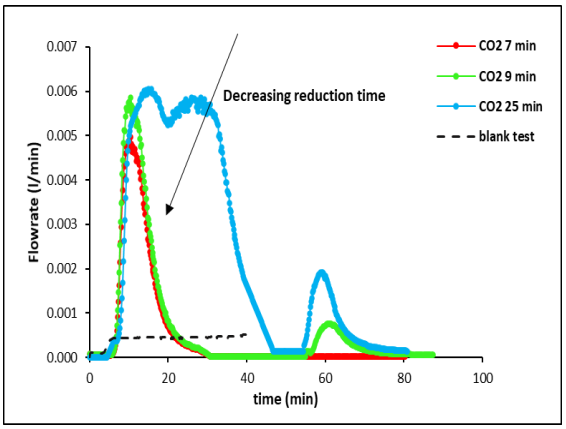

C)

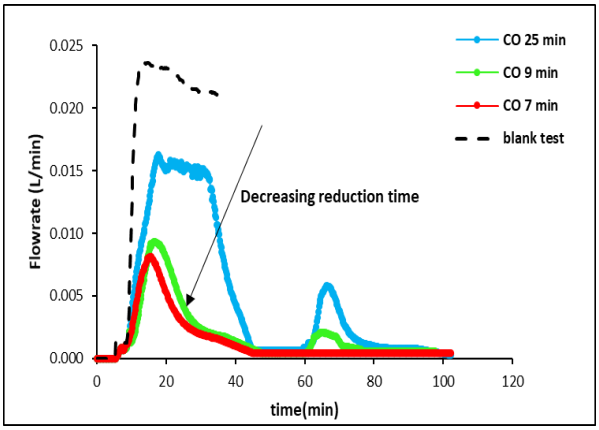

D)

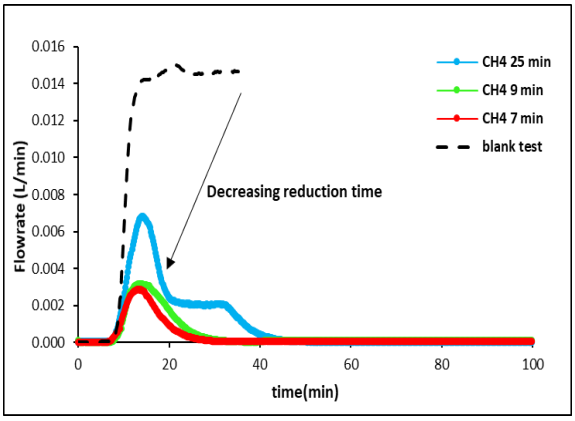

E)

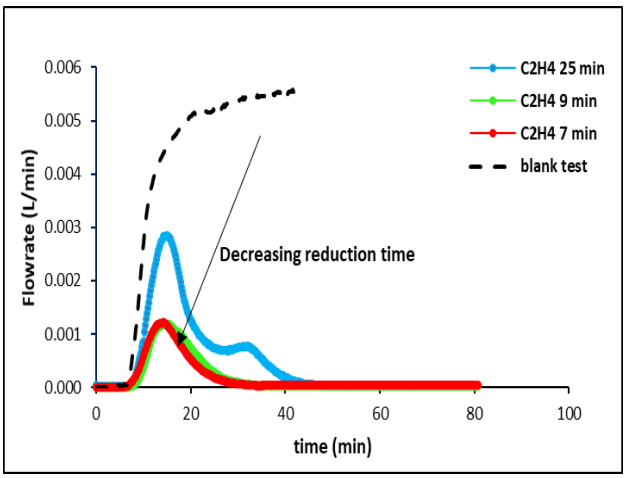

***Figure 5.3**: Flow rate trend of the main compounds produced during one redox cycles at different reduction time, comparison with a blank test (dashed line):A)H_2; B)CO_2; C)CO; D)CH_4; E)C_2H_4*

The data obtained in the reduction step changing the ethanol feeding time were compared with those produced by thermal ethanol decomposition (see Figure 5.4). However, in order to make a consistent comparison only the data with a feeding time of 25 min were used. This because, looking at the figure 5.4, it is clear that times of 7 and 9 minutes are not enough to let the formation of a stable concentration of the produced gaseous species.

Except for CO_2, all the species obtained have lower flow rates than those detected in the thermal ethanol decomposition on SiO_2; this result was expected; the gases produced by ethanol decomposition are oxidized by the oxygen lattice of Fe oxides producing CO_2. Looking at figures 5.4 D and 5.4 E, for a reduction time of 25 minutes, it can be noticed that CH_4 and C_2H_4 present a peculiar flow rate trend as a function of time, showing a shoulder for times higher than 15 minutes. The decrease of CH_4 and C_2H_4 after this time confirms the Fe^0 catalytic activity in hydrocarbon cracking reactions, promoting the formation of carbon and also of H_2 (figure 5.4 A). These results suggest that the consumption of CH_4 and C_2H_4 is strongly related to the degree of the solid bed reduction and, in particular, to the Fe^0 formation. The catalytic activity of metallic iron on the CH_4 cracking reaction is analyzed in different studies in which a complete CH_4 conversion into pure H_2 and carbon is achieved already at a temperature of 700 °C [131],[132].

Based on the results collected by the experimental tests and on the literature data, a simplified reaction scheme for the reduction of iron oxides with ethanol is proposed (figure 5.5). At long reduction time, when the formation of the first Fe^0 particles occurs, cracking reactions of CH_4 and C_2H_4 are catalyzed by Fe particles leading to the formation of additional H_2 and active carbon (equation 5.03). The produced carbon in close contact with iron oxides can act as an additional iron reducing agent producing CO as a by-product; CO can reduce again iron oxide particles producing Fe and CO_2. When the complete reduction of iron oxides to Fe^0 has been reached, the formed carbon is not consumed anymore, and thus it begins to be deposited on the bed particles. This mechanism can be seen in figures 5.4 D and 5.4 E, relative to CH_4 and C_2H_4 respectively, where for reduction time of 25 minutes, the concentration of these two species begin to decrease as first Fe^0 particles are formed and, when the whole bed is reduced, their concentration is stabilized to a constant value and the coke deposition begins to occur. The output amounts of CO and CO_2 are, at this point, regulated by the Boudouard equilibrium reaction.

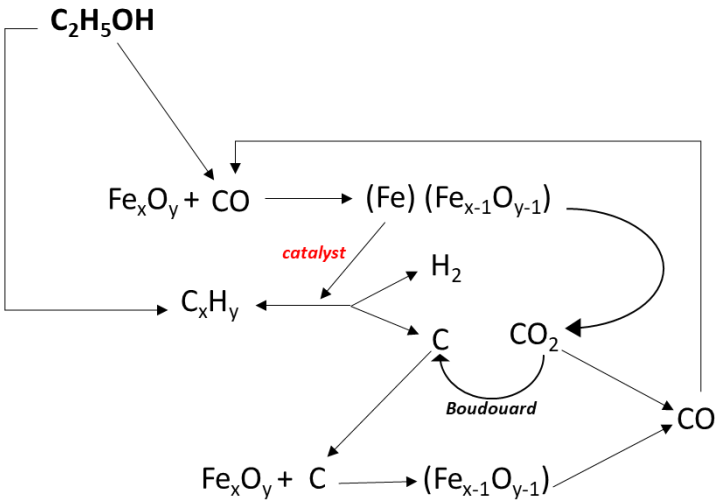

Figure 5.4: *Mechanism proposed of CO iron oxides reduction with ethanol (675°C, 1 bar).*

Looking at the oxidation peaks reported in figure 5.4, it can be noted that pure hydrogen is obtained only for reduction times of 7 minutes. This result suggests that the reduction time parameter significantly influences the composition of the gas mixture in oxidation due to the occurrence of the coke formation for higher reduction times. When a reduction time equal to 25 minutes and 9 minutes is used, an increase of CO_2 and CO flowrate is registered; the presence of carbonaceous compounds is detrimental when pure H_2 is the target of the process. In fact, the carbon produced in reduction in the oxidation step can react with water vapor by gasification reaction (equation 5.06) producing CO and CO_2 (equation 5.07) in the outlet gas. The purity of the hydrogen stream is obtained at the expense of the hydrogen yield, in fact as it is clearly visible from figure 5.4 A, the reduction time highly influence the amount of hydrogen produced. This result is expected since when the reduction time is decreased to avoid the deposition of carbon the reduction degree of the Fe particles is lower and thus their ability to produce H_2. However, only through an inferior reduction of the solid bed, it is possible to obtain a pure flow of H_2 in the oxidation phase and therefore to make possible the use of ethanol to produce H_2 as a feed for fuel cells.

Table 5-3 summarizes the volume of species obtained during the oxidation step for the three times of reduction and the efficiency of the process calculated according to equation 5.08, where H_{2e} is the hydrogen measured from the experimental tests and H_{2t} is the theoretical value.

$$E\ (\%) = (H_{2e} / H_{2t}) * 100 \qquad (5.08)$$

H_{2t} was calculated hypothesizing that the whole amount of Fe_2O_3 loaded was reduced to metallic iron in the reduction step and then totally oxidized to Fe_3O_4 in the presence of steam. The volumes of the several species produced in each test are calculated by integrating the peaks shown in Figure 5.4.

The results collected in table 5-3 confirm that, when reduction times of 25 minutes and 9 minutes are used, carbon deposition occurs. This behavior is also confirmed by the amount of the experimental hydrogen produced, which exceeds by 4.4% the theoretical maximum hydrogen value (H_{2tv}=0.595 L) at a reduction duration of 25 minutes. Decreasing the reduction time to 7 allows the production of pure H_2 during the oxidation step, meaning that coke deposition is negligible. However, hydrogen production was significantly lower than the theoretical value (process efficiency of 35.29%) since a period of 7 minutes is not enough to achieve the complete reduction of Fe_2O_3 particles.

***Table 5-3**: Amounts of species produced during the first oxidation peak at the operating conditions of 675°C, 1 atm and different reduction time (25 min, 9 min and 7 min).*

t_{red} (min)	$H_{2\,e}$ (L)	CO (L)	CO_2 (L)	E%
25*	0.621 ± 0.005	0.058 ± 0.004	0.015 ± 0.003	104.40 ± 0.50
9*	0.257 ± 0.005	0.029 ± 0.012	0.007 ± 0.010	43.86 ± 0.50
7§	0.210 ± 0.069	0.000	0.000	35.29 ± 6.90

* The measurements are repeated three times; dispersion evaluates through semi-dispersion.

§ The measurements are repeated ten times; dispersion evaluates through standard deviation.

Figure 5.5 shows a typical trend of the molar concentration of the compounds produced in 3 redox cycles using 7 minutes as reduction time. During the reduction steps, the gaseous mixture was mainly constituted by H_2, CO, CH_4, CO_2 and C_2H_4 traces. In the subsequent oxidation phase, pure H_2 was always achieved.

It should be noted that during the reduction step, the peak is reached at the end of the 7 minutes due to the interruption of the feed. On the contrary, in the oxidation step, the reaching of the hydrogen peak is independent from the feeding time of water but depends only on the oxidation state of iron. The H_2 concentration comes back to zero when iron particles are completely oxidized to Fe_3O_4.

In addition, in the first reduction, the areas of H_2 and CO peaks are smaller than that in the subsequent reduction peaks; this occurs because the iron oxide at the beginning of the process is in the form of Fe_2O_3, which requires a higher amount of reducing agents to reach the metallic state (Fe^0) than that needed for magnetite. In fact, starting from the first oxidation peak, the restored iron oxide is magnetite

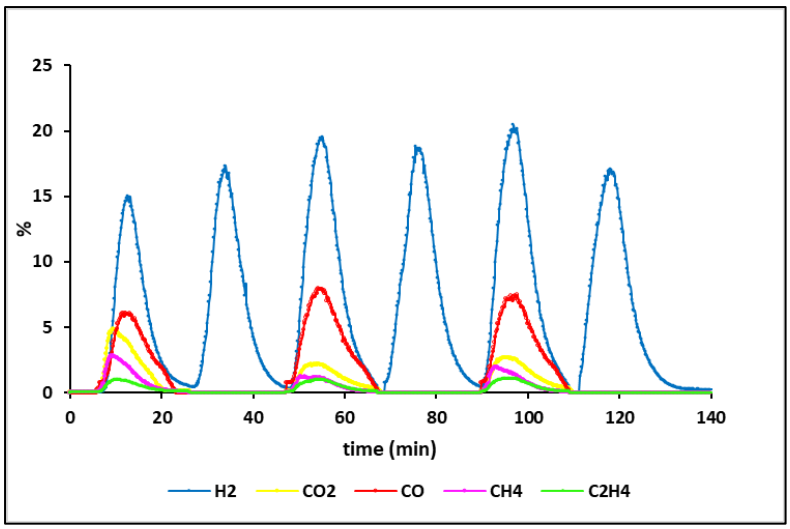

***Figure 5.5**: Molar concentration of the gaseous species produced at three consecutive redox cycles(675°C, 7 minutes of reduction)*

Stability of the system at consecutive redox cycles

Currently, the research for metal oxides with high reactivity and stability is still the aim of several studies on the steam-iron process due to the low resistance of this material to high temperatures. Therefore, to verify the stability of the used material, an experiment with a high number of redox cycles (10 cycles) was conducted.

The amounts of hydrogen obtained, and the process efficiency related to each redox cycle are shown in table 5-4.

***Table 5-4**: Amounts of H_2 produced and process efficiency in 6 redox cycles*

N cycles	H_2 (L)	E (%)
I cycle*	0.211 ± 0.058	35.5 ± 5.8
II cycle*	0.219 ± 0.049	36.9 ± 4.9
III cycle*	0.301 ± 0.046	50.4 ± 4.6
IV cycle§	0.269 ± 0.017	45.2 ± 1.7
V cycle§	0.184 ± 0.018	30.9 ± 1.8
VI cycle§	0.149 ± 0.012	25.0 ± 1.2
VII cycle	0.107± 0.010	18.1 ± 1.0
VIII cylcle	0.077 ± 0.009	13.2 ± 0.8
IX cycle	0.047 ± 0.005	8.0 ± 0.7
X cycle	0.0178 ± 0.004	3.1 ± 0.7

*The measurements are repeated ten times; dispersion evaluates through standard deviation.

§ The measurements are repeated three times; dispersion evaluates through semi-dispersion.

A growing trend of hydrogen produced up to the third cycle is observed, confirming that in every cycle the complete reduction of the particles is not achieved; this condition is essential to ensure the high purity of the hydrogen obtained when ethanol is used as a reducing agent since only with lower reduction grade, the coke deposition ca be avoided. However, the long-term hydrogen production is not stable under the operating conditions adopted; the efficiency of the process decreases from the maximum value of 50.4% reached at the third cycle to 25.0 % at the sixth cycle. This instability is highly likely to be found in agglomeration/sintering phenomena of Fe, which cause a reduction of the reactive surface of the bed[133]. As a result, a smaller amount of magnetite is reduced and therefore, a lower amount of Fe is oxidized. The instability of the powders used in this work suggests that the presence of inert porous support could be an effective solution to increase the reactive surface and thus to improve the process stability [134].

Influence of MnO_2 addition in the process efficiency

The results obtained so far show that in the proposed configuration system, it is possible to produce pure H_2 but with low efficiency. The addition of a compound able to enhance the degree of reduction of the solid bed avoiding coke deposition can be one of the solutions to improve the H_2 production. MnO_2 can be a good candidate due to the high mobility of the oxygen in its lattice that can contribute to the oxidation of the deposited carbon allowing to reach a higher reduction degree of the Fe oxides.
It worth to underline that MnO_x participates in the redox reaction system [135],[136]. Like Fe oxides, MnO_2 can be reduced to MnO in three steps; first MnO_2 is reduced to Mn_2O_3 (equations 4.01-4.03), then Mn_2O_3 is reduced to Mn_3O_4 (equation 4.04-4.06) which is finally reduced to MnO (equations 4.07-4.09).

The complete reduction to Mn cannot be achieved under the operating conditions adopted ($\Delta G>0$)[136].

1° step

$$2MnO_2 + H_2 \leftrightarrow Mn_2O_3 + H_2O \quad (5.09)$$

$$2MnO_2 + CO \leftrightarrow Mn_2O_3 + CO_2 \quad (5.10)$$

$$2MnO_2 + C \leftrightarrow Mn_2O_3 + CO \quad (5.11)$$

2° step

$$3Mn_2O_3 + H_2 \leftrightarrow 2Mn_3O_4 + H_2O \quad (5.12)$$

$$3Mn_2O_3 + CO \leftrightarrow 2Mn_3O_4 + CO_2 \quad (5.13)$$

$$3Mn_2O_3 + C \leftrightarrow 2Mn_3O_4 + CO \quad (5.14)$$

3° step

$$Mn_3O_4 + H_2 \leftrightarrow 3MnO + H_2O \quad (5.15)$$

$$Mn_3O_4 + CO \leftrightarrow 3MnO + CO_2 \quad (5.16)$$

$$Mn_3O_4 + C \leftrightarrow 3MnO + CO \quad (5.17)$$

In the oxidation phase MnO, in the presence of water vapor, can be oxidized to Mn_2O_3, releasing H_2 according to equation 5.18. The oxide obtained is Mn_2O_3, since to restore MnO_2, at the temperatures used, pressures higher than 3000 atm are necessary [135].

$$2MnO + H_2O \leftrightarrow Mn_2O_3 + H_2 \quad (5.18)$$

Therefore, MnO_2 plays a dual role in the steam iron process: it enhances the reduction of the iron oxides in the reduction phase and participates as active specie in the H_2 production in the oxidation step. A simplified illustration of the proposed system is reported in figure 5.6.

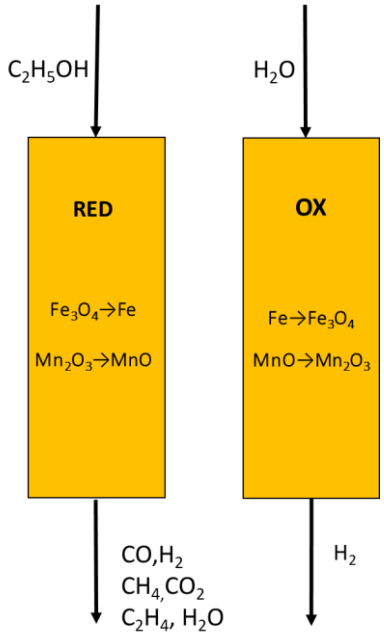

Figure 5.6: Steam-Iron Process in a fixed bed reactor using C_2H_5OH as a reducing agent and a mixture of Fe_2O_3 and MnO_2 powders as a solid bed

Tests were carried out, adding different quantities of MnO_2 powder (10 wt% and 40 wt% with respect to Fe_2O_3 weight) to investigate the effect of the amount of MnO_2 on the process efficiency.
The influence of MnO_2 addition was evaluated during three redox cycles. The amounts of H_2 produced in the oxidation step adding different amount of MnO_2 and in the presence of Fe_2O_3 alone are compared in figure 5.7 A; in all the oxidation peaks, the amounts of H_2, produced with MnO_2, were higher than those obtained using Fe_2O_3 alone. As shown in figure 5.7 B, with the addition of MnO_2, also the process efficiency was significantly improved at each oxidation cycle. From the comparison of the results obtained the optimal amount of MnO_2 was individuated to be 10 wt%.

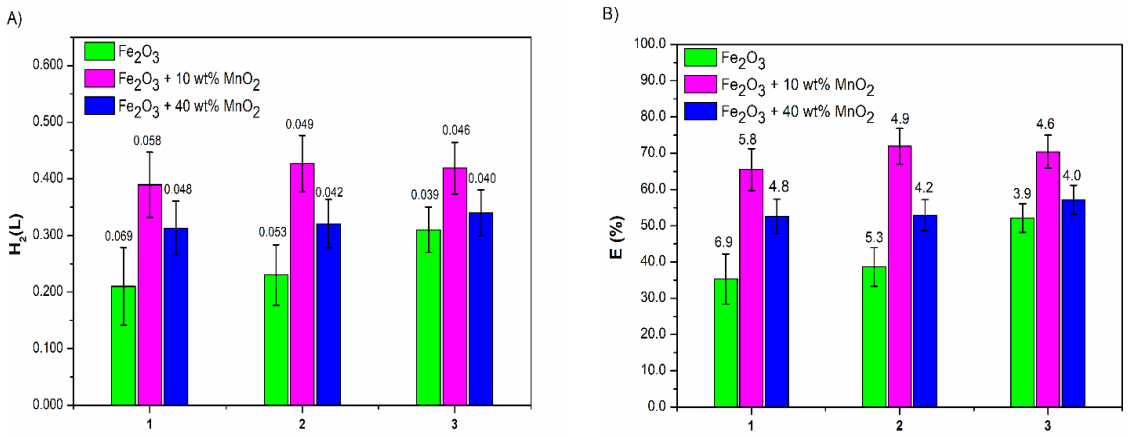

Figure 5.7: *A) Hydrogen produced during three oxidation cycles with and without MnO2; B) Process efficiency with and without the MnO_2. The measurements are repeated ten times; dispersion evaluates through standard deviation.*

In this case, in the calculation of the theoretical produced H_2 it is necessary also to consider the H_2 coming from the oxidation reaction of MnO (equation 5.18) and compare this value with the experimental amount of H_2. This comparison allows us to verify if MnO_2 behave as redox material in the process able to produce H2 together with Fe or if it can also enhance the iron oxide reduction degree as hypotized. According to the literature data, under the adopted operating conditions, MnO_2 can be reduced at MnO during the reduction step and subsequently re-oxidized to Mn_2O_3 in the oxidation phase [137]. Assuming that the whole amount of MnO_2 is reduced to MnO and then totally oxidized to Mn_2O_3, the hydrogen produced by this reaction should be equal to 0.021 L and 0.082 L for 10 wt% MnO_2 and 40 wt% of MnO_2, respectively. The difference between the H_2 produced with and without the addition of MnO_2 was calculated according to equation 5.19.

$$\Delta H_2 = H_{2e\ (Fe2O3+MnO2)} - H_{2e\ (Fe2O3)} \qquad (5.19)$$

As reported in table 5-5, ΔH_2 values were always higher than the maximum hydrogen produced by MnO oxidation, confirming that MnO_2 is not only a redox element but also improves the degree of the reduction of the iron oxides.

Table 5-5*: ΔH_2 values and process efficiency for experiments with the addition of 10 wt% and 40 wt% of MnO_2.*

N cycles	10 wt% MnO_2			40 wt% MnO_2		
	ΔH_2 (L)		E (%)	ΔH_2 (L)		E (%)
	Experimental	*Theoretical*		*Experimental*	*Theoretical*	
I cycle	0.179 ± 0.011	0.021	65.49 ±	0.103 ± 0.008	0.082	52.60 ± 4.76
II cycle	0.195 ± 0.004	0.021	71.91 ±	0.110 ± 0.007	0.082	52.94 ± 4.55
III cycle	0.103 ± 0.007	0.021	70.40 ±	0.084 ± 0.002	0.082	57.14 ± 4.85

The measurements are repeated ten times; dispersion evaluates through standard deviation.

In order to understand what is the role of MnO_x in the process, the amount of the gaseous species produced during the reduction step in three redox cycle with the addition of 10 wt% MnO_2 and in the presence of Fe_2O_3 alone are compared (figure 5.8). As shown in figures 5.8 A and 5.8 B, no significant differences in the amount of H_2 and CO are relieved; this result is unexpected because even in limited quantities also MnO_x consumes reducing agents in the reduction phase (equations 5.09-5.17). In contrast, the addition of MnO_2 resulted in a lower amount of CH_4 and a higher amount of CO_2 compared to the test performed with Fe_2O_3 alone (figure 5.8 C and 5.8 D). Finally, no differences are detected in the ethylene amount produced (figure 5.8 E).

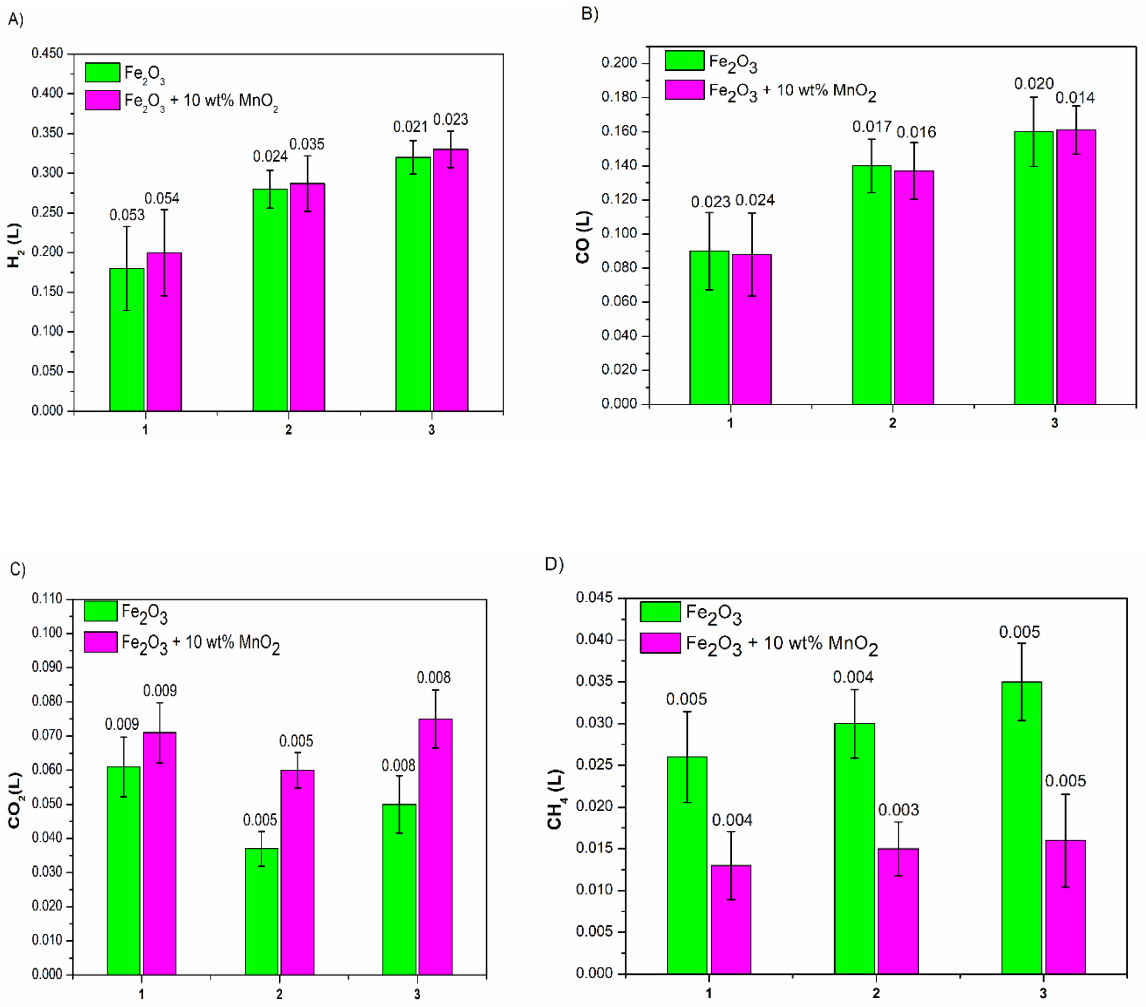

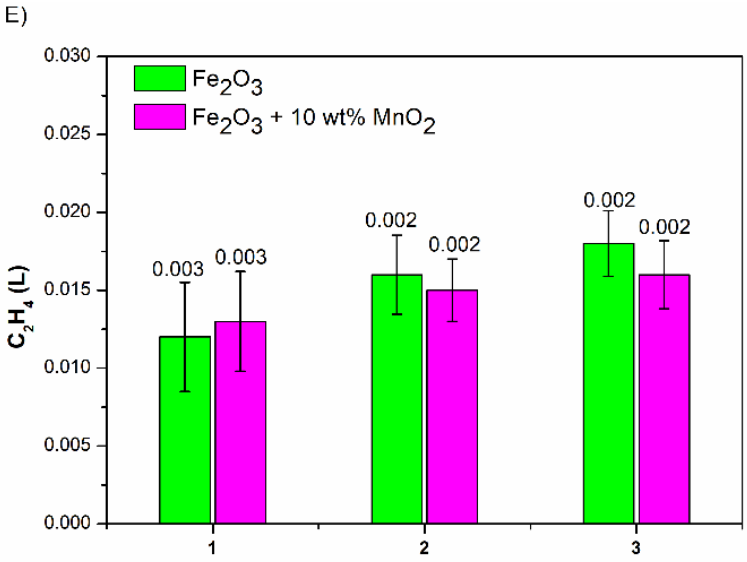

Figure 5.8: *Comparison of the amount of the species produced during the reduction step for three redox cycle with and without 10 wt% of MnO2.A) H2; B) CO; C) CO2; D)CH4; E) C2H4. The measurements are repeated ten times; dispersion evaluates through standard deviation.*

The results collected in figure 5.8 suggest that in the presence of MnO_x, the methane consumption is enhanced. Several literature studies confirm that at high temperatures, also methane actively participates in the reduction of MnO_x through reactions 17, 25 and 26 [138],[139],[135].

$$a)\ CH_4 \leftrightarrow C + 2H_2 \tag{5.20}$$

$$b)\ MnO_2 + C \leftrightarrow CO + MnO \tag{5.21}$$

Total reaction:

$$MnO_2 + CH_4 \leftrightarrow MnO + CO + 2H_2 \tag{5.22}$$

As already described for the case of iron oxides, in the MnO_x reduction a central role is played by the adsorbed active carbon resulting from methane cracking reaction (equation 5.20); MnO_x are characterized by greater reticular oxygen mobility than that of iron oxides; the MnO_x thus acts as oxygen donor during the reduction step enhancing the active carbon consumption (equation 5.21)[140] [139]. The adsorbed carbon is oxidized to CO, obtaining the complete reduction of MnO_2 to MnO and additional syngas, according to equation 5.22, is produced [138]. As a consequence, looking at the sum of reaction 5.20 and 5.21 reported as reaction 5.22, methane in presence of MnO_2 is converted into syngas avoiding its decomposition into carbon. Therefore, the additional carbon monoxide and

hydrogen produced can reduce iron oxides according to the simplified scheme already proposed in figure 5.5.

From the results obtained, it can be concluded that the addition of MnO_2 improves the reduction grade of the iron oxides fixed bed, enriching the gas phase in reducing compounds at the expense of methane and thus avoiding coke formation even at high reduction degree of the Fe oxides.

The proposed mechanism for the role of MnO_2 on the process can also explain why an increased amount of MnO_2 (40 wt%) decreases the overall process efficiency. The results obtained by the tests made adding 10 % of MnO_2 (figure 5.8 D) demonstrated that the amount of CH_4 is strongly reduced in these conditions. The addition of higher amount of MnO_2 could produce negative effect on the process efficiency. In fact if high amount of MnO_2 are available for the reduction, the CH_4 converted into carbon will reduce only a small portion of the MnO_2 present in the bed and the other amount of MnO_2 will be reduced with the syngas produced by ethanol decomposition. This phenomena will be in competition with the reduction of Fe oxides and the overall amount of H_2 and CO is used to reduce not only the iron oxides but also the additional MnO_2, decreasing the synergic effect of the use of iron and manganese oxides.

The simplified scheme which takes into consideration the effect of MnO_x addition on the iron oxides reduction system is reported in Figure 5.9.

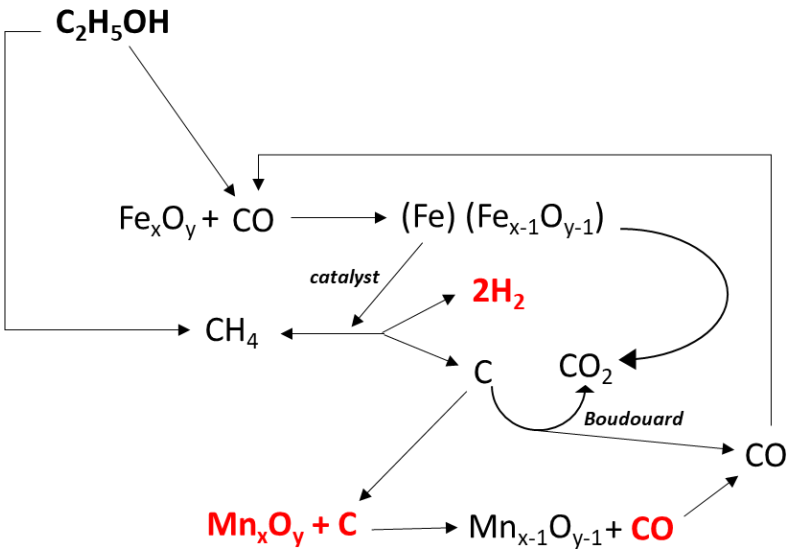

***Figure 5.9**: Effect of MnO_2 addition in iron oxides reduction with ethanol (675°C, 1 bar)*

Stability of the system in multi-redox cycles

Currently, the research for metal oxides with high reactivity and stability is still the aim of several studies on the steam-iron process. An experiment with a high number of redox cycles (10 cycles) was conducted to verify whether the powder mixture tested in this work present also good thermal stability. The test was carried out at the optimal conditions previously identified (Fe_2O_3+ 10 wt% MnO_2).
The amounts of hydrogen obtained, and the process efficiency related to each redox cycle are shown in table 5.6. The stability of the particles resulted to be poor even if the drop in process efficiency is less evident than the one obtained in the tests performed without the addition of MnO_2.

***Table 5-6**: Amounts of H_2 produced and process efficiency in 6 redox cycles*

N cycles	H_2 (L)	E (%)
I cycle*	0.389 ± 0.058	65.5 ± 5.8
II cycle*	0.427 ± 0.049	71.9 ± 4.9
III cycle*	0.419 ± 0.046	70.4 ± 4.6
IV cycle§	0.402 ± 0.017	67.2 ± 1.7
V cycle§	0.374 ± 0.018	63.9 ± 1.8
VI cycle§	0.361 ± 0.011	60.5 ± 1.2
VII cycle	0.357± 0.010	58± 1.1
VIII cycle	0.308± 0.008	50± 1.0
IX cycle	0.246± 0.010	40± 1.2
X cycle	0.196± 0.012	32± 1.2

*The measurements are repeated ten times; dispersion evaluates through standard deviation.
§ The measurements are repeated three times; dispersion evaluates through semi-dispersion.

5.4 Conclusions

The feasibility of using renewable ethanol as a reducing agent in the CLH process was demonstrated. At the adopted operating conditions (T = 675 °C and P = 1 atm), ethanol is completely decomposed in a gaseous mixture mainly consisting mainly of H_2 and CO, with high reducing activity. However, the formation of solid carbon is also favoured and in order to successfully use ethanol as a reducing agent to produce pure hydrogen, the control of the ethanol feeding time in the reduction step is crucial. The control of ethanol feeding time aims to limit the amount of solid carbon formed and to avoid the iron oxides reduction to the iron metal. This last aim is fundamental to ensure the presence of oxygen atoms in the reticular of the iron oxides, able to convert the deposited carbon into CO and CO_2 during the reduction step. A reduction time of 7 minutes seems to be the optimal value to avoid coke formation which , however, leads to a low degree of reduction of hematite and, therefore, to a poor process efficiency value. The addition of MnO_2 has a dual role in the process: it produces additional hydrogen participating in the redox cycles and increases the amount of reducing gas, allowing a better reduction of the fixed bed, avoiding coke deposition. The highest H_2 yields (0.427 ± 0.049 L) and process efficiency (71.9% ± 4.9%) were obtained, adding 10 wt% of MnO_2. Finally, extended duration test (10 redox cycles) shows that the overall process efficiency sharply decreases due to the poor thermal stability of hematite powders, making their application at industrial scale impossible.

6. The role of Al_2O_3, MgO and CeO_2 addition on steam iron process stability to produce pure and renewable H_2

6.1 Introduction

The results reported in the previous chapter demonstrated the feasibility to produce pure H_2 using bioethanol as reducing agent and Fe_2O_3 as OCs. However, the low thermal stability of pure iron oxides at repeated redox cycles led to a rapid deactivation due to particles' agglomeration and sintering phenomena, which decrease the active surface area[141][142][143]. The result highlights the fundamental role played by a support/structural promoter in the process, needed for the scale-up of the technology [144] [145] [119]..

In this work, the use of Al_2O_3, CeO_2 and MgO as structural promoter of iron is deeply studied. These materials are widely used in the field of catalysts especially as supports, thanks to their resistance at high temperature[146]. Furthermore, due to their different chemical properties they can own catalytic activity towards several reactions, includes ethanol cracking. Al_2O_3 is generally used as catalyst for cracking reactions and alcohols dehydrations to olefine due to its high concentration of Lewis acidic sites [147]. MgO is considered a promising heterogeneous catalyst support and promoter for many kinds of chemical reactions including dry reforming and hydrogenation [148][149]. MgO is used to avoid carbon deposition on the catalyst surface favouring CO_2 adsorption and promoting carbon conversion to CO, by the reverse Boudouard reaction [150][151][152]. CeO_2 has been widely used as redox catalyst in several processes such as water gas shift and catalytic methane oxidation [153]. Furthermore, it can improve the catalyst performance avoiding carbon deposition thanks the excellent mobility of its lattice oxygen atoms [150][154].

The Fe-based particles are synthetized by co-precipitation method maintaining constant the amount of promoter added to 40 wt%. The redox materials are tested in the fixed bed reactor working at 675 °C and at 1 bar. As explained in the previous chapter, the production of highly pure H_2, is achieved tuning the reduction degree of iron oxides by feeding different amount of ethanol in reduction. After the determination of the optimal amount of ethanol, the powders' stability is evaluated for 10 consecutive redox cycles.

6.2 Experimental Set Up and Procedure

The bench scale plant used for the experiments is explained in detail in Chapter 3. All experiments are carried in a fixed bed reactor maintained at constant temperature and pressure (675°C and 1 atm, respectively). All tests are conducted using 2 g of Fe-based particles as redox fixed bed. The effect of the promoters on the ethanol decomposition products was evaluated independently. The reactor was loaded only with 2 grams of Al_2O_3, MgO and CeO_2 and the tests last 1 hour. Screening tests to determine the optimal amount of ethanol fed are performed maintaining constant the ethanol flowrate equal to 4 $mL \cdot h^{-1}$ and changing the reduction time. The ethanol feeding time is strongly connected to the amount of iron loaded in the sample mass and to the accessibility of the iron active sites. The ethanol feeding time investigated in this chapter is from 4 min to 1 min.

6.3 Experimental Results

Influence of promoters on ethanol thermal cracking reactions

In this section the influence of the addition of promoters on the ethanol thermal cracking products was investigated.

As already reported in Chapter 4, ethanol thermal cracking starts at relatively low temperature (500 °C) producing low molecular weight compounds such as CH_4, C_2H_4, CO and H_2, through C-C and C-O dissociation [155]. However, the mechanism of ethanol decomposition is strongly related to the operative temperature and pressure and to the nature of the catalyst, if present [156].

When ethanol is used as reductant of iron oxides, the Fe formation influences the ethanol decomposition pathway as it acts as catalyst of light hydrocarbon cracking, promoting their conversion into H_2 and further solid carbon [131].

To evaluate the effect of each promoter (Al_2O_3, CeO_2 or MgO) on ethanol thermal cracking reactions, blank tests were carried out feeding only ethanol for 1 hour on each promoter (ethanol decomposition without Fe). The operative conditions are maintained constant and equal to that of the reduction step (675°C, 1 bar, F_{Arg}= 230 $mL \cdot min^{-1}$ and F_{EtOH} = 4 $mL \cdot h^{-1}$).

Figure 6.1 displays the trend of the main compounds detected in the gaseous phase as a function of the test duration time while Table 6-1 summarizes the molar amount of each product present in liquid, gaseous and solid phase.

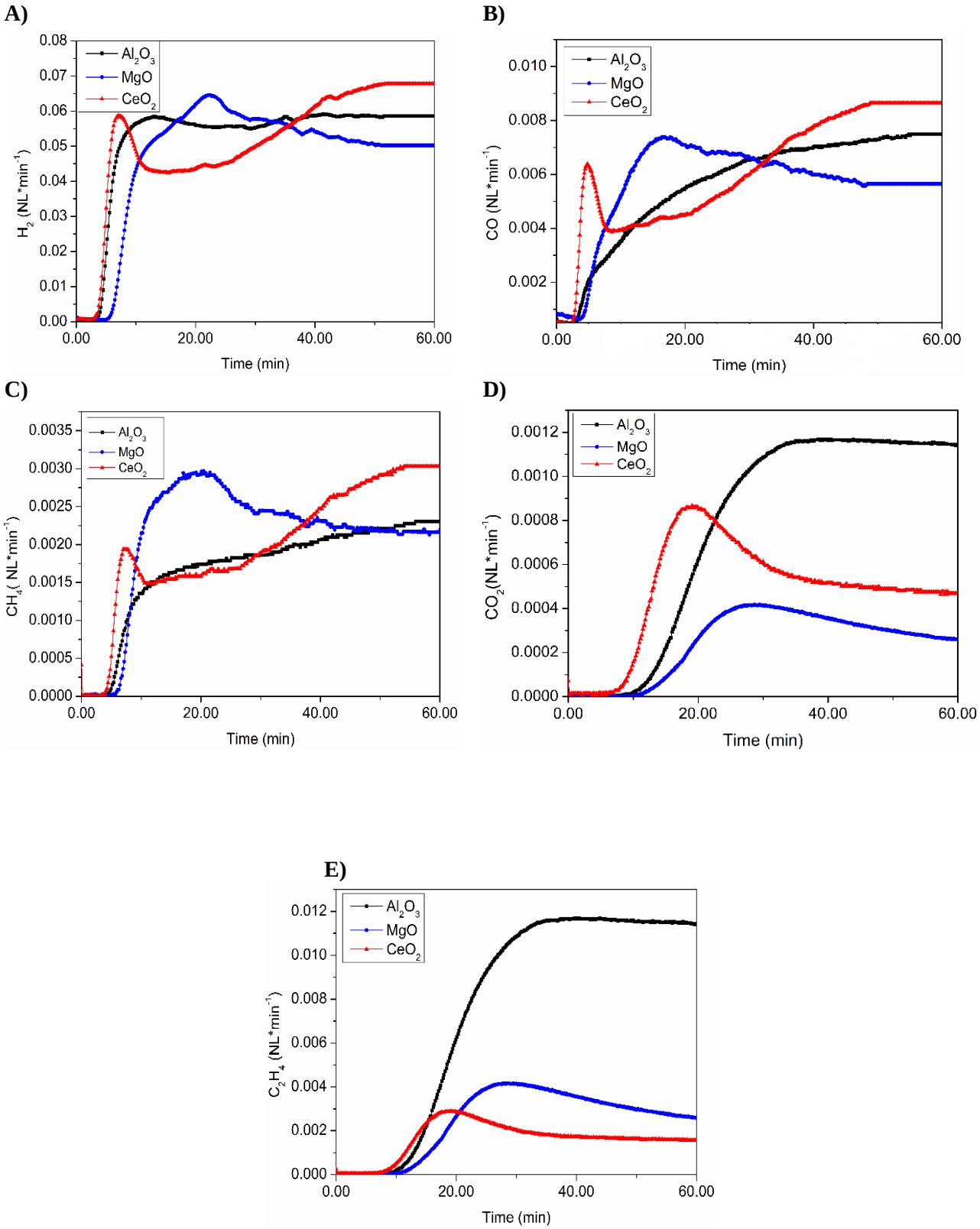

***Figure 6.1**: Volumetric flowrates of the main gaseous products resulted from ethanol decomposition on Al_2O_3, CeO_2 and MgO (675 °C, 1 bar, reaction time 1 h).*

Table 6-1: *Molar amount of the main ethanol decomposition products with Al_2O_3, MgO and CeO_2(675°C,1 bar, reaction time 1 h)*

	Al_2O_3 (mmol)	**MgO (mmol)**	**CeO_2 (mmol)**
Gas phase			
H_2	90.10 ± 2.00	132.00± 4.00	130.00± 4.00
CO	9.00± 1.00	15.00± 1.00	12.00± 1.00
CO_2	1.20± 0.10	0.40± 0.01	0.90± 0.08
CH_4	3.00± 0.08	5.00± 0.10	4.00± 0.08
C_2H_4	12.00± 1.00	8.00± 1.50	5.00± 1.50
Liquid phase			
H_2O	75.00± 3.00	47.00± 2.00	50.00± 3.00
Solid phase			
Coke	120 ± 10.00	100± 12.00	90± 9.00

According to the results collected in Figure 6.1 and Table 6-1, a complete ethanol conversion is obtained in all the tests; the liquid phase, condensed at the reactor exit is, in fact, composed only by water. The gaseous stream is mainly constituted by H_2 and CO, however, albeit in different proportions, the solid carbon is always formed, confirming the main drawback of ethanol utilization in the process.

Among the promoters tested, the highest amount of carbon is obtained in the presence of Al_2O_3 suggesting that the use of an acidic oxides in the process promotes the cracking reactions of the light hydrocarbons enhancing coke formation[157]. Al_2O_3, is also a catalyst for alcohols dehydration reaction promoting, in the case of ethanol, the production of C_2H_4 and water[158]. The effect of the catalytic activity offered by Al_2O_3 in ethanol dehydration reaction is clearly visible in the plot of Figure 6.1 E and 6.1 D. The increased presence of water, related to the catalytic activity of Al_2O_3 on dehydration reaction, promotes the direct water gas shift reaction, leading to higher CO_2 concentration in the gas phase (Figure 6.1 D).

MgO and CeO_2 act similarly in the ethanol cracking reactions. Ethanol starts to decompose mainly into H_2, CO and CH_4 accompanied by traces of C_2H_4. A fraction of the methane and ethylene participates to cracking reaction producing coke. A peculiar trend for H_2, CO and CH_4 is registered when CeO_2 is used. The curves of these three gaseous compounds present a clear peak in the first 15 minutes (Figure 5.1 A-C) suggesting an interaction between CeO_2 and them. The explanation to this behaviour can be found in numerous literature works, which demonstrated a catalytic activity of CeO_2 in oxidation/partial oxidation of hydrocarbon[159] [160]. The lattice oxygens of CeO_2 act as local oxygen source for hydrocarbon combustion reactions and H_2, CO and CH_4 are partially burnt (Figure 5.1 A-C) by lattice oxygen, till CeO_2 is reduced to CeO_{2-x} [161] . When the lattice oxygens of CeO_2 are not available anymore the concentration of H_2, CO and CH_4 starts to increase (Figure 5.1 A-C).

Optimal amount of ethanol in the reduction step: effect of MgO, CeO_2 and Al_2O_3 addition

To make possible the use of ethanol as reducing agent for pure H_2 production, the control of the reduction degree is fundamental. For each Fe based sample the amount of ethanol was tuned in order to find the optimal value which corresponds to the maximization of the yield of H_2 pure. These tests are needed to understand the effect of the promoter addition on the Fe_2O_3 redox activity and consist into 1 redox cycle where different amount of ethanol are fed (4.56, 3.42, 2.28 and 1.14 mmol, which correspond to an ethanol feeding time from 4 min to 1 min). Considering that the particle synthesis method is a key factor for their activity, tests with pure Fe_2O_3 synthetized by the same method are also performed.

Figure 6.2 A and figure 562 B report the amount of H_2 and CO produced in the first oxidation step as a function of the ethanol fed in the reduction.

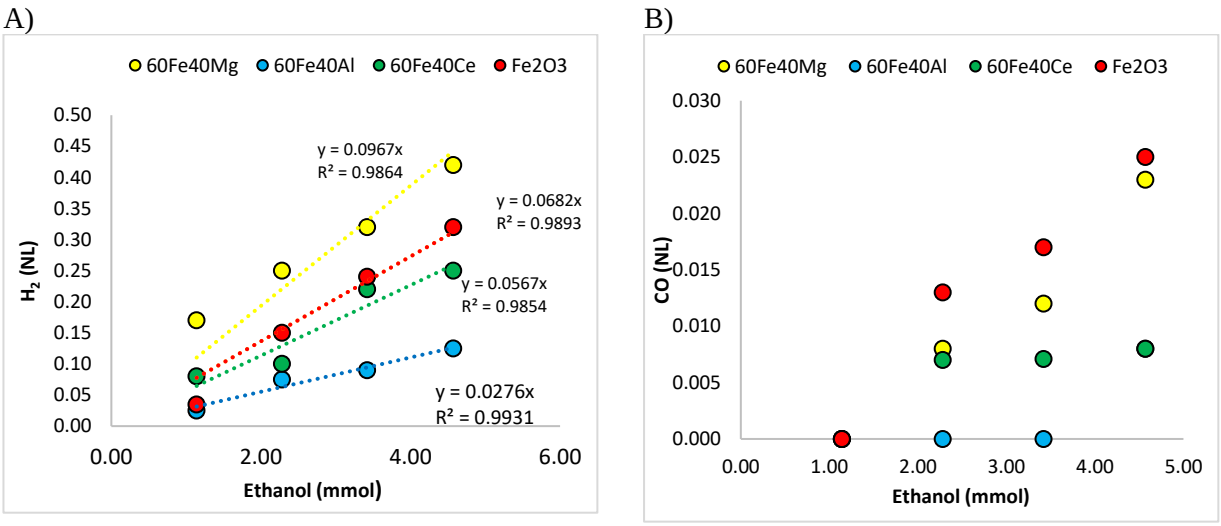

Figure 6.2: A) *H_2 produced in the first oxidation step as a function of ethanol fed in reduction* ***B)*** *CO produced in the first oxidation as a function of ethanol fed in reduction* .

The results collected in figure 6.2 A and figure 6.2 B highlight the existing relationship between the particle reduction degree and the hydrogen purity. As already demonstrated in Chapter 5, decreasing the amount of ethanol fed leads to lower reduction degree of iron oxide and therefore to lower H_2 yield in oxidation (Figure 6.2 A). The plot of CO concentrations (Figure 6.2 B) shows the same trend. CO decreases when the amount of ethanol fed is lowered till the optimal amount of ethanol is reached (CO < 10 ppm).

Figure 6.2 A shows a linear dependency between H_2 yield and ethanol fed in reduction for all the samples. In the experiments conducted with pure Fe_2O_3, a significant variation of H_2 as a function of the ethanol fed is registered. The promoter addition mitigates this effect, the slope of the curve is in fact

lower (0.0955 for Fe_2O_3, 0.06 for CeO_2 and MgO, 0.039 for Al_2O_3) and thus the H_2 yields seem to be less dependent on the amount of ethanol fed. This result suggests that the presence of a promoter does not only affect the thermal stability of iron oxides but also their redox activity and the accessibility of the reactive iron sites. The influence of promoter on the sample morphology is already discussed in chapter 3 and will be resume at the end of this chapter.

For each amount of ethanol tested the highest amount of H_2 is always obtained with the sample 60 wt% Fe_2O_3-40 wt% MgO while the lowest with 60 wt% Fe_2O_3 -40 wt% Al_2O_3. The samples 60 wt% Fe_2O_3-40 wt% CeO_2 and pure Fe_2O_3 show an intermediate behaviour.

Some additional information can be obtained looking at Figure 5.2 B which reports the amount of CO detected in oxidation as a function of ethanol fed. Except for the sample 60 wt% Fe_2O_3-40 wt% CeO_2, CO profile always presents a linear variation with the amount of ethanol fed, confirming the relationship between reduction degree and carbon deposition. The plateau value registered in the presence of CeO_2 for high amount of ethanol, can be related to the excellent mobility of the lattice oxygen of this material (Figure 6.2 B). Specifically, CeO_2 is able to reduce the carbon deposition even when all the iron oxides are reduced, consuming the carbon deposited thanks to its high lattice oxygen mobility. This result confirms the active participation of CeO_2 during the redox cycles, relieved also in the blank tests. The lowest production of CO at high amount of ethanol fed was registered for the sample with Al_2O_3.

The optimal amount of ethanol fed is equal to 1.14 mol (0.83 mmol/g $_{Fe2O3}$) for all the sample tested except for 60 wt% Fe_2O_3 -40 wt% Al_2O_3 for which a pure H_2 stream is already obtained with 3.42 mmol of ethanol fed (2.85 mmol/g_{Fe2O3}). Table 6-2 reports the process efficiency calculated according to equation 3.4 (Chapter 3) and the ratio H_2 produced in the first oxidation step and the optimal amount of ethanol fed in reduction.

Table 6-2 Efficiency of the process and weight amount of pure H_2 produced on optimal amount of ethanol fed in reduction.

	E_p (%)	**H_2(NL)/ EtOH(g)**
Fe_2O_3	5.57	0.475
60 wt% Fe_2O_3-40 wt% MgO	37.87	3.422
60 wt% Fe_2O_3-40 wt% Al_2O_3	15.60	0.444
60 wt% Fe_2O_3-40 wt% CeO_2	13.37	1.141

As reported in table 6-2, the sample 60 wt% Fe_2O_3- 40 wt % MgO shows the best performance. The use of MgO improves the production of pure H_2 increasing the process efficiency (37.87%) and at the same time consuming the lowest amount of ethanol (H_2/EtOH=3.42).

Stability tests: effect of promoter addition

After the determination of the optimal amount of ethanol fed in the reduction step, stability tests are conducted to evaluate the cyclability of the synthetized Fe-based particles. The stability tests consist in 10 consecutive redox cycles feeding in reduction the optimal amount of ethanol previously determined. During the oxidations step, water is fed until complete oxidation is reached.

The amount of H_2 produced in each oxidation step for all the Fe-based particles is reported in figure 2.1. For comparison purpose, the results obtained with pure Fe_2O_3 are also reported.

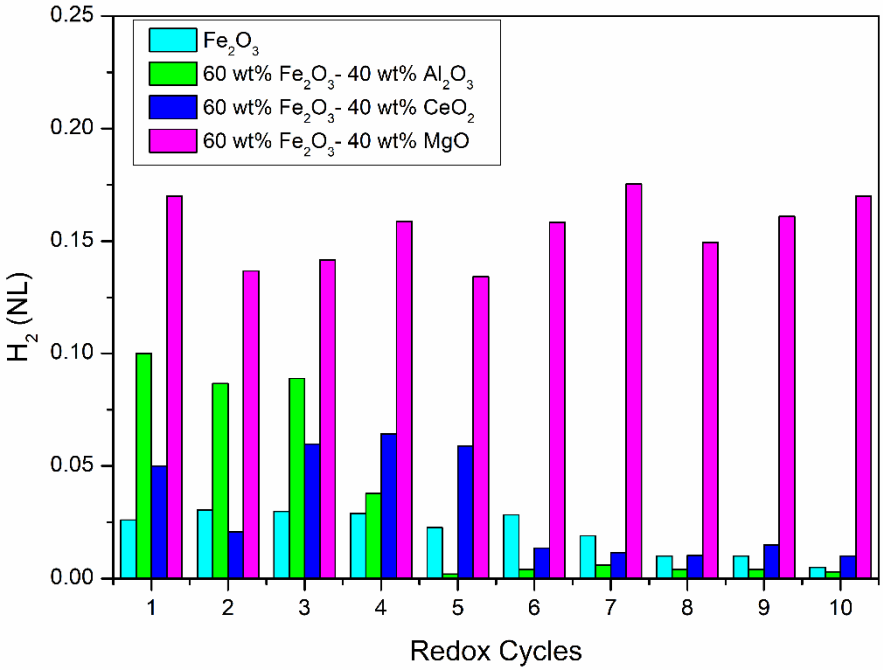

***Figure 6.3**: Amount of H_2 produced by each sample for 10 consecutive redox cycles.*

Looking at the results collected in figure 2.1, where the results obtained with promoters are compared with those of pure Fe_2O_3, only using 60 wt% Fe_2O_3 40 wt% MgO a stable H_2 production is registered for all the cycles. MgO addition improves not only iron cyclability but also hydrogen yields confirming its positive effect on the iron oxides reduction degree also at repeated redox cycles.

With the sample 60 wt% Fe_2O_3- 40 wt% Al_2O_3 the amount of H_2 produced significantly decreases after few redox cycles (3 cycles). Initially, a consistent amount of H_2 was produced (0.10-0.085 NL), but this value dropped to very low amounts for higher number of cycles. A similar behaviour is also registered for the sample 60 wt% Fe_2O_3-40 wt% CeO_2. With the addition of CeO_2 no positive effects in terms of particles stability were obtained, in fact, the sample can be consider completely deactivated at the 6th cycle. However, for all the sample studied, a pure H_2 stream was obtained in each cycle confirming that the tuning of the amount of ethanol fed in reduction is a fundamental step in the optimization of the whole process, significantly affecting the H_2 purity also for high number of redox cycles. The worst

performances are obtained using pure Fe_2O_3 for which a very low amount of H_2 is produced in the first redox cycle and, as expected, a drop in H_2 production is observed after consecutive cycles.
In order to evaluate the effective amount of iron which participates to the redox reactions, the efficiency of the process is calculated for the sample which exhibits the better performance (60 wt% Fe_2O_3 -40 wt% MgO). Table 2.0 reports the efficiency of the process (E%) calculated for each cycle

***Table 6-3**: efficiency of the process for each cycles using 60 wt% Fe_2O_3 - 40 wt% MgO.*

Redox cycles	E (%)
1	37.87
2	30.51
3	31.57
4	35.37
5	29.90
6	35.26
7	39.06
8	33.28
9	35.89
10	37.87

The efficiency values for the sample 60 wt% Fe_2O_3- 40 wt% MgO confirms that decreasing the reduction time and therefore the amount of ethanol fed imply the reduction of only a fraction of the loaded Fe, leading to a lower process efficiency value (≈35%). However, considering that the main advantage of this technology is the direct production of pure H_2 it can be convenient to reach this target even at the expense of the hydrogen yield if a stable hydrogen production over a high number of cycles is reached.

6.4 Characterization of the Fe-based particles after stability tests

XRD

The crystal phase of each Fe-Based particles and of pure Fe_2O_3 at different step of the process (fresh sample, after 1° reduction and at the end of the stability test) are reported in figure 6.5 A-D. The comparison with the XRD results if each fresh samples, already reported in Chapter 3, is added to highlight how the chemical interaction between the active metal and the structural promoter at change at different step of the process.

The fresh sample Fe_2O_3-MgO shown a chemical interaction between the Fe and Mg already after synthesis. Specifically, after calcination in air at 900°C, magnesium oxide and iron oxide form a spinel structure, magnesium ferrite ($MgFe_2O_4$) (figure 6.4 B). $MgFe_2O_4$ is one of the most important ferrites

which find a wide number of applications in heterogeneous catalysis, in the sensor sector and in magnetic technologies [162]. These interactions modify the redox system of the Fe_2O_3-MgO material. After reduction, in fact, iron is reduced in two different structures, part of the iron is present as magnetite and the other amount form a mixed oxides named magnesiowustite $(Mg_{0.6}Fe_{0.4})O$ with oxidation state equal to +2 (figure 6.4 B). Comparing the iron oxidation state after the first reduction step of the Fe-based particles, only for MgO metallic iron is not detected. This is not related to the limited duration of the reduction step but to the interaction between iron and magnesium. The MgO lattice, in fact, stabilize the oxidation state +2 of iron in the solid solution preventing the total reduction of iron oxide to Fe^0 [163].

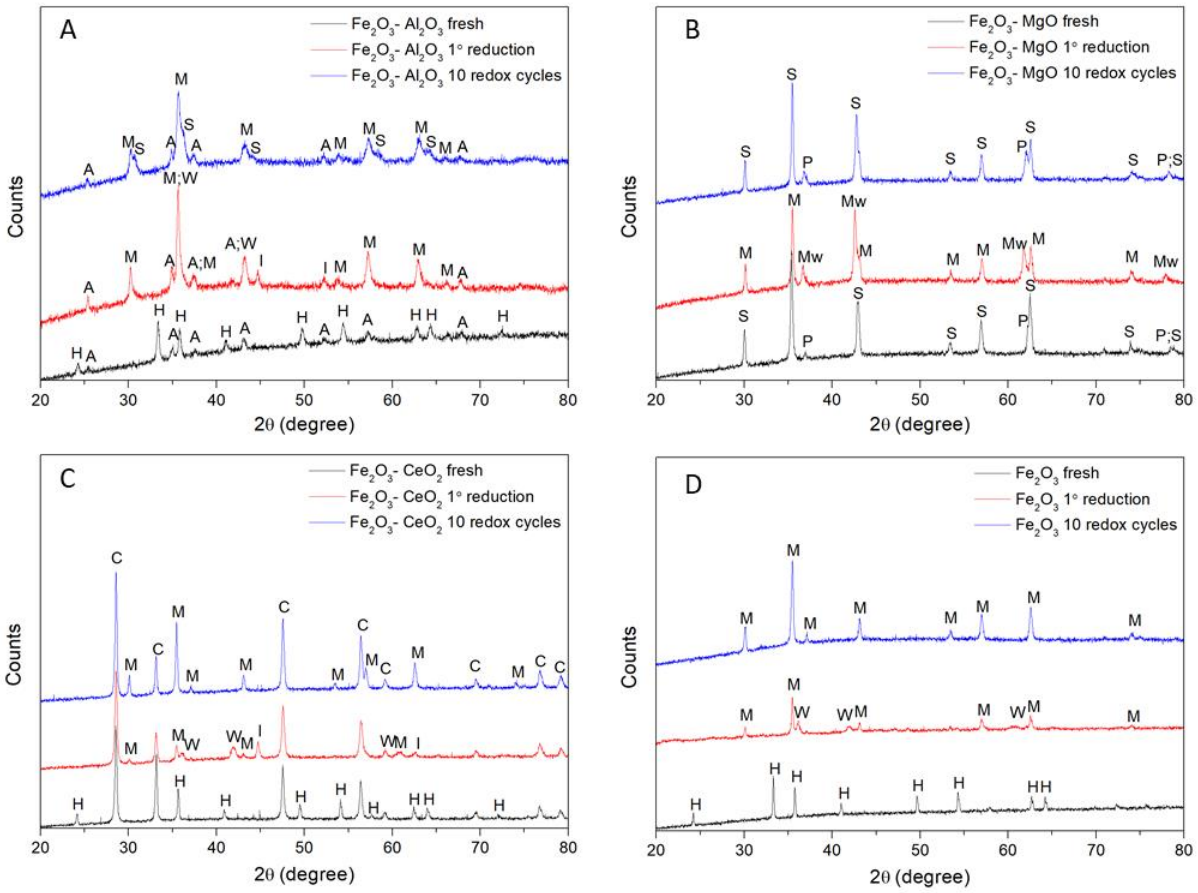

Figure 6.4: *XRD pattern of Fe-based particles (fresh, after the 1th reduction and after the stability test). H= Fe_2O_3; M= Fe_3O_4; W =FeO; I=Fe; A= Al_2O_3; P= MgO; C= CeO_2; Mw= $(Mg_{0.6}Fe_{0.4})O$; S= Spinel ($FeAl_2O_4$ or $MgFe_2O_4$).*

Assuming that the stability of the powders in steam iron process is strongly dependent on the reduction degree of iron oxides, the lag effect of MgO on iron oxides reduction is responsible to the better activity of this sample.

For 60 wt% Fe_2O_3-40 wt% Al_2O_3 the formation of a spinel iron aluminate ($FeAl_2O_4$) is detected only after the stability tests (figure 5.4 A) . Considering the significant activity loss registered for this sample,

the formation of $FeAl_2O_4$ can be responsible of the deactivation. However, any interaction between iron and aluminium oxides is detected after calcination or after the first reduction, suggesting that the formation of $FeAl_2O_4$ occurs during oxidation with steam water. The formation of $FeAl_2O_4$ can make the material inactive in the subsequent cycles. Tsvigunov et al.[164] stated that the formation of $FeAl_2O_4$ occurs during the oxidation step and it can convert back to iron oxide and Al_2O_3 only after CO reduction in a temperature range of 800-1100°C. Due to the low temperature adopted in this study (675°C) and to the strict control of the reduction time to avoid carbon deposition, $FeAl_2O_4$ is not decomposed due the thermodynamic and kinetics limitations, leading to a complete deactivation of the sample.
Furthermore, the formation of Fe phase at the first reduction step registered in the samples with Al_2O_3 and CeO_2, can be responsible of their deactivation (figure 5.4 A and figure 5.4 C, respectively). As already explained in the previous section Fe can catalyse cracking reaction improving coke formation, that considered the pure H2 stream obtained, remains on the particles surface cycle after cycle. The carbon deposited can block the particle active sites making them unactive at repeated cycles.
Only in the sample 60 wt% Fe_2O_3- 40 wt% CeO_2 no interaction is detected between the two oxides at any step of the process.

Elemental analysis for determination of carbon deposition after the stability test

In order to better understand if particle deactivation is related to the interaction between Fe and promoters or to the deposition of unreacted carbon during the reduction step, elemental analyses of the Fe-based particles after the stability tests are performed. Table 6-4 reports the results obtained for each sample after the stability test.

***Table 6-4**: Amount of carbon for each sample after the stability tests.*

	Carbon (wt%)
Fe_2O_3	0.00
60 wt% Fe_2O_3-40 wt% MgO	0.00
60 wt% Fe_2O_3-40 wt% Al_2O_3	0.90
60 wt% Fe_2O3-40 wt% CeO2	0.40

At the operating conditions adopted, only for Fe_2O_3-Al_2O_3 and Fe_2O_3-CeO_2 carbon was measured after the stability tests. Looking at XRD analysis after the first reduction (figure 6.4 D), the formation of unreacted solid carbon occurs only for the two samples in which a fraction of metallic iron is obtained. The formed carbon does not react with water in oxidation step, remaining on the particle surface and contributing to the deactivation blocking the active sites. The control of the amount of ethanol fed totally avoid the carbon deposition for the samples 60 wt% Fe_2O_3-40 wt% MgO and pure Fe_2O_3.

These results confirm that also carbon deposition, together with thermal and mechanical resistance, is a key factor for particle stability. In fact, the sample Fe_2O_3-MgO presents the highest stability in the tests due to the complete absence of carbon deposition and to the high thermal stability of MgO. The highest amount of carbon on the particle's surface is registered for 60 wt% Fe_2O_3-40 wt% Al_2O_3 due to the catalytic activity of Al_2O_3 towards cracking reaction.

BET

The activity of the redox material in the process is also strongly related to their active surface area. In order to evaluated if structural modifications of the Fe-based particles during repeated cycles take place, BET analyses before and after the stability test were performed. Table 6-5 summarizes the results obtained.

***Table 6-5**: BET surface area of each sample before and after the stability test*

	Fresh ($m^2 \cdot g^{-1}$)	After stability test ($m^2 \cdot g^{-1}$)
Fe_2O_3	0.7411	0.5601
60 wt% Fe_2O_3-40 wt% MgO	9.7593	8.4675
60 wt% Fe_2O_3-40 wt% Al_2O_3	9.0084	1.2346
60 wt% Fe_2O3-40 wt% CeO_2	2.7886	2.2936

As reported in Table 5-5, Fe_2O_3 exhibited a small specific surface area (0.74 $m^2 \cdot g^{-1}$). The low H_2 yields registered during the stability tests using Fe_2O_3 as redox material are therefore related to the important limitation of the gas diffusion in the bulk of the particle. With the addition of the promoters a positive effect in terms of reactive surface area is always obtained.

Among the promoters tested, fresh 60 wt% Fe_2O_3- 40 wt% MgO exhibits the highest surface area equal to 9.76 $m^2 \cdot g^{-1}$ followed by 60 wt% Fe_2O_3-40 wt% Al_2O_3 with 9.00 $m^2 \cdot g^{-1}$. However, the surface area of the sample with Al_2O_3 significantly decrease after 10 redox cycles (1.23 $m^2 \cdot g^{-1}$) due to the high carbon deposition. Among the promoters studied, the fresh 60 wt% Fe_2O_3-40 wt% CeO_2 exhibits the lowest surface area (2.7886 $m^2 \cdot g^{-1}$). Several studies report the negative effect of increasing calcination temperature on CeO_2 surface area. In the study conducted by Amadine et al.[165] a significant decrease of surface are from 156 $m^2 \cdot g^{-1}$ to 8 $m^2 \cdot g^{-1}$ is registered when the calcination temperature increase form 500 °C to 800 °C. The thermal stability of CeO_2 is lower than MgO and Al_2O_3. The low H_2 yield obtained with the utilization of this sample can be related also to its low active surface area. However, the reduction of the surface area after the test is almost insignificant suggesting that the sample deactivation is not related to agglomeration phenomena. For this sample it seems that the deactivation is to be ascribed to the formation of carbon which partially blocks the active sites.

The surface area of 60 wt% Fe_2O_3 -40 wt% MgO is the highest and only a slight reduction after the test is measured (15 % of reduction). The decrease of the surface area is related to the interactions between Fe_2O_3 and MgO in both reduction and oxidation phase.

SEM

SEM analysis was also performed to compare the Fe-based particles morphology before and after the stability tests.

From the comparison of the fresh samples, the presence of the promoters leads to an improve of the Fe_2O_3 porosity as also confirmed by the results of the BET analyses. Looking at figure 6.5 B) Fe_2O_3 particles after the stability tests present incipient softening phenomena, confirming the low thermal stability of pure Fe_2O_3 and the importance of the presence of a structural promoter to make possible its utilization in the steam iron process.

A) Fe_2O_3 fresh

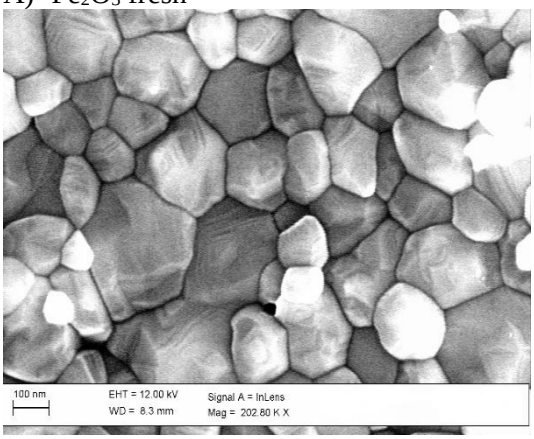

B) Fe_2O_3 after 10 redox cycles

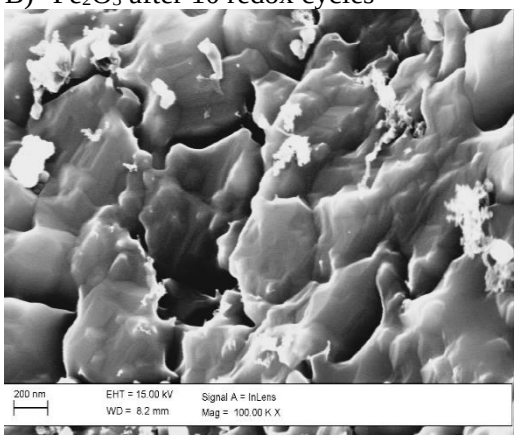

C) 60 wt % Fe_2O_3- 40 wt% MgO fresh

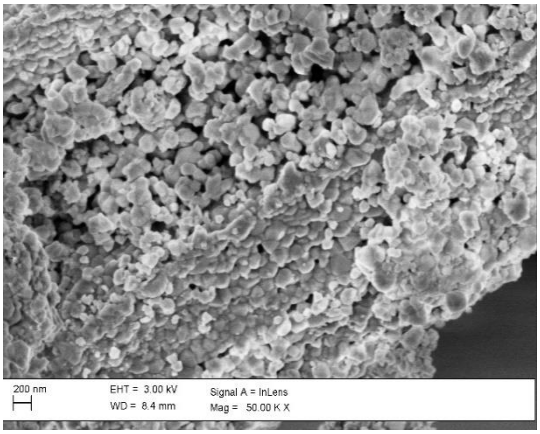

C) 60 wt % Fe_2O_3- 40 wt% MgO after 10 redox cycles

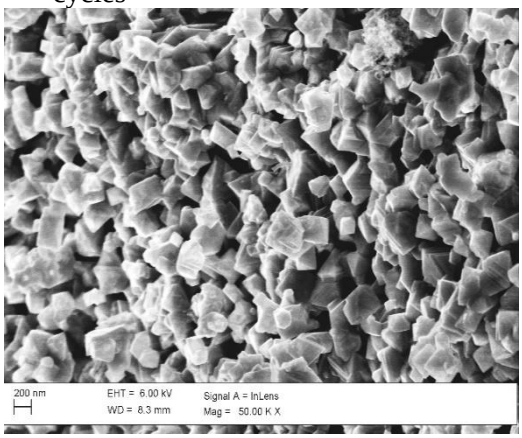

E) 60 wt % Fe_2O_3- 40 wt% CeO_2 fresh

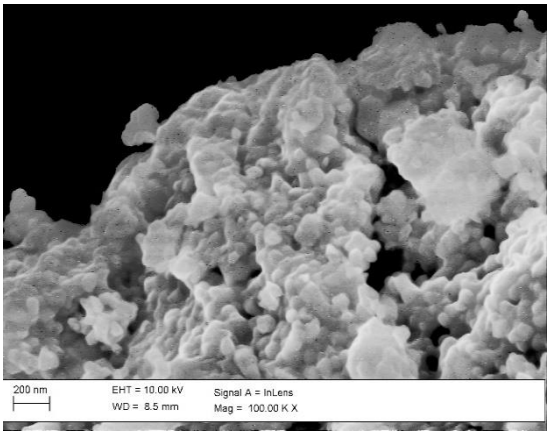

F) 60 wt % Fe_2O_3- 40 wt% CeO_2 after 10 redox cycles

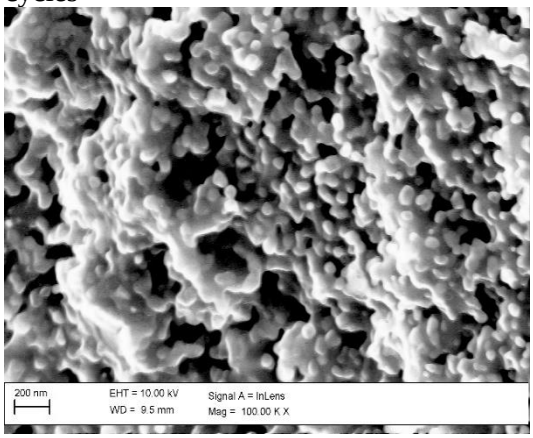

G) 60 wt % Fe_2O_3- 40 wt% Al_2O_3 fresh

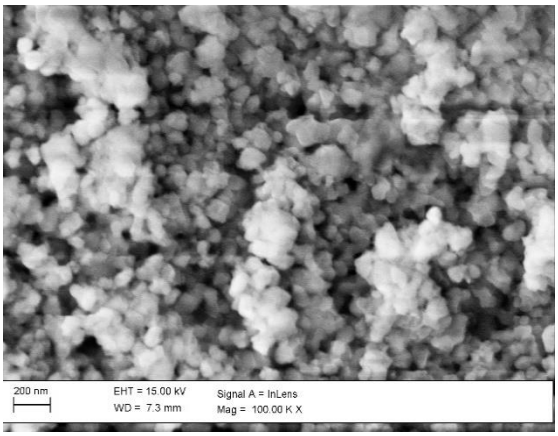

H) 60 wt % Fe_2O_3- 40 wt% Al_2O_3 after 10 redox cycles

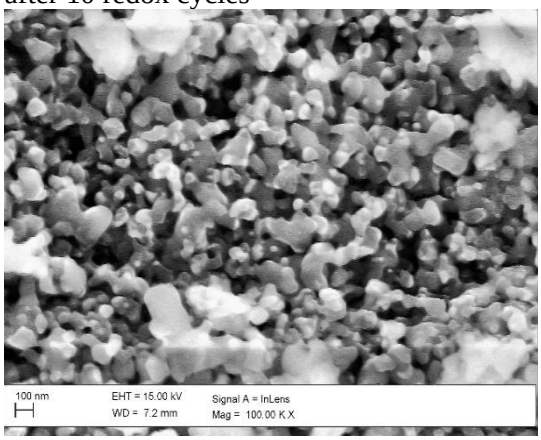

Figure 6.5: *SEM images of the Fe-based particles before and after the stability tests.*

Looking at the samples with Al_2O_3 and MgO addition before and after the stability tests (figure 6.5 G-H and C-D, respectively) the high thermal stability of these materials is confirmed. After stability test, in fact, no significant differences are detected in terms of sample porosity. Therefore, the significant decreases of the surface area registered in BET analyses for the sample with the presence of Al_2O_3 (Table 5-5) is related to the formation of carbon resistant to oxidation with water that blocking the active sites led to a lower active surface area. For the sample with MgO addition, although the dimension of particles suffered a slight increase in size, no smoother surfaces are relieved, and the crystallite of the sample are clear visible also after the stability test. This result confirms the positive effect of MgO addition on the activity and stability of iron oxides in the steam iron process.

According to BET analysis, the surface area of 60 wt% Fe_2O_3- 40 wt% CeO_2 does not present a significant decrease. However, looking at figure 5.5 F which reports the sample's images after the stability test, the particles seem to be covered by a carbon layer confirming the results of the carbon deposition and a coalescence of the grain is visible.

6.5 Conclusion

The results obtained in this Chapter demonstrates that, Al_2O_3, CeO_2 and MgO not only improve the thermal stability of iron oxides, but they actively participate in the process, modifying the particles reactivity. Specifically, the studied promoters influence the ethanol decomposition reactions and interact with iron forming spinel structures affecting the iron oxides redox properties. The control of the reduction degree by means of the ethanol feeding time was successfully applied to avoid the presence of CO in the oxidation step. Among the Fe-based particles tested, 60 wt% Fe_2O_3- 40 wt% MgO is the most favourable one, giving the highest pure H_2 yields and consuming the lowest amount of ethanol in reduction ($H_2(NL)/\ EtOH(g) = 3.422$). The thermal stability of each sample is evaluated for 10 consecutive redox cycles, and only the samples with MgO shows a constant activity, leading to a stable H_2 yields at 10 redox cycles (H2= 0.15 NL and E= 35 %). The presence of MgO as promoter of iron oxides makes the system stable also using bioethanol as direct reductants and thus mature for a scale-up.

7. Al_2O_3 as structural promoter of Fe into 2 and 3 steps chemical looping hydrogen process

7.1 Introduction

Al_2O_3 is one of the most studied material in the field of heterogeneous catalysis, widely used as a catalytic support in many chemical reactions [166]. Its utilization in chemical looping processes still requires a deep investigation because of its active role in the redox mechanism when iron is used as OCs [167]. In fact, as demonstrated in the chapter 6, Al_2O_3 interacts with iron during the redox cycles forming a spinel structure, named hercynite ($FeAl_2O_4$), which totally changes the OCs reactivity[168]. Furthermore, due to its acidic nature Al_2O_3 catalyse cracking reactions, when carbon-based reducing agent are used, promoting the carbon formation during the reduction step [169] [170].

In this Chapter the production of pure and green H_2 by chemical looping technology using bioethanol as renewable fuel and Fe_2O_3-Al_2O_3 particles as OC is deeply investigated. The interaction between Fe and Al is studied in the 2 steps CLH configuration at different Fe_2O_3/Al_2O_3 ratios to better understand the effect of Al_2O_3 addition on particle's performance. For this purpose, two samples with 40 wt% (60Fe40Al) and 2 wt% (98Fe2Al) of Al_2O_3 added were synthesized. The samples were tested at two temperatures (675°C-750°C) for 10 consecutive redox cycles. The experiments at higher temperature are performed to enhance the hydrogen yields by favouring the iron oxides reduction.

The increase of temperature has opposite effects on the CLH system: it enhances the hydrogen yield and increases the rate of carbon formation during reduction. At higher temperatures, in fact, the ethanol conversion into solids carbon is promoted both from a thermodynamic and kinetic point of view, due to the endothermic nature of cracking reaction and due to the catalytic activity offered by iron phase, respectively. Since the deposition of carbon, as already demonstrated, is one of the main issues when carbonaceous reductants are used, it is fundamental to study the decomposition of ethanol at the higher temperature. Therefore, the influence of temperature on ethanol cracking is first studied on an inert SiO_2 fixed bed (750°C).

To conclude, the sample 60Fe40Al is also tested into a 3 steps CLH (reduction-steam oxidation-air oxidation) with the aim to avoid the sample deactivation at consecutive cycles caused by the spinel formation.

7.2 Experimental procedures

The particles were tested in a fixed bed reactor at reaction temperatures of 675°C and 750°C maintaining the pressure constant at 1 bar. The fixed bed was constituted by 1 gram of Fe-based particles. The bench scale plant is described in detail the Chapter 3.
In the 3 steps CLH experiments, air was also fed to the reactor at the end of each steam oxidation with a constant flowrate of 500 mL/min.

7.3 OCs characterization results

XRD analysis

To have a better comprehension of the experimental data obtained, a study of the physical and chemical properties of the sample before and after the rection is needed. XRD analyses were performed on the samples 60Fe40Al and 98Fe2Al before and after the stability test (10 consecutive redox cycles) at 675°C and 750°C in the 2 step CLH configuration. The diffractograms are reported in Figure 7.1. The pattern of the sample 98Fe2Al after the stability test at 750°C overlaps with that at 675°C and therefore it is not reported in the Figure.

The pattern of the fresh sample 98Fe2Al shows only the peaks related to Fe_2O_3 suggesting that the amount of free crystalline alumina in the sample is lower than the detection limit of the XRD technique used [171][172]. The same results are obtained for the sample 98Fe2Al after the stability tests in all the range of temperature studied, no signals for Al_2O_3 are detected and iron is present only in the crystal phase of magnetite (Fe_3O_4). Furthermore, no $FeAl_2O_4$ phase is detected in any process step: if a chemical interaction between Fe and Al occurs, it regards only a small amount of the sample and it is lower than the detection limit of XRD analysis.

A particular behaviour is detected for the sample 60Fe40Al. Unlike 98Fe2Al, the XRD pattern of the fresh 60Fe40Al shows the two separated oxides (Fe_2O_3 and Al_2O_3), the spinel is not presence after the sample synthesis. Looking at the 60Fe40Al pattern after stability tests, the crystal phases detected change with the reaction temperature suggesting that the formation of spinel is affect by the reaction temperature. At 675°C the crystal phases are magnetite (Fe_3O_4), hercynite ($FeAl_2O_4$) and corundum (Al_2O_3) while by increasing the reaction temperature until 750°C, the signal of free Al_2O_3 at the end of the test disappears, and only the peaks for $FeAl_2O_4$ are detected. These results confirm that the spinel formation occurs during the redox cycles and that higher temperature favoured its formation.

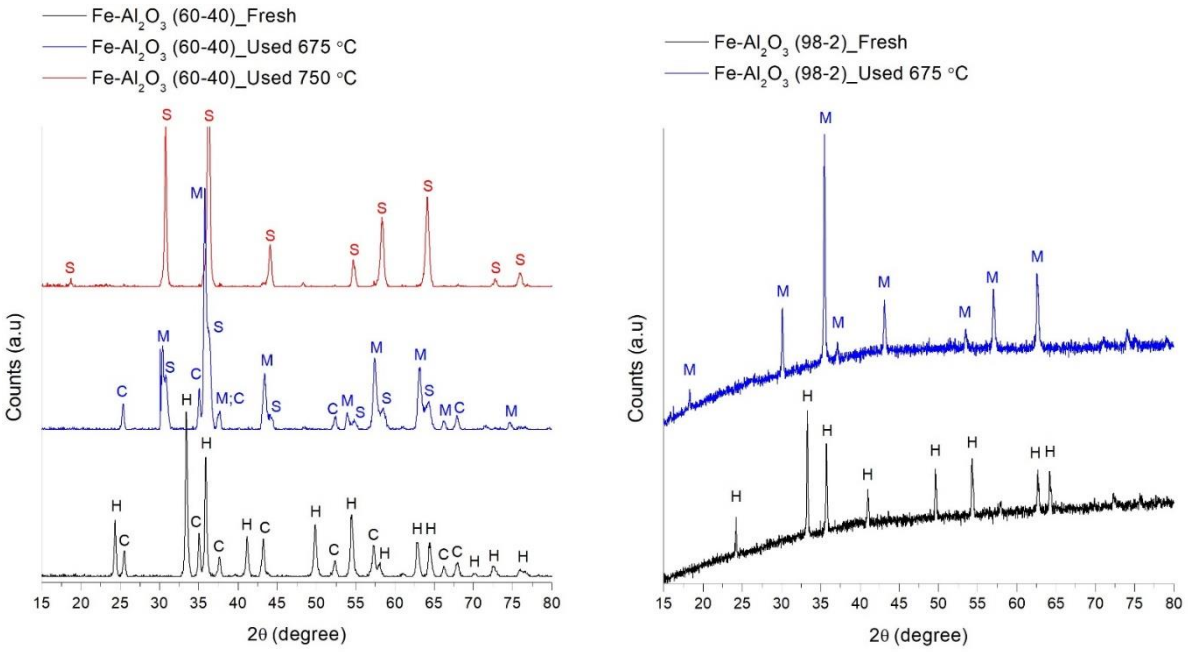

***Figure 7.1**: XRD patterns of the sample 60Fe40Al (left) and 98Fe2Al (right) before and after the stability tests at 675°C and 750°C. (H: Fe_2O_3, M: Fe_3O_4, C: Al_2O_3, S: $FeAl_2O_4$)*

BET analysis

The sample surface area is a key parameter of the process since it directly affects the sample reactivity. To evaluate the structural modification during the consecutive redox cycles and the influence of Al_2O_3 addition on the surface area of the Fe_2O_3, BET analyses are conducted on the samples before and after the stability tests at all the tested temperatures. The BET surface area values before and after tests are summarized in Table 7-1. Looking at the BET value of the fresh samples, it is evident that there is a strong relation between amount of Al_2O_3 added and BET, increasing the amount of Al_2O_3 the BET raises from 1.5 m^2/g to 9 m^2/g.

***Table 7-1**: BET analysis of the fresh samples before and after the stability tests as a function of temperature*

BET analysis (m^2/g)	***Fresh sample***	***675°C***	***750°C***
98Fe2Al			
2 steps	1.2	1.1	1.0
60Fe40Al			
2 steps	9.0	1.3	1.2
3 steps	9.0	6.2	6.2

After the stability tests in the 2 steps CLH, the surface area of the sample 60Fe40Al decreases of 86.7% with respect to its original value (from 9 m^2/g to 1.3 m^2/g at 675°C). The effect of temperature on the decrease of surface area is not substantial, only a slight negative trend is observed going from 1.3 m^2/g at 675 °C to 1.2 m^2/g at 750°C.

However, for the same sample the drop in BET surface area in the 3 step CLH is only of 33.0% varying from 9.0 m^2/g to 6.2 m^2/g after the test at 675°C and it remains almost constant with reaction temperature. This different behaviour can be related to the different chemical composition of the sample at the end of the CLH tests in the 2 and 3 steps configuration. In the 2 steps CLH the sample is composed by a mixture of $FeAl_2O_4/Fe_3O_4$ in different proportion according to the reaction temperature. At the end of stability test in the 3 step CLH the $FeAl_2O_4$ is converted into Fe_2O_3 and Al_2O_3 by the addition of the air oxidation step[167].

On the contrary, the BET values of the sample 98Fe2Al at the end of the stability tests are always close to the fresh one (fresh sample 1.2 m^2/g, 1.0 m^2/g at 750°C).

7.4 Experimental results

Influence of temperature on ethanol cracking products

The results of the ethanol decomposition on inert material are reported in Table 7-2 where the molar fraction of the products (carrier free basis) as a function of temperature (675°C,750°C) are shown.

Table 7-2:Thermal ethanol decomposition products and carrier free molar concentration at 675°C and 750°C.

Temperature	H_2	CO	CH_4	Carbon
675°C	58.4%	18.4%	7.0%	17.1%
750°C	61.5%	17.2%	3.2%	19.1%

As reported in Table 7-2 the molar fraction of the products changes with reaction temperature. At the highest temperature tested in this study (750°C), H_2 molar fraction is 6% higher than the value at 675°C while methane decreases of 55% whit respect the value registered at 675°C. The production of solid carbon formation is also favoured at higher temperature (from 17.1% to 19.1%).

The decrease of methane concentration registered at 750°C is due to the occurring of methane cracking reaction, favoured at high temperature, which leads to higher H_2 and carbon yields. The concentration of CO remains constant in all the tests, confirming its non-participation in secondary reactions.

The increased concentrations of H_2 and carbon at 750°C confer a higher reducing power to the produced stream. However, the iron reduction by carbon still owns slow kinetics over the range of temperatures

studied (675°C-750°C) [173] [174] therefore its formation must be carefully monitored to avoid the production of H_2 contaminate by CO.

Influence of temperature and amount of Al_2O_3 added to Fe on the purity of H_2

The optimal amount of ethanol is determined performing 1 redox cycle experiments at 675°C and 750°C, by feeding different amounts of ethanol in reduction (3.42-5.71 mmol of EtOH) and by fully oxidizing the sample with steam monitoring the H_2 purity.

The comparison of the process efficiency obtained with the samples 60Fe40Al and 98Fe2Al at two different redox temperatures (675°C and 750°C) is reported in Figure 7.2. The maximum CO concentration measured in the first oxidation step is also reported in the graph.

A) 675°C B) 750°C

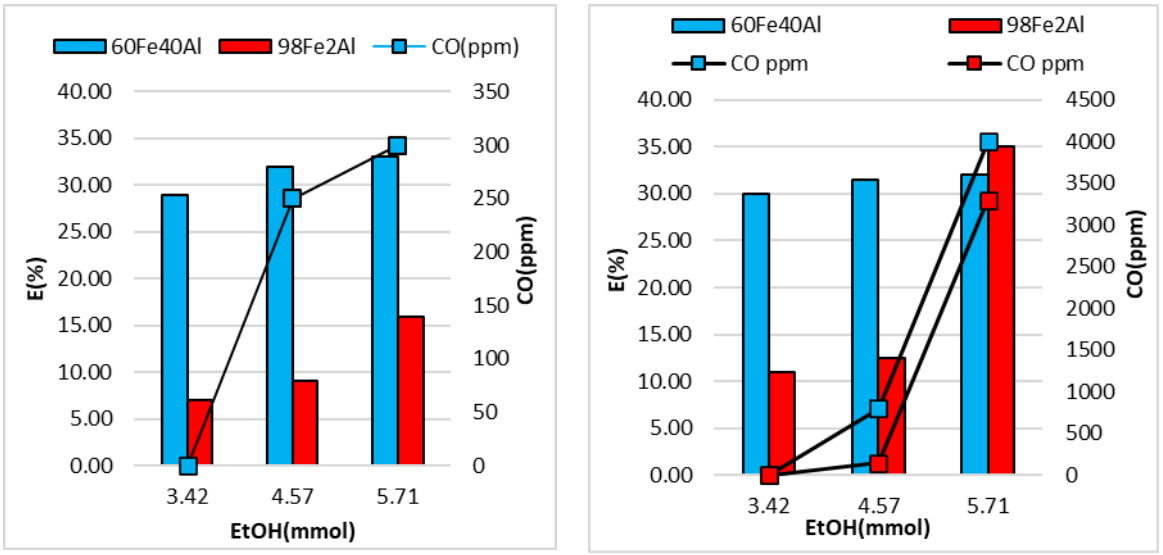

***Figure 7.2**: process efficiency(bars) and CO maximum concentration(lines) obtained with the samples 60Fe40Al and 98Fe2Al. A) 675°C B)750°C*

Looking at efficiency values, it is evident that the amount of Al_2O_3 added to iron oxides is a key parameter in the production of pure H_2. Al_2O_3 enhances the accessibility of iron active sites conferring to the Fe-based sample an higher surface area (table 7-1) but at the same time its addition decreases the H_2 purity catalysing cracking reactions and therefore the rate of carbon formation during reduction. These opposites effects are clearly visible in figure 7.2; at constant ethanol amount fed, the H_2 yield assumes the highest value when Al_2O_3 concentration in the sample is equal to 40 % reaching a maximum process efficiency of 30 % at 750°C and 3,42 mmol of ethanol fed in reduction. However, the high Al_2O_3 concentration in the sample mass always led to the production of H_2 contaminate by CO, except

in the tests were 3.42 mmol of ethanol are fed. On the contrary, at constant temperature of 675°C, the sample 98Fe2Al produce pure H_2 at all amounts of ethanol fed with a maximum E% value of 15.9%. in this case the low process efficiency values can be attributed to the severe diffusion limitations of gaseous reductants in the particle core [175] linked to the lower BET surface area of this sample (Table 7-1).

The opposite effects induced by the increases of temperature on the hydrogen purity and hydrogen yields is visible form the comparison of the 98Fe2Al performances at 675°C and at 750°C (figure 7.2). At constant amount of ethanol, the process efficiency values registered at 750°C (figure 7.2 B) are always higher than that obtained at 675°C (Figure 7.2 A) but at 750°C the sample cannot produce H_2 in the whole ethanol range, as registered at 675°C, but only when 3.42 mmol of ethanol are fed.

The results confirm the hypothesis that, the increase of temperature worsens the problem of carbon formation although it favours the iron oxides reduction, promoting thermodynamics and kinetic [176].

Influence of temperature and amount of Al_2O_3 added to Fe in the sample stability: Fe/Al interaction into 2 steps CLH

The influence of temperature on the long- term particles reactivity is evaluated for 10 redox cycles, feeding 3.42 mmol of ethanol in the reduction step, amount for which pure H_2 is always produced.

Figure 7.3 reports the process efficiency (E%) for the two samples (60Fe40Al and 98Fe2Al) as a function of the reaction temperature (675°C and 750°C).

A) 60Fe40Al, 2 steps CLH

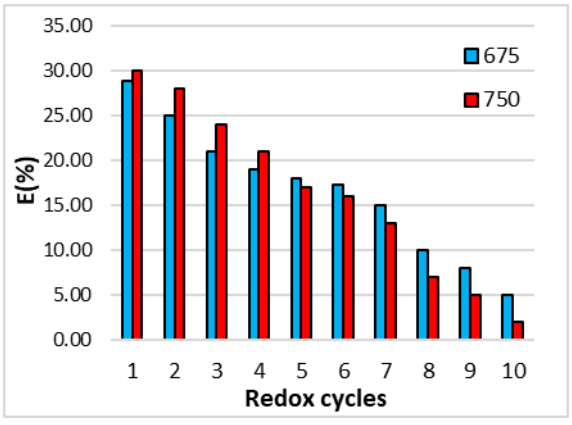

B) 98Fe2Al, 2 steps CLH

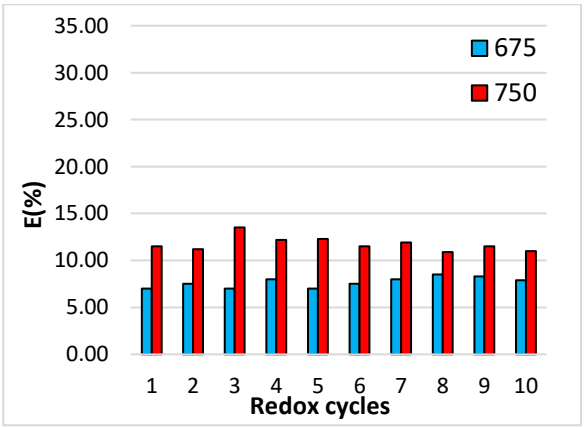

***Figure 7.3**: Process efficiency for 10 consecutive redox cycles when 3.42 mmol of EtOH are fed, 2 steps CLH. A) 60Fe40Al; B)98Fe2Al*

Looking at the results reported in figure 7.3, the added amount of Al_2O_3 is demonstrated to be a key parameter also on the long-term particle performances. At the higher Al_2O_3 content (60Fe40Al), the

sample shown a sharp decrease of the efficiency whereas the 98Fe2Al maintains constant its activity, with a slight variation of 10% around a medium efficiency value.

The efficiency of the sample 60Fe40Al (Figure 7.3 A) assumes the highest values among all the tested samples in the first few cycles, but a rapid deactivation is registered at each tested temperature. The increase of temperature has opposite effects in the process: it increases the hydrogen yield and enhance the spinel formation, responsible of sample deactivation. In fact, the enhanced temperature improves the efficiency only till the 4th while starting from cycles number 5, the trend becomes opposite (Figure 7.3 A), the efficiency values at higher temperature becomes lower those at 675 °C. These results demonstrate that the deactivation rate of 60Fe40Al depends on the reaction temperature, becoming faster at high temperature due to the formation of $FeAl_2O_4$ also detected in the XRD analyses (Figure 7.1). Several works in literature studied the $FeAl_2O_4$ formation in chemical looping H_2 processes ([177][178][179]) but the kinetics and reaction mechanism of hercynite redox cycles are still poorly understood.

The proposed redox mechanism of Fe/Al particles is reported in reactions 7.1-7.7.

Reduction pathway with H_2 of Fe/Al particles

$$3Fe_2O_3 + Al_2O_3 + H_2 \leftrightarrow 2Fe_3O_4 + Al_2O_3 + H_2O \quad (7.1)$$

$$Fe_3O_4 + Al_2O_3 + H_2 \leftrightarrow 3FeO + Al_2O_3 + H_2O \quad (7.2)$$

$$FeO + Al_2O_3 \leftrightarrow FeAl_2O_4 \quad (7.3)$$

$$FeAl_2O_4 + H_2 \leftrightarrow Fe + Al_2O_3 + H_2O \quad (7.4)$$

Steam Oxidation pathway

$$Fe + Al_2O_3 + H_2O \leftrightarrow FeO + Al_2O_3 + H_2 \quad (7.5)$$

$$FeO + Al_2O_3 \leftrightarrow FeAl_2O_4 \quad (7.6)$$

Air Oxidation

$$2FeAl_2O_4 + 0.5\ O_2 \leftrightarrow Fe_2O_3 + 2Al_2O_3 \quad (7.7)$$

$FeAl_2O_4$ is formed from the reaction of wustite (FeO) with Al_2O_3 and, according to the redox iron pathway, the FeO can be formed in both the process steps, in reduction (reaction 7.3) or during the oxidation (reaction 7.6) [180]. Furthermore, the $FeAl_2O_4$ oxidation with steam is not thermodynamically favored [181] and its conversion into the two separated oxides can be achieved only using a more sever oxidation step with air (reaction 7.6) or by a longer reduction, leading to the formation of Fe and Al_2O_3

(reaction 7.4) [182]. However, this last option would require higher amount of ethanol fed which is not compatible with the production of pure H_2, as demonstrated by the performed tests.
For the sample 60Fe40Al, the spinel formation regards a higher fraction of the sample mass due to the higher concentration of Al_2O_3, causing the sample deactivation at repeated cycles. Furthermore, XRD analyses of 60Fe40Al performed at the end of stability tests, demonstrated that the $FeAl_2O_4$ formation is favoured at higher temperature; the entire amount of Al_2O_3 added is in the spinel form after the test at 750 °C whereas a fraction of free Al_2O_3 is still detected at the end of stability test at 675°C (Figure 6.1) [183].
The different behaviour of 98Fe2Al sample in terms of particle stability is explained by the lower concentration of Al_2O_3 in the sample mass and, thus, on the negligible negative effect introduced by the Fe/Al chemical interaction. The spinel in this case confers to iron oxides the thermal stability needed thanks its high thermal resistence.

3 steps CLH configuration: influence of addition of air oxidation step on 60Fe40Al activity

The obtained results previously reported for the sample 60Fe40Al in the 2 steps CLH shows that 60Fe40Al is able to produce high process efficiency, but it suffers from deactivation. To make possible its utilization the air oxidation step is added to the process set-up (3 steps CLH). The 3 step CLH consists in a reduction, a steam oxidation and an air oxidation step. During the air oxidation step the $FeAl_2O_4$ is oxidized into Fe_2O_3 and Al_2O_3 according to reaction 7.6 [184] restoring the initial material properties.

Figure 7.4 reports the efficiency of the 3 steps CLH process for 10 redox cycles as function of temperature. The results confirm that the presence of the air oxidation let to overcome the issue of the Fe/Al interaction registered in the 2 steps CLH, at the expense of the complexity of the system, which requires an additional unit for the air oxidation. By increasing the temperature, the H_2 yields are always higher without registering any deactivation.

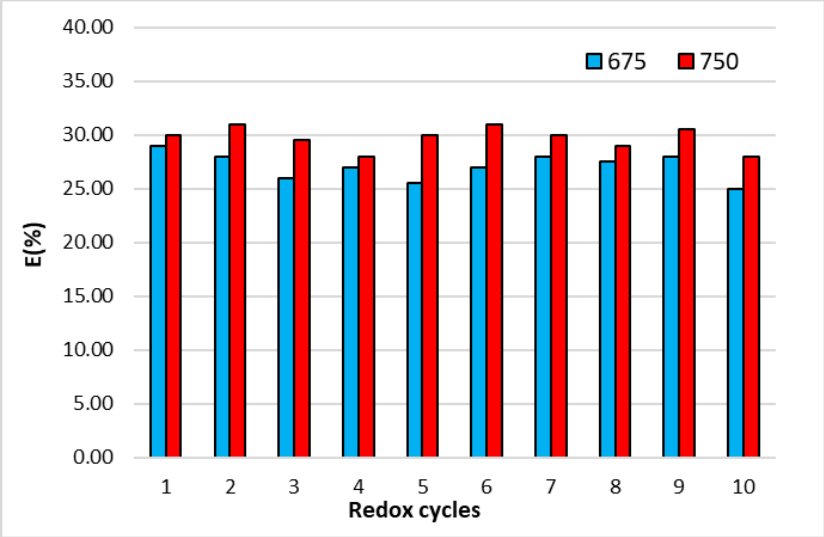

***Figure 7.4**:Process efficiency sample 60Fe40A as a function of temperature in the 3 steps CLH*

Influence of 2 wt% of MgO or CeO_2 addition on the activity and stability of iron oxides

To complete the series of tests using Al_2O_3, MgO and CeO_2 as structural promoters, stability tests are also conducted on the OCs having the 2 wt% of MgO and CeO_2. The stability tests are performed at 675°C and 750 °C by feeding 3.42 mmol of ethanol for 10 consecutive redox cycles. Figure 7.5 A reports the result of 98Fe2Mg while figure 7.5 B those obtained with the sample 98Fe2Ce.

A) 98Fe2Mg

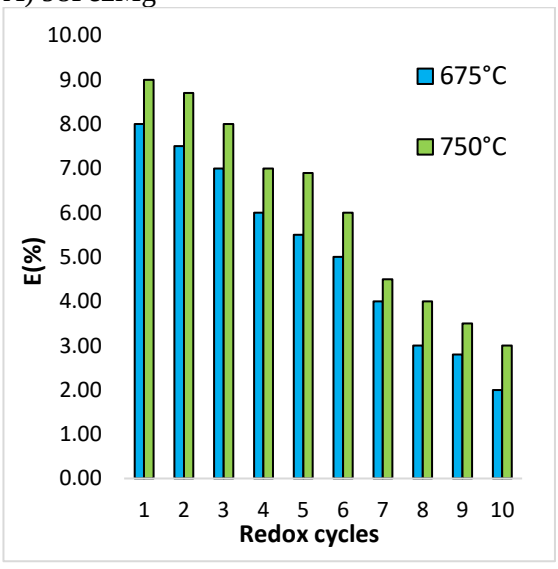

B) 98Fe2Ce

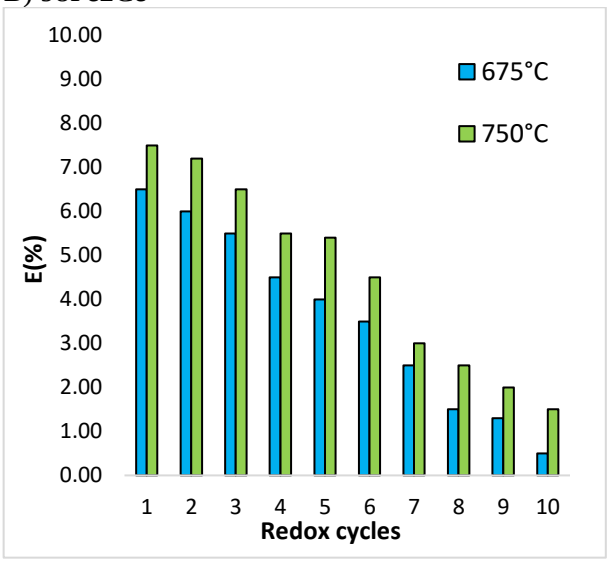

***Figure 7.5**: Process efficiency as a function temperature. A)98Fe2Mg; B)98Fe2Ce*

The results reported in the figure 7.5 show that although a pure H_2 is always produced, a rapid deactivation in 10 cycles occurs with both the doping elements, with a similar deactivation trend registered for undoped Fe_2O_3. If the addition of CeO_2 did not appear promising also when present in 40wt% in the sample mass (Chapter 6), the result of 98Fe2Mg is unexpected, since the addition of 40% of MgO showed constant activity for 10 consecutive redox cycles, producing the highest H_2 yields of the study.

The results suggest that, among the promoters analysed, only Al_2O_3 is able to confer the required thermal stability to iron oxides when present in the sample mass in 2 wt%. In the case of MgO an higher amount of promoter must be added to avoid the agglomeration/sintering phenomena traditionally present in the pure iron.

Based on the results obtained in the study, the use of CeO_2 as structural iron oxides promoter did not appear promising in the proposed system, and therefore the study of this material was limited to the results so far.

7.5 Conclusions

The results reported in this Chapter demonstrated that the effectiveness of Al_2O_3 as structural promoter of Fe is feasible only when low amounts of Al_2O_3 are added, due to the formation of a spinel $FeAl_2O_4$, that behaves as inert material in the 2 step CLH. The spinel formation is significantly affected by the reaction temperature, becoming faster at 750°C and so leading to a faster sample deactivation. By decreasing the amount of Al_2O_3 added to 2 % and so limiting the amount of spinel formed, the iron thermal stability is improved, the sample produces stable H_2 yield for 10 cycles with a positive effect on the iron reducibility, especially at 750°C. However, in the case of MgO and $CeO_{2.}$, the decrease of the amount added to 2 wt% did not appears promising to avoid the sintering/agglomeration phenomena as both samples suffer from a rapid deactivation.

To maintain high H_2 yields using 60Fe40Al, the addition of an air oxidation step (3 steps CLH) is fundamental to restore the Fe redox activity converting the inert $FeAl_2O_4$ into the separated oxides Fe_2O_3 and Al_2O_3. In this way the successful utilization of this material with a constant process efficiency for 10 cycles is obtained, demonstrating the feasibility of the process with an efficiency of about 30 % at 750 °C.

8. The synergistic effect of manganese and iron oxides in the maximization of pure H_2 production

8.1 Introduction

Based on the results of Chapter 7 the sample 98Fe2Al appears to be the best candidate in the 2 steps CLH. However, at high temperature (750°C) the production of pure H_2 is achieved only at low amount of ethanol fed. With the aim to fully exploit the positive effect of temperature on enhancing iron oxides reduction degree without compromising the H_2 purity, 1 wt% of manganese oxide (Mn_2O_3) is added to the sample 98Fe2Al. Mn_xO_y was already successfully tested mixed with Fe_2O_3 commercial powder. The results showed increased efficiency but due to the low resistance to high temperature of the two oxides the system went rapidly to deactivation. The aim of this study is to fully exploit the property of Mn_xO_y to avoid carbon deposition in the reduction phase, enhancing the partial/total consumption of the produced carbon exploiting the high mobility of the reticular oxygen atoms of manganese oxides compared to that of iron oxides.

In order to identify the optimal OCs composition, including the Mn oxides, in terms of activity, stability and resistance to carbon deposition, two different Fe-based materials were synthesized starting from the most promising material synthetized 98Fe2Al:

- **98Fe1Al1Mn** where is kept constant the active iron content to 98wt% (98% Fe_2O_3, 1% Al_2O_3, 1 % Mn_2O_3)

- **97Fe2Al1Mn**, where is kept constant the Al_2O_3 concentration to 2 wt% (97% Fe_2O_3, 2% Al_2O_3, 1% Mn_2O_3).

8.2 Experimental procedures

The samples were tested in a fixed bed reactor at two different reaction temperatures (675°C-750°C) maintaining the pressure constant at 1 bar. The fixed bed was constituted by 1 gram of Fe-based particles. The bench scale plant is described in detail in the Chapter 3. Different amounts of ethanol were tested (3.42 mmol, 4.57 mmol, 5.71 mmol) in order to assess the Mn-oxides effect on the sample reducibility and on the hydrogen purity. For each quantity fed, 10 consecutive redox cycles were conducted.

The experiments at higher ethanol flow rate are performed feeding 8 $mL \cdot h^{-1}$ for 3 minutes at constant redox temperature of 675°C.

8.3 Experimental results

Determination of the optimal sample composition in terms of H_2 yields and stability

In order to evaluate the effect of manganese oxide on carbon deposition, the two samples 97Fe2Al1Mn and 98Fe1Al1Mn are firstly tested at 750 ° C, condition at which the 98Fe2Al produce an H_2 stream contaminated by CO (Figure 7.2 B). As already explained in the Chapter 5, also Mn_xO_y participates to the redox cycles and the amount of hydrogen producible by its reduction-steam oxidation must be considered in the calculation of the H_2 theoretical to properly evaluate the influence of its addition on iron oxides reactivity.

Table 8-1 reports the maximum amount of hydrogen producible by the two samples and the contribution of each redox couple to the final value.

***Table 8-1**: Theoretical H_2 production by the samples examined.*

	H_2(NL) Couple Fe/Fe_3O_4	**H_2(NL) Couple MnO/Mn_2O_3**	**Total H_2 (NL) producible**
97Fe2Al1Mn	0.36301	0.00124	0.36425
98Fe1Al1Mn	0.36602	0.00124	0.36726

The process efficiencies values and the maximum CO concentration (if present) as a function of the amount of ethanol fed are shown in figure 8.1 A) for the sample 98Fe1Al1Mn and figure 8.1 B) for the 97Fe2Al1Mn.

A) B)

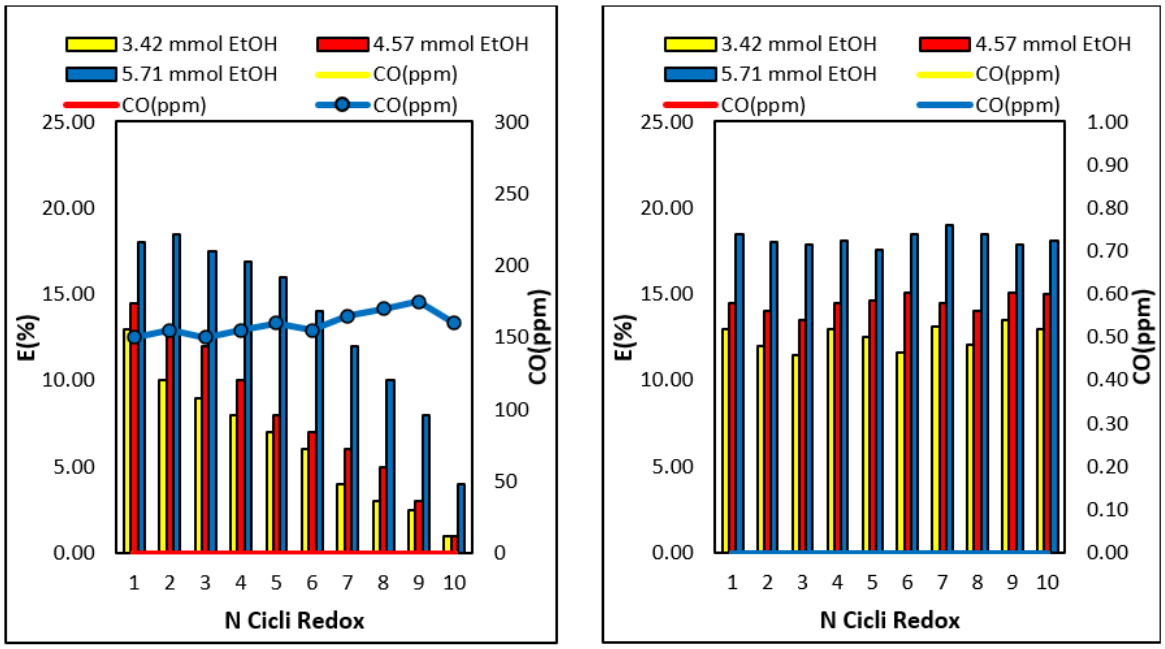

***Figure 8.1**: Process Efficiency for 10 consecutive redox cycles as a function on the ethanol fed at 750°C. A) 98Fe1Al1Mn; B)97Fe2Al1Mn*

The results reported in Figure 8.1 confirm that the promoter amount in the sample is a key parameter for the thermal stability. Looking at the results of the 98Fe1Al1Mn (Figure 8.1 A), where the Al_2O_3 concentration is 1wt%, the thermal stability of the sample is compromised, and a progressive deactivation of the sample is observed for all the quantities of ethanol fed. On the other hand, when Al_2O_3 is present at 2wt % (97Fe2Al1Mn), no deactivation occurs, the efficiencies oscillate around an average value and improve as the quantity of ethanol fed increases. As also reported in the Chapter 5, the addition of Mn oxides produces a positive effect on the reduction degree of the bed allowing to obtain pure H_2 even at higher amount of ethanol fed. Pure H_2 stream is obtained also when 4.57 mmol and 5.47 mmol of ethanol are fed. On the contrary, under the same operating conditions, sample 98Fe2Al, that does not contain Mn, produced increasing quantities of CO during the tests (CO max = 3300 ppm, figure 7.2).

The two samples with the addition of Mn were also tested at 675 ° C. Figure 8.2 A shows the efficiencies obtained with the sample 98Fe1Al1Mn as a function of the ethanol fed. The deactivation trend registered with 98Fe1Al1Mn is unchanged, in all the conditions the sample is progressively deactivated. Likewise, also at 675°C the sample 97Fe2Al1Mn shows constant efficiencies, with an increasing trend as a function of the amount of ethanol fed.

A) B)

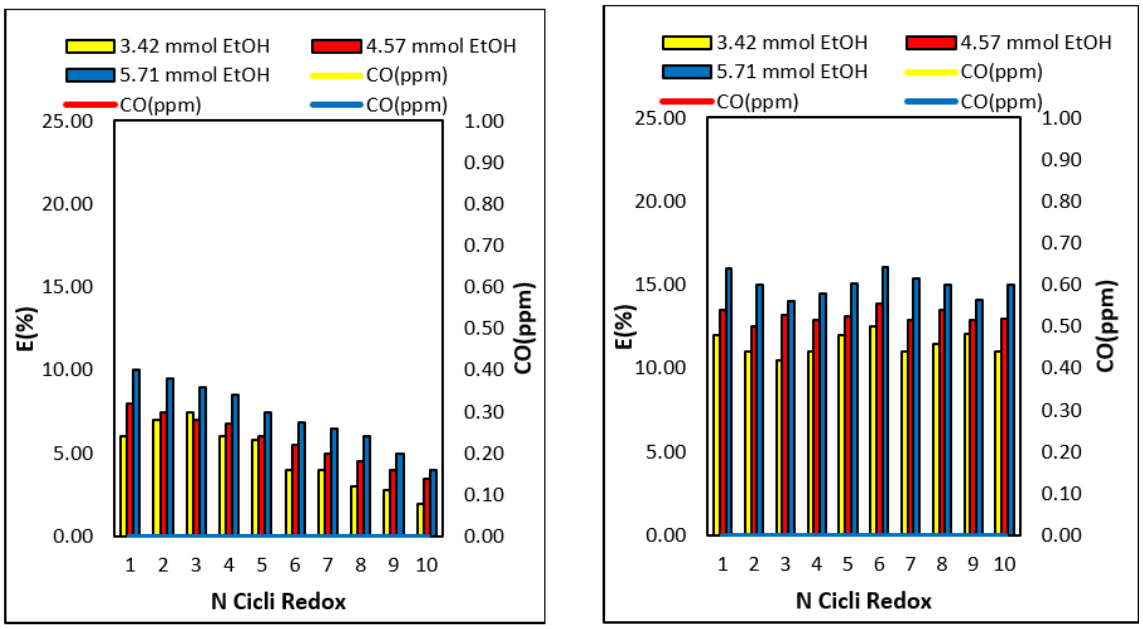

Figure 8.2: *process efficiency as a function of ethanol fed at 675°C; A) 98Fe1A1Mn. B)97Fe2Al1Mn*

The obtained results show that it is possible to exploit the properties of manganese oxide in the process but only if the content of Al_2O_3 remains constant at 2% by weight in the sample, otherwise the thermal stability of the material will be lost with consequent deactivation.

To highlight the effect of Mn_xO_y on improving the iron oxides reducibility, Figure 8.3 shows a comparison of the average efficiency values trend as a function of the amount of ethanol fed at 675 ° C obtained with the samples 98Fe2Al and 97Fe2Al1Mn.

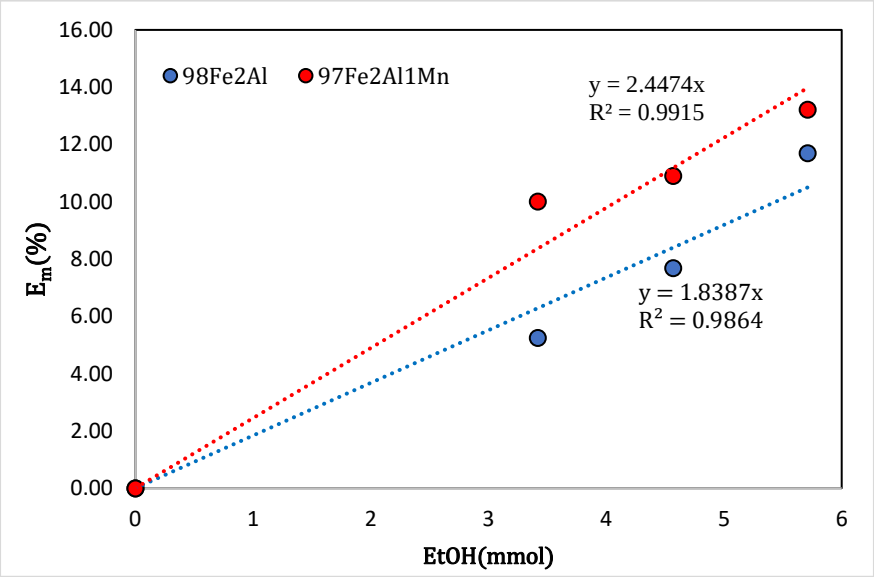

Figure 8.3: *Comparison of average process efficiency as a function of the ethanol fed with 98Fe2Al and 97Fe2Al1Mn. Experimental results obtained at 675°C.*

The results reported in figure 8.3 show that in the whole range of ethanol studied the amounts of hydrogen produced with the sample 97Fe2Al1Mn are always the highest, suggesting that a better reducibility can be achieved when Mn_2O_3 is added to the OCs. The ratio between the slopes of the two linear regressions suggests that the 97Fe2Al1Mn sample can exploit the reducing power of ethanol 1.3 times more than the 98Fe2Al sample.

Considering that the amount of Al_2O_3 is the same in both the samples and therefore the amount of active iron subtracts to the redox cycle due the formation of inactive $FeAl_2O_4$ is constant, the higher activity of the 97Fe2Al1Mn lies in the better reducibility of the active iron fraction. Figure 8.4 reports a comparison of the volume of the species resulted from the reduction step. The results are referred at the experiments conducted at 675°C feeding ethanol for 3 minutes (3.42 mmol).

Table 8-2 reports the carbon balance, made to validate the results

A)

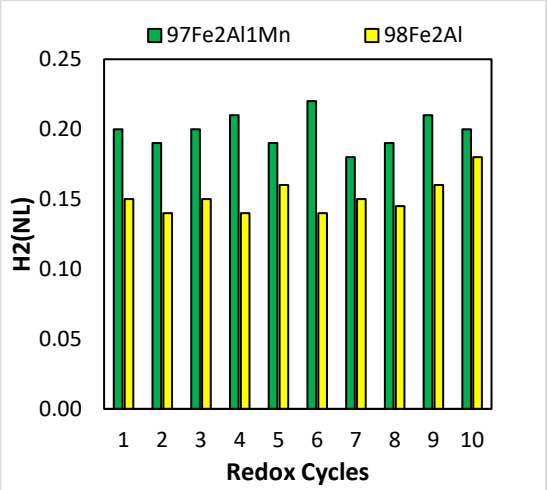

B)

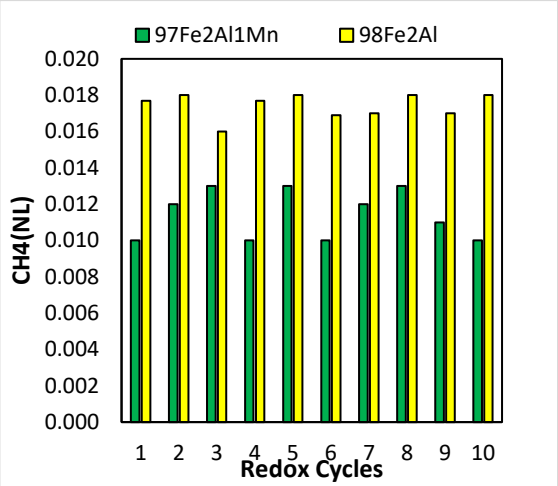

C)

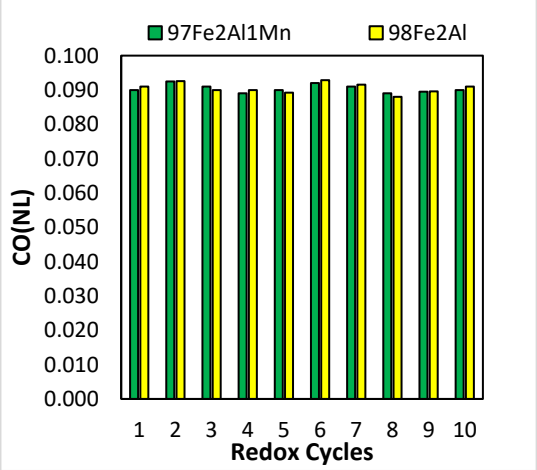

D)

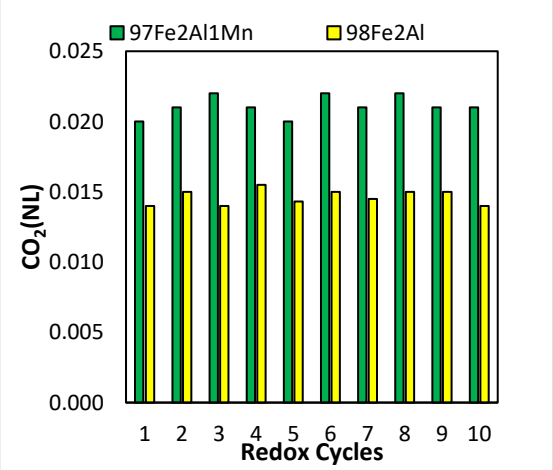

E)

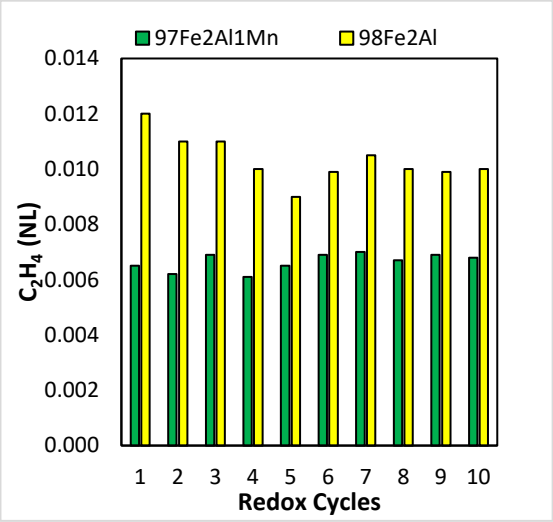

Figure 8.4: *Comparison of the volumes of species detected in the reduction step with the sample 97Fe2Al1Mn and 98Fe2Al. results referred at the experiments with 3.42 mmol of ethanol are fed at 675°C*

Table 8-2*:Carbon balance for the determination of the solid carbon conversion in the reduction step. Results referred to the tests at 675°C and 3.42 mmol of ethanol fed. comparison of 97Fe2Al1Mn and 98Fe2Al*

	Cin	**C_{out} with gases species**				
	C_{EtOH} (mmol)	CH_4 (mmol)	C_2H_4 (mmol)	CO_2 (mmol)	CO (mmol)	Δmol C (mmol)
97Fe2Al1Mn	6.84	0.59	0.79	0.93	4.22	0.21
98Fe2Al	6.84	0.86	0.99	0.69	4.08	0.22

Δmol C = mol C_{EtOh} - sum of mol C gaseous products

Looking at the results of Figure 8.4, at each cycle the sample 97Fe2Al1Mn produces a higher amount of H_2 and CO_2 during the reduction step while a lower light hydrocarbons concentration is detected, which is almost 35%-45% lower than the value obtained with 98Fe2Al.

In the Chapter 5 the influence of the addition of manganese on the redox activity of iron oxides in the proposed scheme was thoroughly investigated. The results showed that manganese oxides actively participate in the proposed redox system. Thanks to the high mobility of oxygen in its lattice, it is able to partially oxidize methane and ethylene into gaseous species (CO and H_2) improving the reducing power of the gaseous mixture, and at the same, solving the problem of carbon deposition on the surface of the reduced particles. As a consequence, the reduction degree of iron oxides is enhanced without compromising the hydrogen purity. The higher volumes of CO_2 detected (33% more than the value with

98Fe2Al) confirm the hypothesis, CO_2, in fact, is the product of the reduction reaction of the oxides by CO and solid carbon.

The carbon balance reported in Table 8-2 validate the results although a difference of 0.21 mmol for both the samples between the input and output carbon was identified; nevertheless, being this deviation within the error range of the instrument, it is considered negligible. The carbon balance results also demonstrated the absence of unreacted carbon on the OCs surface.

Influence of ethanol concentration in the redox performance of 97Fe2Al1Mn

The results obtained so far show that the addition of Mn oxides to the OCs let to overcome the main issue of the proposed system: the impossibility to maximize the hydrogen yield without compromising the hydrogen purity.

Considering the promising activity of 97Fe2Al1Mn, tests at higher ethanol flow rate (from 4 $mL*h^{-1}$ to 8 $mL*h^{-1}$) are performed. The increased ethanol flow rate allows the production of a gaseous reducing stream, resulted from its decomposition, having higher concentration of reducing species, considering that the tests are made with Ar as carrier gas, and thus, an enhanced reduction force. Obviously, in this condition, also the amount of solid carbon formed will increase.

Table 8-3 reports the molar percentage of the gaseous species measured during the reduction step at the two ethanol flow rates. As expected, the concentration of all ethanol decomposition products (H_2, CO, CH_4 and C_2H_4) is almost double with respect to the values obtained at 4 $mL{\cdot}h^{-1}$. The measured CO_2 molar concentration at 8 $mL{\cdot}h^{-1}$ is 3 times higher the measured value at 4 $mL{\cdot}h^{-1}$, suggesting that the iron oxides reduction by solid carbon and/or CO at higher ethanol flow rate is enhanced. In fact, based on thermodynamic evaluation (Bauer Glassner diagram, Figure 5.1) at the same reduction temperature, the use of a gaseous stream with higher reducing power allows a deeper reduction of iron oxides.

***Table 8-3**: Gas composition during the reduction step at different ethanol flow rates. Reduction temperature of 675°C.*

EtOH flow rate	**Reducing gas out composition**					
	H_2 (%)	CO (%)	CO_2 (%)	CH_4 (%)	Ar (%)	C_2H_4 (%)
4 mL·h-1	12.5	3.5	0.5	0.5	82.7	0.3
8 $mL{\cdot}h^{-1}$	25.1	8.0	1.5	1.2	63.6	0.6

The positive effect of higher reducing species concentration on the iron oxide reducibility is confirmed by the hydrogen yields in oxidation. Figure 8.5 A and Figure 8.5 B report the comparison of the efficiency values obtained in the 10 redox cycles at the two ethanol flow rates and the average efficiencies values, respectively. The results demonstrated that increasing the reducing agent concentrations in the examined range, the average efficiency value doubles (from 9.90 % at 4 $mL \cdot h^{-1}$ to 21.52% at 8 $mL \cdot h^{-1}$). Furthermore, the 97Fe2al1Mn is still able to produce pure hydrogen for 10 consecutive cycles, confirming the feasibility of the system proposed in the production of pure hydrogen also at higher concentration of ethanol.

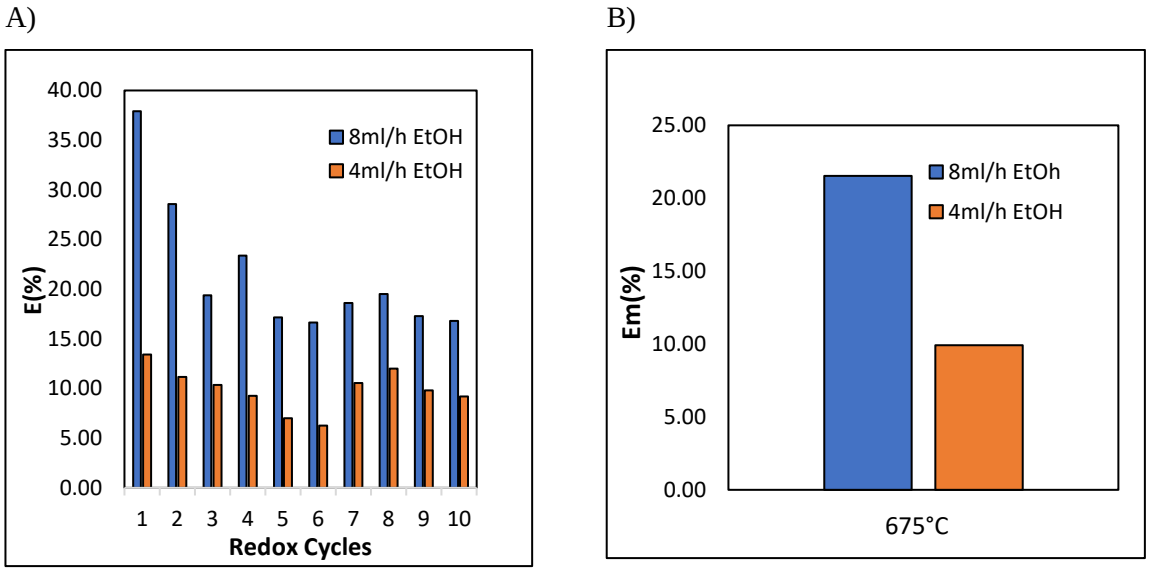

***Figure 8.5**: Tests with different ethanol flow rates (8 mL/h and 4mL/h) at 675 °C and reduction length of 3 minutes A) Process efficiency values for each cycles B) Average E% values*

8.4 Conclusions

The addition of Mn_xO_y in the sample 98Fe2Al appears to be the best choice to maximize the efficiency of the process guarantying the production of pure hydrogen. The higher lattice mobility of Mn_xO_y oxygen atoms with respect to the iron oxides allows the conversion of deposited carbon into gaseous species at each cycle, solving the issues related to H_2 contamination and sample deactivation due to the accumulation of unreactive carbon on the OCs surface. Furthermore, the carbon conversion into gaseous species let the formation of a gaseous stream with higher concentration of H_2 and CO and thus having a higher reductant power. The positive effect on iron oxides reducibility is confirmed by the higher amounts of pure hydrogen produced in oxidation obtained with the sample 97Fe2Al1Mn.

The enhanced activity of 97Fe2Al1Mn is also tested by feeding higher flow rate of ethanol in the reduction step with the aim of promoting the iron oxides reduction degree by increasing the concentration of reducing agents. Under these conditions, the highest amount of pure hydrogen pure using OCs with 2wt% of Al_2O_3 is achieved, reaching an average efficiency of the process value of 21.52%.

9. TGA analysis

9.1 Introduction

The results presented in this work demonstrate that OCs activity in the water splitting reaction is strongly depended on the ability of the sample to exchange oxygen atoms during the redox cycles. The OC in fact, lose oxygen atoms reacting with a fuel during the reduction step and regaining them during the oxidation with steam. When the aim is the pure hydrogen production also the rate of oxygen exchange becomes a key parameter, as a high oxygen mobility is needed to avoid carbon deposition during the reduction step (Chapter 8).

Based on the experimental results obtained so far, the addition of promoters significantly affects the oxygen exchange capacity of OCs. When a high amount of Al_2O_3 is added to hematite-based sample, the iron oxide reactivity changes; it always improves the hydrogen yields at the first redox cycles but in the long-term application it causes the sample deactivation due the formation of $FeAl_2O_4$, inactive under the operative conditions adopted. On the contrary, when MgO is used as promoter, the spinel formation does not prevent the hydrogen production by chemical looping technologies; in this case, in fact, the spinel participates in the redox reactions behaving as the Fe.

In the following section, to understand the origin of the different performance of the OCs in the presence of Al_2O_3 and MgO as promoters, temperature programmed reduction (TPR) was employed. To evaluate the influence of promoter in the sample reducibility, the TPR analysis is conducted on the samples having different promoters concentrations (98Fe2Al and 60Fe40Al, 98Fe2Mg and 60Fe40Mg) comparing the results with those obtained with pure Fe_2O_3.

To evaluate the positive effect of Mn_2O_3 addition on the sample reducibility a TPR analysis on 97Fe2Al1Mn is also performed.

TPR analysis: Mechanism Insight

The TPR profiles of the pure Fe_2O_3 and of samples with 2 wt% of promoters added are reported in Figure 9.1 A-D.

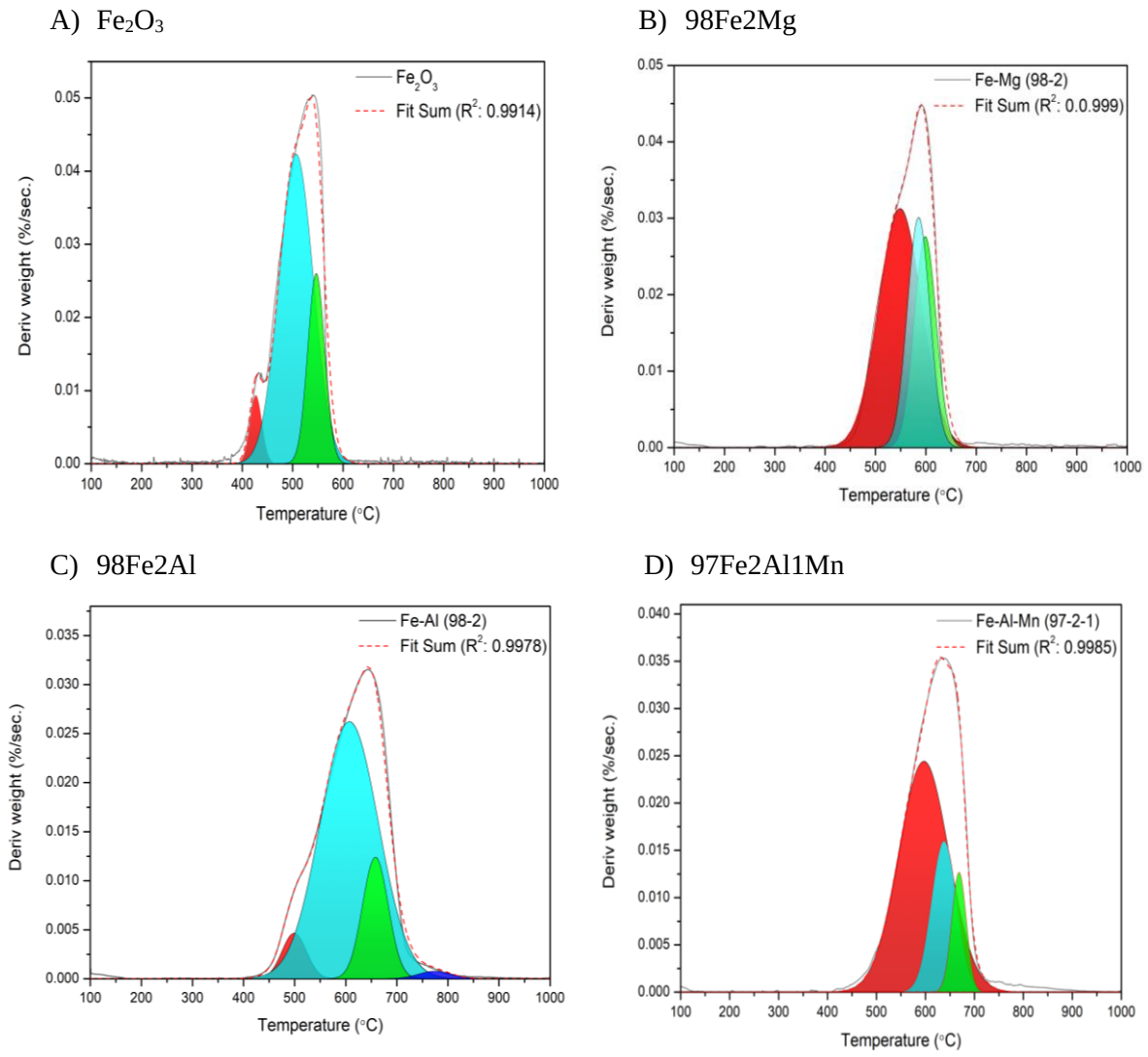

***Figure 9.1**: TPR profiles of the samples A) Fe_2O_3; B)98Fe2Mg; C)98Fe2Al;D)97Fe2Al1Mn*

The TPR profile of pure Fe_2O_3 (Figure 9.1 A) shows that the reduction to metallic iron occurs into mainly three phases partially overlapped:

i) Fe_2O_3 reduction (red curve) occurs in the temperature range 400°C-450°C with the highest weight loos rate at 425°C.

ii) The reduction of Fe_3O_4 to FeO (light-blue curve) starts at 400°C with a maximum weight loss rate at 500°C. The complete reduction to FeO is reached at 600°C.

iii) FeO reduction to metallic Fe (green curve) occurs in the temperature range (500°C-600°C) having the maximum weight loss rate at 550°C. The complete reduction to Fe is reached at 600°C.

The results confirm that to completely reduce iron oxides up to the iron phase and thus to maximize the H_2 yields by chemical looping technologies, the reduction step must be performed at high temperature (T > 600°C). When Al_2O_3 and MgO are added to hematite, the rate of reduction of iron oxides completely changes. Specifically, a lag effect on the iron oxide reduction rate is registered.

Observing the TPR profile of the sample 98Fe2Al (Figure 9.1 C), the effect of the chemical reaction between FeO and Al_2O_3 to produce $FeAl_2O_4$ is clearly visible. The peak at 500 ° C corresponds to the hematite reduction to magnetite which is increased by 50 ° C compared to the results of pure Fe_2O_3 sample. In the reduction region from Fe_3O_4 to FeO (light-blue peak) significant differences are detected: in sample 98Fe2Al the weight loss rate is extended up to 800 °C while with pure Fe_2O_3 the complete reduction of wustite is already reached to 600 °C. This delay effect introduced by the presence of 2% by weight of Al_2O_3 could be attributed to the formation of the spinel, that increases the complexity of reduction of iron oxides mechanism by adding another reaction in the region of FeO formation thus causing the enlargement of the peak. It is worth to highlighted that the completion of this step of reduction is fundamental to produce hydrogen by chemical looping technology as without the formation of FeO and Fe phase, hydrogen cannot be produced by steam oxidation. However, when the amount of Al_2O_3 added to the iron oxides is only 2 wt% of the sample mass, this phenomenon regards only a small fraction of the wustite produced and the free wustite can be rapidly reduced to iron as visible in the green peak at 650°C. For the conversion of $FeAl_2O_4$ into Fe and Al_2O_3, higher temperature is needed (790°C, blue peak).

The TPR profile for the 98Fe2Mg sample (Figure 9.1 B) shows good reducibility of the material, The sample is reduced in 3 steps as measured for pure hematite sample and the peak of wustite formation is distributed in a temperature range lower than the 98Fe2Al (500°C-600°C). These results confirm that the spinel formed from Mg and Fe interaction owns good redox properties and if its formation concerns a small fraction of the total sample mass (2%), it does not significantly change the redox kinetics of iron.

Comparing the TPR profile of 98Fe2Al and 97Fe1Al1Mn (figure 9.1 C and D, respectively), the gain obtained by the presence of Mn_2O_3 in the oxygen exchange capacity is clearly visible. The spinel formation seems avoided, the lag effect of the wustite region is not registered and the peak related to the spinel decomposition is not present. The absence of spinel formation favours the complete reduction to metallic iron at lower temperature (750°C) with respect the temperature needed for the sample 98Fe2Al (825°C).

The TPR profiles of the sample having 40 wt% of promoter added (Figure 9.2 A-B), highlight the negative effect of spinels formation on iron oxides reduction rate.

A) 60Fe40Al

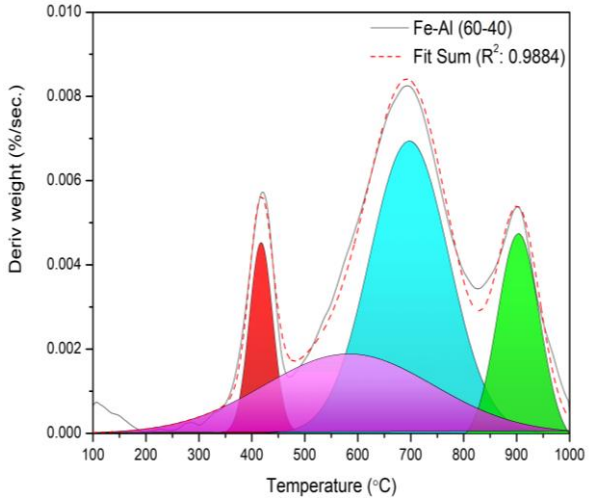

B) 60Fe40Mg

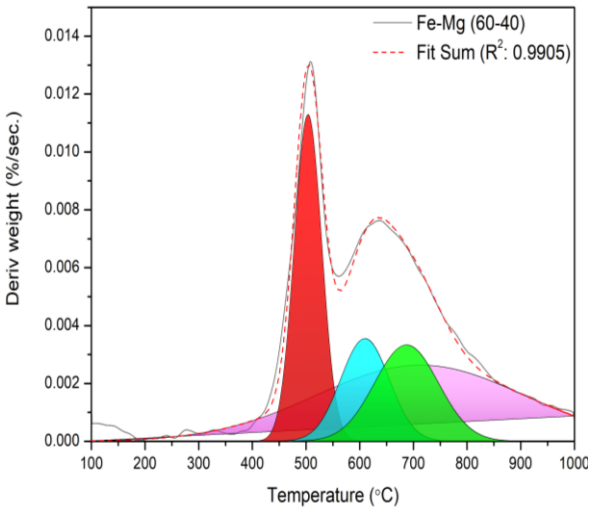

Figure 9.2: *TPR profiles of the samples. A) Fe_2O_3. B) 97Fe2Al1Mn .C)98Fe2Al. D)98Fe2Mg. E)60Fe40Al. F)60Fe40Mg.*

For both samples, 60Fe40Al (figure 9.2 A) and 60Fe40Mg (Figure 9.2 B), the complete reduction to metallic iron is achieved at temperatures significantly higher than those required for pure Fe_2O_3. In the case of 60Fe40Al the reduction to Fe can be considered complete only at 1000°C while with MgO is achieve at 800°C. The violet peaks detected for both the samples over the whole temperature range examined can be related to diffusion limitation in the solid matrix due to the formation of the spinel and to the difficulty of desorption from the sample pores of the water produced by iron oxides reduction with hydrogen, as these two samples own a higher pore density. Furthermore, the high performance of the sample 60Fe40Mg are also visible in the TPR profile. Instead of the results of 60Fe40Al where the peak of iron starts to appear after the peak of wustite in the case of 60Fe40Mg the iron peak overlaps the peak of wustite, appearing already at 550°C.

9.2 Conclusions

The OCs ability of transfer oxygen atoms during the redox cycles is the key parameter that must be optimized to efficiently produce hydrogen through chemical looping technology. Based on the experimental results obtained so far also the rate of OCs oxygen exchange is a fundamental parameter aiming at the production of pure hydrogen from bioethanol. In fact, the synthesis of OCs able to exchange oxygen more easily is crucial to improve the rate of reduction of iron oxide without compromises the hydrogen purity. The TPR analysis make possible to deeply study the reduction mechanism of iron oxides and the influence of promoters of each step of the reduction, fundamental to individuate the best material among the OCs studied and the optimal thermal conditions for which the sample reduction is maximized.

The comparison of the TPR profiles of the pure Fe_2O_3 and of the doped OCs, demonstrated the key role of promoters on the kinetics of iron oxides reduction. The formation of spinel structures enhances the complexity of iron oxides reduction pathway, increasing the number of steps required to reach the metal phase and slowing down the reduction rate. Although the structural promoter addition is fundamental to solve the issued linked to the low iron thermal resistance it adversely affects the amount of hydrogen producible by water splitting. Decreasing the amount of promoter in the sample mass the lag affect can be reduced but not avoided.

However, difference among MgO and Al_2O_3 promoters are detected. The formation of $FeAl_2O_4$ spinel slow down the reduction rate in the region of FeO formation due the chemical reaction between the two oxides (FeO and Al_2O_3) while in the case of MgO the spinel $MgFe_2O_4$, already present after the sample synthesis, appears more reducible.

The addition of 1wt% of Mn_2O_3 in the sample 97Fe2Al1Mn seems to be a promising solution to the kinetics problems introduced by the presence of Al_2O_3, improving the oxygen transfer and avoiding he formation of spinel between Fe/Al.

10. Scale-up solution: the use of Fe-based foam in the CLH

10.1 Introduction

Based on the promising results obtained with the OCs synthetized by coprecipitation method, a solution for the scale- up of the bench plant with a fixed bed reactor is proposed.

The fixed bed reactor configuration allows to perform the redox cycles consecutively in a batch mode, enabling a system design with a low degree of complexity due to the absence of moving parts, making the scale up easier than the fluidized bed mode operation. However, one of the main challenges of the fixed bed reactors scale-up is related to the high pressure drop of the reactor, strongly linked to the geometry of Fe-based material and to the amount of redox material loaded. The synthesis of a tailored Fe-based material with a high grade of porosity is therefore fundamental to make possible the scale-up of the system.

In this Chapter, the redox activity and the thermal stability of a highly interconnected porous doped Fe_2O_3 foams (FeFOAM) are investigated; a picture of the FeFOAM tested is reported in figure 10.1

The FeFOAM samples are synthetized by Freeze casting Technique at the Department of Materials and Transports at the University of Seville by the research group of Prof. Sepulveda.

The highly interconnected structure of FeFOAM prevents the iron sintering and pore clogging during the redox operations guaranteeing a stable amount of hydrogen produced at each cycle. The use of FeFOAM appears a promising solution for the scale- up of the proposed system, enhancing the activity of the OCs, the thermal stability and the heating transfer in the fixed bed.

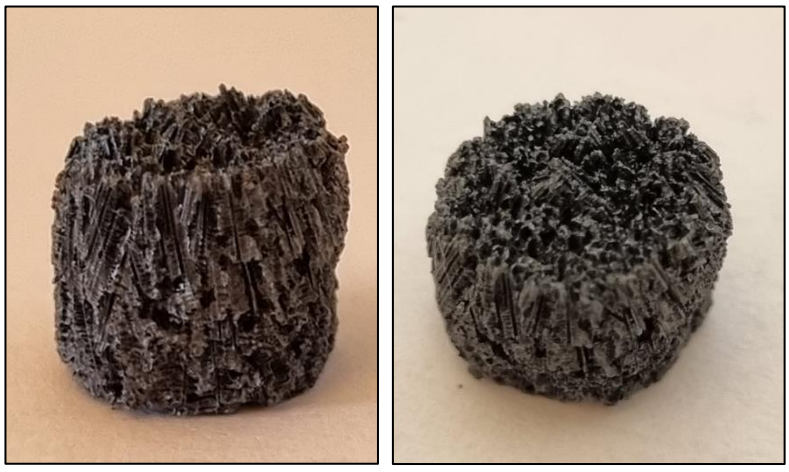

Figure 10.1*: Pictures of the FeFOAM sample before test.*

10.2 Experimental procedures

The FeFOAM samples were tested in a fixed bed reactor at two different reaction temperatures (675°C-750°C) maintaining the pressure constant at 1 bar. The fixed bed was constituted by an amount of 1 g of FeFOAM. The FeFOAM are tested in the bench scale plant described in detail in the Chapter 3.

10.3 Experimental results

Control of the ethanol amount fed in isothermal conditions (675°C): Pure H_2 production

The feasibility to produce pure H_2 with the FeFOAM sample was first evaluated in isothermal conditions (675°C) by following the same procedure adopted for the particles. First, the optimal amount of ethanol in the reduction step is determined by feeding 3 different amounts of ethanol (3.42 mmol, 4,57 mmol and 5.71 mmol of C_2H_5OH) in order to avoid the presence of coke deposition on the material and thus of CO in oxidation. At each condition, the thermal resistance of the sample was evaluated performing 10 consecutive redox cycles.

Figure 10.2 compares the process efficiency values and the maximum CO concentration detected (if presents) in each oxidation step as a function of the ethanol fed.

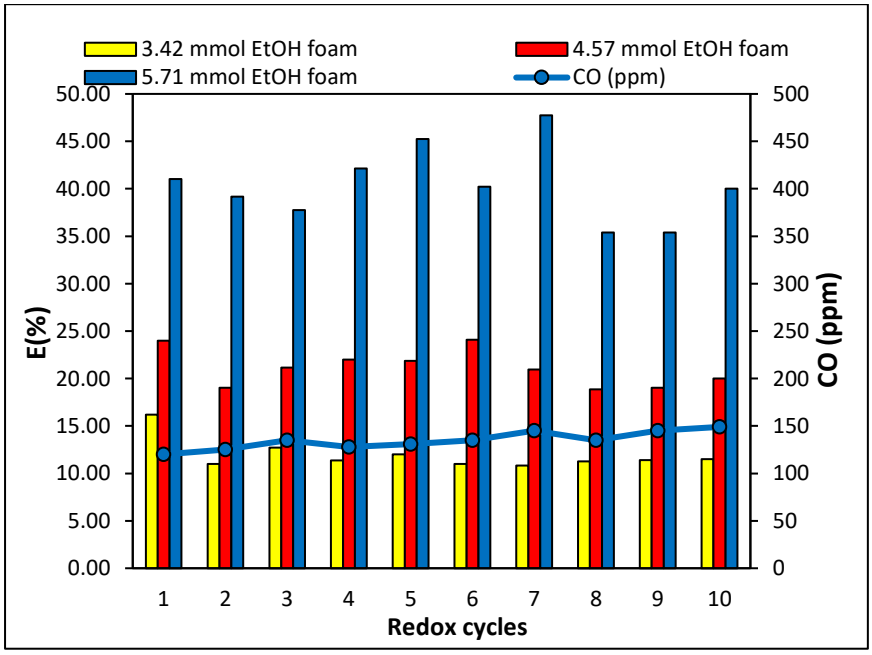

Figure 10.2: Efficiencies of the process and CO profile with FeFOAM at 675°C for 10 consecutive cycles, as a function of the amount of ethanol fed in reduction.

The results reported in Figure 10.2 confirm the relationship between the amount of ethanol fed and reduction degree of iron oxide, the efficiency values at higher ethanol amount are always enhanced. Furthermore, no deactivation in H_2 production was detected demonstrating that the presence of 2 wt% of Al_2O_3 confers an excellent thermal resistance to the material also in the Foam shape, guaranteeing the production of stable H_2 yields for 10 consecutive redox cycle.

The sample FeFOAM appears to be significantly more active, in all tests the process efficiency values were approximately double those obtained with 98Fe2Al in the same conditions (e.g. E≈12 % with FeFOAM with respect to E≈5% obtained with 98Fe2Al, when 3.42 mmol of ethanol are fed).

Since the chemical composition of the examined samples was the same (98 wt% Fe_2O_3-2 wt% Al_2O_3) the enhanced activity of FeFOAM confirms the positive effect introduced by the interconnected structure of the FeFOAM, which improving the accessibility of the iron active sites, led to a deeper iron oxide reduction and a more efficient iron oxidation [126].

The different performances between the two samples were also relieved on the purity of the produced H_2. Specifically, at redox temperature of 675°C, pure H_2 was always produced with the sample 98Fe2Al at each ethanol amount (Chapter 7, figure 7.2), while approximately an amount of 150 ppm of CO is detected with FeFOAM when 5.71 mmol of ethanol are fed (Figure 10.2, blue line). The presence of CO in oxidation proves that carbon deposition during reduction step is occurred. However, in these conditions, the process efficiency reaches the highest values, equal to approximately 40 %, due to the additional H_2 produced by carbon gasification.

The presence of CO in the FeFOAM sample at the highest ethanol amount fed, in fact, is connected to the lower concentration of oxygen in the sample mass at the end of the reduction step, caused by the deeper reduction degree reached.

The enhanced performance of the FeFOAM is also visible in Figure 10.3, where the relationship between the average process efficiency values and amount of ethanol fed is studied.

The results demonstrated a linear relationship between E_m(%) and ethanol fed in reduction in the region of pure hydrogen production for both the samples. The average process efficiency value of FeFOAM at 5.71 mmol of ethanol fed is not considered in the linear regression since under these operative conditions a hydrogen stream contaminated by CO was obtained, and therefore the hydrogen final volume also includes the additional hydrogen produced by the gasification reaction of the deposited carbon. According to the linear regression, in fact, The FeFOAM average efficiency at 5.71 mmol of ethanol fed is significantly higher than the value predicted by the linear regression.

At constant ethanol amount fed, FeFOAM was able to exploit the ethanol reducing power 2.28 times more than the 98Fe2Al. At the optimal ethanol value for FeFOAM (4.57 mmol) the average process efficiency value was equal to 21.98%, while only an efficiency of 5.1% is obtained with 98Fe2Al in the same conditions.

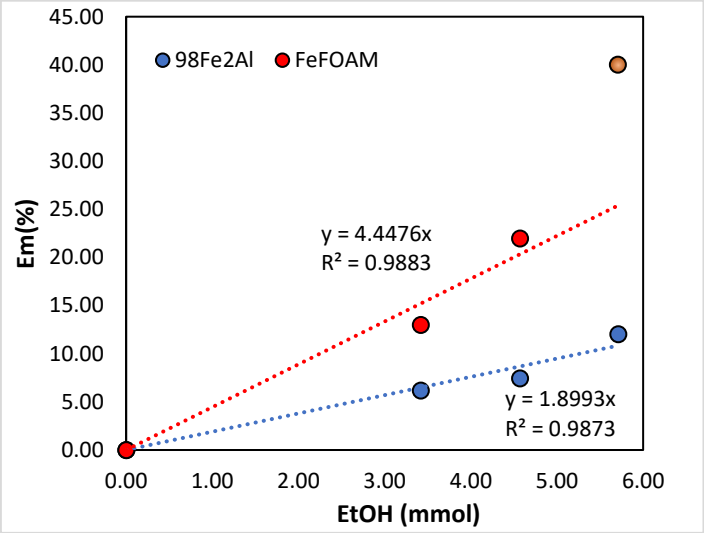

Figure 10.3: *Average process efficiency (Em) as a function of ethanol fed. Comparison of FeFOAM and 98Fe2Al*

The ratio H_2 produced/ethanol consumed is a fundamental parameter for the scale-up of the technology, which directly affect the costs of the proposed system. Table 10.1 reports the values of the ratio H_2 produced/ethanol consumed at the optimal ethanol amount for the samples FeFOAM and 98Fe2Al tested at 675°C. In the case of FeFOAM, 17.99 mL of H_2 were produced when a gram of Fe_2O_3 is used as redox material and 1 mmol of ethanol is consumed for the reduction. In the same conditions, only 7.88 mL are produced by 98Fe2Al sample.

Table 10-1*: Pure H_2 and optimal amount ratio for FeFOAM and 98Fe2Al at 675°C.*

Sample	**H_2(mL·g$^{-1}_{Fe2O3}$)**	**EtOH consumed (mmol)**	**H_2/EtOH consumed (mL·g$^{-1}_{Fe2O3}$· mmol$^{-1}_{EtOH}$)**
FeFOAM	82.24	4.57	17.99
98Fe2Al	45.01	5.71	7.88

Influence of temperature on the H_2 purity

In order to understand the effect of temperature on the performances of the FeFOAM in pure H_2 production, tests at different temperatures were performed (675°C, 700°C and 750°C). A number of 10 consecutive redox cycles were conducted at each temperature to evaluate the particle's stability.
Figure 10.4 shows the process efficiency and the CO profile as a function of the amount of ethanol fed in reduction obtained when the redox temperature was 750°C.

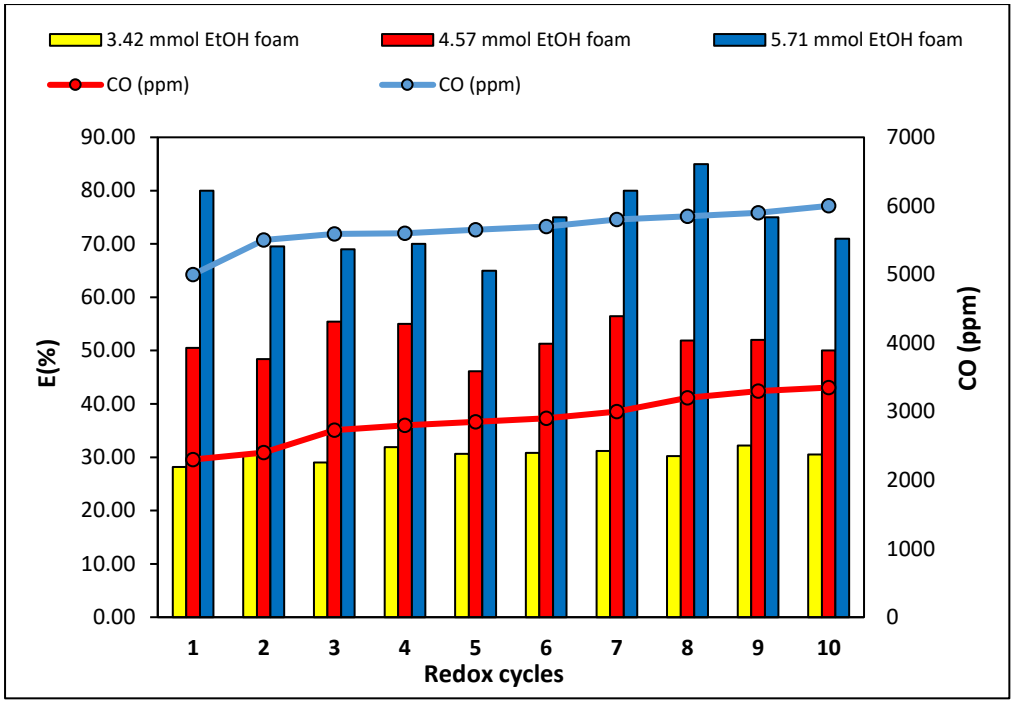

***Figure 10.4**: Efficiencies of the process and CO profile obtained with FeFOAM at 750°C.*

Looking at the results reported in Figure 10.4 by increasing the reaction temperature from 675°C to 750°C no sample deactivation was registered for 10 consecutive redox cycles, demonstrating the improvement on the thermal resistance of Fe offered by the addition of 2 wt% of Al_2O_3. However, the CO profiles reported in the Figures 10.4 show that the issues related to carbon deposition, accelerated by the higher temperatures, lead to a decrease of the optimal ethanol value. In the test with FeFOAM, a CO concentration equal to 2300 ppm starts to appear in the first oxidation step when the ethanol fed is equal to 4.57 mmol (value for which no CO was detected in the experiments at 675°C). The CO concentration slightly increase during the 10 cycles reaching 3350 ppm at the cycle number 10, suggesting that, cycle after cycle, the carbon accumulates on the material surface. The same carbon accumulation trend is registered when 5.71 mmol of ethanol are fed.

Based on the results obtained, the optimal ethanol value for both the sample is equal to 3.42 mmol, value for which the FeFOAM sample owns a major activity of 98Fe2Al at each cycle (E≈30. % with FeFOAM with respect to E≈9.0% obtained with 98Fe2Al).

Influence of temperature on the process efficiency: comparison of FeFOAM and 98Fe2Al

The effect of temperature on H_2 yields is visible in Figure 10.5, where a comparison of the average process efficiency values obtained with FeFOAM and 98Fe2Al as function of the redox temperature is reported. Since the efficiency values are influenced by the optimal ethanol amount fed that, as already demonstrated in the previous section, temperature changes are studied at constant ethanol amount fed

equal to 3.42 mmol. At this value in fact, the pure H_2 production is always obtained at each temperature for both the sample.

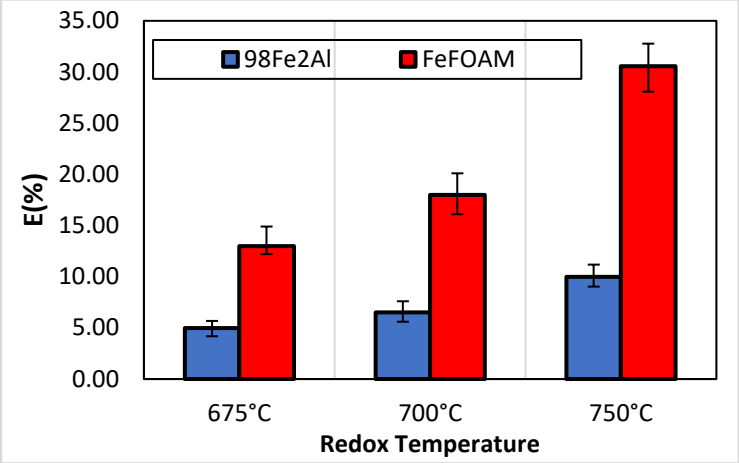

***Figure 10.5**: Average process efficiency values as a function of temperature when 3.42 mmol of ethanol are fed in reduction. Temperature tested (675°C-700°C-750°C)*

The results collected in Figure 10.5 suggest that the interconnected structure of FeFOAM allows to exploit the positive effect introduced by the higher temperature on the iron reduction degree more than the 98Fe2Al. At 750°C, FeFOAM appears significantly more active in H_2 production with respect the results obtained at 675°C; the average efficiency value was 13.9% while by increasing the temperature until 750°C, it reaches 30.1 %, with no detection of CO in H_2 stream. The increase of temperature in the case of FeFOAM sample promotes the iron oxides reduction favouring at the same time the consumption of carbon during this phase, allowing the production of pure H_2 also with high H_2 yields.

***Table 10-2**: Pure H_2 ethanol amount ratio for the FeFOAM and 98Fe2Al at 750 °C*

Sample	**H_2(mL·g$^{-1}_{Fe2O3}$)**	**EtOH consumed (mmol)**	**H_2/EtOH consumed (mL·g$^{-1}_{Fe2O3}$· mmol$^{-1}_{EtOH}$)**
FeFOAM	114.38	3.42	33.44
98Fe2Al	37.33	3.42	10.91

For both the samples the H_2/EtOH ratio increases with respect the results at 675°C. Also looking at this parameter, the FeFOAM appears to be significantly more efficient in the pure hydrogen production region (FeFOAM: from 17.99 at 675°C to 33.44 at 750°C; 98Fe2Al: from 7.88 to 10.91 at 750°C).

10.4 Conclusions

The use of a highly porous OCs is fundamental to decrease the pressure drop of the fixed bed rector and make possible the reactor scale-up.

FeFOAM is demonstrated to be the best choice for the possible scale up of the system studied. The highly interconnected porous structure confers to the material high activity, excellent thermal resistance at repeated redox cycles and very low pressure drops. Furthermore, FeFOAM appears much more active than the sample having the same chemical composition but different shape (98Fe2Al). At constant operative conditions, the FeFOAM produces 3.34 times more hydrogen than 98Fe2Al (efficiency of 21.98% with respect to 7.2% with 98Fe2Al, at 675°C and 4.57 mmol of ethanol fed in reduction).

11. Conclusions

Chemical Looping Hydrogen process is a very promising technology able to produce directly green and pure hydrogen from renewable sources. In a detailed literature review the recent advances achieved in chemical looping technologies were presented. The activity of R&D for the optimization of Fe-based oxygen carriers is focused on the synthesis of materials with enhanced thermal stability and redox reactivity, achieved thanks the addition of structural and electronic promoters. Extensive kinetic studies on the OCs redox performances provided data for mathematical modelling and for a better understanding of the reactions on a molecular level, which ensures further progress in the field of OCs synthesis. In recent years, the process development led to the construction of several prototypes up to 50 kW, most of them operating in fluidized bed reactors.

The main objective of this work is to demonstrate the feasibility of producing pure and renewable H_2 by Chemical Looping Hydrogen process, suitable to be directly fed to the PEMFCs. However, for their correct functioning, PEMFCs required a highly pure hydrogen stream, with a strict limit in CO concentration (CO<10ppm), a poison of PEMFC catalyst. The feasibility of the process is evaluated in a fixed bed reactor using bioethanol as renewable sources of reductants (H_2, CO and C) and iron as redox element.

The feasibility of using ethanol as a source of reducing agent was first demonstrated using commercial fine Fe_2O_3 powder as redox material. At the adopted operating conditions (T = 675 °C and P = 1 atm), ethanol was completely decomposed in a gaseous mixture constituted mainly of H_2 and CO, and thus owning high reducing force. However, in these conditions the solid carbon formation, detrimental for the H_2 purity, was also favoured. In fact, if carbon remains on the Fe reduced particles surfaces, at the beginning of the oxidation step, it reacts with steam, producing H_2 and CO by gasification reaction. A strict control of the ethanol feeding time was found to be crucial to limit the amount of solid carbon formed monitoring the iron oxide reduction degree. This last condition is fundamental to avoid carbon deposition ensuring the presence of oxygen atoms in the iron oxides reticular able to convert the formed carbon into CO and CO_2. A reduction time of 7 minutes seems to be the optimal value to avoid coke deposition leading, however, to a low iron oxide reduction degree and, therefore, poor process efficiency. The addition of 10 wt% MnO_2 powder, physically mixed with Fe_2O_3, promotes the carbon conversion into CO and CO_2 thanks the higher mobility of the oxygen lattice atoms of MnO_2 with respect to iron oxides. Furthermore, the enhanced carbon consumption led to the formation of a gaseous stream in reduction with higher H_2 and CO concentration, able to improve the iron oxide reduction degree without affecting the hydrogen purity. With the addition of 10 wt% of MnO_2 powder, the highest H_2 yields (0.427 ± 0.049 L) and process efficiency (71.9% ± 4.9%) of the study were obtained. However, extended duration test (10 redox cycles) shows that the overall process efficiency sharply

decreased due to the poor thermal stability of hematite powders, making their application at industrial scale impossible.

The synthesis of new and high resistance Fe-based materials having high activity and high thermal resistance is therefore fundamental to make possible the scale-up of the technology. A deep study of the role of structural promoters on the redox performances of iron oxides was performed. The structural promoters studied (Al_2O_3, MgO and CeO_2) showed strong interaction activity with iron oxides forming spinel structures affecting the iron oxides redox properties. Furthermore, the tests demonstrated that ethanol decomposition reactions were highly influenced by the presence of promoters, modyfing the overall reactivity of the process. Among the Fe-based particles tested, 60Fe40Mg was found to be the most favourable one, giving the highest pure H_2 yields among the promoters tested and consuming the lowest amount of ethanol in reduction ($H_2(NL)/EtOH(g) = 3.422$). The thermal stability of each sample was evaluated for 10 consecutive redox cycles, and only the samples with MgO showed a constant activity, leading to a stable H_2 yields at 10 redox cycles (H_2= 0.15 NL and E= 35 %). A peculiar behaviour was registered for the sample with Al_2O_3 added, which suffered from a rapid deactivation, mainly due to the formation of the spinel ($FeAl_2O_4$), inactive in the water splitting reaction.

To deeply study the effect of Al_2O_3 in the iron oxide redox mechanism, sample having different Al_2O_3 concentration (2% and 40% by weight) were tested into 2 and 3 steps CLH configuration, focusing the attention on the effect of increased temperature (750°C) on the Fe/Al interaction and on the thermal resistance of the OCs. The sample with the high amount of Al_2O_3 (60Fe40Al) appeared very active in hydrogen production (E=25%) in the first cycles, but suffering from deactivation due to the spinel formation, which became faster at high temperatures. By decreasing the amount of Al_2O_3 added to 2 % (98Fe2Al) and so limiting the amount of spinel formed, the iron thermal stability was improved, the sample produced stable H_2 yield for 10 cycles with a positive effect on the iron reducibility, especially at 750°C. To fully exploit the high activity of the sample 60Fe40Al registered only in the first few cycles in the 2 steps CLH, the addition of an air oxidation step (3 steps CLH) appeared fundamental to restore the Fe redox activity converting the inert $FeAl_2O_4$ into the separated oxides Fe_2O_3 and Al_2O_3. In this way the successful utilization of this material with a constant process efficiency for 10 cycles was obtained, demonstrating the feasibility of the process with an efficiency of about 30 % at 750 °C.

The addition of 1% of Mn_2O_3 (97Fe2Al1Mn) to the sample having 2% of Al_2O_3 as structural promoter, appeared to be the best solution to maximize the efficiency of the process guarantying the production of pure hydrogen, stable for 10 consecutive cycles. The higher lattice mobility of Mn_xO_y oxygen atoms with respect to the iron oxides allowed to produce pure hydrogen with increased process efficiency even in conditions which were not achievable in absence of this promoter (5.71 mmol of ethanol fed and 750 °C). The positive effect of Mn_xO_y in iron oxides reducibility already demonstrated in the first part of this work was confirmed, the sample 97Fe2Mn1Al appeared more active in hydrogen production than the 98Fe2Al. The enhanced activity of 97Fe2Al1Mn was also tested by feeding higher flow rate of ethanol in the reduction step with the aim of promoting the iron oxides reduction degree with the

increase of the reduction force of the gaseous stream, even at low reaction temperature (675°C). Under these conditions, the highest amount of pure hydrogen was obatined with OCs having 2wt% of Al_2O_3, achieving an average efficiency of the process of 21.52%.

The experimental results obtained with the addition of Mn_2O_3, demonstrated that also the rate of the oxygen exchange of the sample is a key feature to produce pure hydrogen when carbonaceous reductants are used.

The comparison of the TPR profiles with and without promoters highlighted the key role of spinel formation on kinetics of iron oxide reduction. The formation of spinel structures enhances the complexity of iron oxides reduction pathway, increasing the number of steps required to reach the metal phase and so slowing down the overall reduction rate. At low amount of promoter in the sample mass this lag affect can be reduced but not avoided. However, difference among MgO and Al_2O_3 promoters were detected. The formation of $FeAl_2O_4$ spinel slows down the reduction rate in the region of FeO formation due the chemical reaction between the two oxides (FeO and Al_2O_3) while in the case of MgO the spinel $MgFe_2O_4$ appears more reducible. The addition of Mn_2O_3 in the sample 97Fe2Al1Mn overcame the kinetics issues introduced by Al_2O_3, improving the oxygen transfer and avoiding the formation of spinel between Fe/Al.

Based on the promising results obtained with the OCs synthetized by coprecipitation method, a solution for the scale- up of the bench plant with a fixed bed reactor was proposed. The fixed bed reactor configuration allows to perform the redox cycles consecutively in a batch mode, enabling a system design with a low degree of complexity due to the absence of moving parts. However, the use of a porous material with low pressure drops and suitable geometry, is fundamental. The synthesis of a tailored Fe-based foam synthetized by Freeze Casting Technique was demonstrated to be a promising solution, able to confer to the system low pressure drop but also enhanced activity and thermal stability. At constant operative conditions, the FeFOAM sample is 3.14 times more active than the powders with the same chemical composition 98Fe2Al (process efficiency of 22% with respect to 7% with powders).

The work reported in this thesis demonstrated the feasibility to produce directly hydrogen having a purity, in terms of CO amount, ranging from 99.5 in the worst-case scenario to 100 %. The possibility to produce H2 not contaminated by CO was achieved controlling the amount of reductant fed, which was introduced in this work for the first time. The results obtained with the FeFOAM in terms of reactivity and stability makes the proposed system mature for a scale-up of this technology.

12. References

[1] Nations U. The Role of Fossil Fuels in a Sustainable Energy System | United Nations n.d. https://www.un.org/en/chronicle/article/role-fossil-fuels-sustainable-energy-system (accessed October 15, 2022).

[2] Fossil Fuels - Our World in Data n.d. https://ourworldindata.org/fossil-fuels (accessed September 30, 2022).

[3] Okullo SJ, Reynes F, Hofkes MW. Modeling Peak Oil and the Geological Constraints on Oil Production. Undefined 2012. https://doi.org/10.2139/SSRN.2025631.

[4] Bach W. Fossil fuel resources and their impacts on environment and climate. Int J Hydrogen Energy 1981;6:185–201. https://doi.org/10.1016/0360-3199(81)90007-0.

[5] Fossil Fuel - an overview | ScienceDirect Topics n.d. https://www.sciencedirect.com/topics/engineering/fossil-fuel (accessed September 30, 2022).

[6] Demand – Coal 2020 – Analysis - IEA n.d. https://www.iea.org/reports/coal-2020/demand (accessed October 15, 2022).

[7] Jones TH, Willms NB. A critique of Hubbert's model for peak oil. Facets 2018;3:260–74. https://doi.org/10.1139/FACETS-2017-0097.

[8] Eckle P, Burgherr P, Michaux E. Risk of large oil spills: a statistical analysis in the aftermath of Deepwater Horizon. Environ Sci Technol 2012;46:13002–8. https://doi.org/10.1021/ES3029523.

[9] Greenhouse gas emissions - Our World in Data n.d. https://ourworldindata.org/greenhouse-gas-emissions (accessed September 30, 2022).

[10] Effects | Facts – Climate Change: Vital Signs of the Planet n.d. https://climate.nasa.gov/effects/ (accessed September 30, 2022).

[11] CO2 emissions - Our World in Data n.d. https://ourworldindata.org/co2-emissions (accessed October 15, 2022).

[12] IPCC — Intergovernmental Panel on Climate Change n.d. https://www.ipcc.ch/ (accessed October 15, 2022).

[13] Halkos GE, Gkampoura EC. Reviewing usage, potentials, and limitations of renewable energy sources. Energies 2020;13. https://doi.org/10.3390/EN13112906.

[14] World Energy Statistics - Data product - IEA n.d. https://www.iea.org/data-and-statistics/data-product/world-energy-statistics (accessed September 25, 2022).

[15] Das LM. Hydrogen-fueled internal combustion engines. Compend Hydrog Energy 2016:177–217. https://doi.org/10.1016/B978-1-78242-363-8.00007-4.

[16] Hernández JJ, Fúnez C. Editorial of the Special Issue on "Hydrogen technologies and applications." Results Eng 2022;13. https://doi.org/10.1016/j.rineng.2021.100327.

[17] Hydrogen – Analysis - IEA n.d. https://www.iea.org/reports/hydrogen (accessed September 25, 2022).

[18] Abdin Z, Zafaranloo A, Rafiee A, Mérida W, Lipiński W, Khalilpour KR. Hydrogen as an energy

vector. Renew Sustain Energy Rev 2020;120:109620. https://doi.org/10.1016/J.RSER.2019.109620.

[19] De Miranda PE V. Hydrogen Energy: Sustainable and Perennial. Sci Eng Hydrog Energy Technol Hydrog Prod Pract Appl Energy Gener 2019:1–38. https://doi.org/10.1016/B978-0-12-814251-6.00001-0.

[20] Nanda S, N. Vo D-V, Nguyen-Tri P. New dimensions in production and utilization of hydrogen 2020.

[21] Ugurlu A. An emission analysis study of hydrogen powered vehicles. Int J Hydrogen Energy 2020;45:26522–35. https://doi.org/10.1016/J.IJHYDENE.2020.05.156.

[22] Nowotny J, Veziroglu TN. Impact of hydrogen on the environment. Int J Hydrogen Energy 2011;36:13218–24. https://doi.org/10.1016/J.IJHYDENE.2011.07.071.

[23] Holladay JD, Hu J, King DL, Wang Y. An overview of hydrogen production technologies. Catal Today 2009;139:244–60. https://doi.org/10.1016/J.CATTOD.2008.08.039.

[24] Antonini C, Treyer K, Streb A, van der Spek M, Bauer C, Mazzotti M. Hydrogen production from natural gas and biomethane with carbon capture and storage – A techno-environmental analysis. Sustain Energy Fuels 2020;4:2967–86. https://doi.org/10.1039/D0SE00222D.

[25] Katebah M, Al-Rawashdeh M, Linke P. Analysis of hydrogen production costs in Steam-Methane Reforming considering integration with electrolysis and CO2 capture. Clean Eng Technol 2022;10:100552. https://doi.org/10.1016/J.CLET.2022.100552.

[26] Sharma SD. Fuels - Hydrogen Production | Gas Cleaning: Pressure Swing Adsorption. Encycl Electrochem Power Sources 2009:335–49. https://doi.org/10.1016/B978-044452745-5.00307-5.

[27] Sircar S, Golden TC. Purification of hydrogen by pressure swing adsorption. Sep Sci Technol 2000;35:667–87. https://doi.org/10.1081/SS-100100183.

[28] Ruthven DM (Douglas M, Farooq S, Knaebel KS. Pressure swing adsorption 1994:352.

[29] Rödl A, Wulf C, Kaltschmitt M. Assessment of selected hydrogen supply chains-factors determining the overall GHG emissions. Hydrog Supply Chain Des Deploy Oper 2018:81–109. https://doi.org/10.1016/B978-0-12-811197-0.00003-8.

[30] Dawood F, Anda M, Shafiullah GM. Hydrogen production for energy: An overview. Int J Hydrogen Energy 2020;45:3847–69. https://doi.org/10.1016/J.IJHYDENE.2019.12.059.

[31] Kayfeci M, Keçebaş A, Bayat M. Hydrogen production. Sol Hydrog Prod Process Syst Technol 2019:45–83. https://doi.org/10.1016/B978-0-12-814853-2.00003-5.

[32] Technical Contact N, Ruth M. Hydrogen Production Cost Estimate Using Biomass Gasification: Independent Review 2010.

[33] Technical Contact N, Ruth M. Hydrogen Production Cost Estimate Using Biomass Gasification: Independent Review 2010.

[34] COP26: Green hydrogen gets a leg up at climate change meet | Policy Circle n.d. https://www.policycircle.org/environment/green-hydrogen-and-cop26-summit/ (accessed October 15, 2022).

[35] Green hydrogen prices will crash to $1 per kg by 2030: Study | Policy Circle n.d. https://www.policycircle.org/environment/green-hydrogen-prices-crash/ (accessed October

15, 2022).

[36] Hydrogen Transportation - an overview | ScienceDirect Topics n.d. https://www.sciencedirect.com/topics/engineering/hydrogen-transportation (accessed October 16, 2022).

[37] Moradi R, Groth KM. Hydrogen storage and delivery: Review of the state of the art technologies and risk and reliability analysis. Int J Hydrogen Energy 2019;44:12254–69. https://doi.org/10.1016/J.IJHYDENE.2019.03.041.

[38] Elgowainy A. Hydrogen Infrastructure Analysis in Early Markets of FCEVs n.d.

[39] Luise R, Brisse A, Azzaro-Pantel C. Centralised vs. decentralised production and storage: optimal design of a decarbonised hydrogen supply chain with multiple end uses. Comput Aided Chem Eng 2021;50:1775–80. https://doi.org/10.1016/B978-0-323-88506-5.50275-8.

[40] Binod P, Sindhu R, Singhania RR, Vikram S, Devi L, Nagalakshmi S, et al. Bioethanol production from rice straw: An overview. Bioresour Technol 2010;101:4767–74. https://doi.org/10.1016/j.biortech.2009.10.079.

[41] Hou T, Zhang S, Chen Y, Wang D, Cai W. Hydrogen production from ethanol reforming: Catalysts and reaction mechanism. Renew Sustain Energy Rev 2015;44:132–48. https://doi.org/10.1016/j.rser.2014.12.023.

[42] Hepworth TC. Oxygen for Limelight. Nat 1892 471208 1892;47:176–7. https://doi.org/10.1038/047176b0.

[43] David W. Hardie JDP. A History of the Modern British Chemical Industry - David W. Hardie, James D. Pratt - Google Libri. 1969.

[44] Zeng L, Cheng Z, Fan JA, Fan LS, Gong J. Metal oxide redox chemistry for chemical looping processes. Nat Rev Chem 2018 211 2018;2:349–64. https://doi.org/10.1038/s41570-018-0046-2.

[45] Chung EY, Wang WK, Nadgouda SG, Baser DS, Sofranko JA, Fan LS. Catalytic Oxygen Carriers and Process Systems for Oxidative Coupling of Methane Using the Chemical Looping Technology. Ind Eng Chem Res 2016;55:12750–64. https://doi.org/10.1021/ACS.IECR.6B03304/ASSET/IMAGES/MEDIUM/IE-2016-03304J_0018.GIF.

[46] Brady C, Murphy B, Xu B. Enhanced Methane Dehydroaromatization via Coupling with Chemical Looping. Undefined 2017;7:3924–8. https://doi.org/10.1021/ACSCATAL.7B00879.

[47] Giuliano A Di, Capone S, Anatone M, Gallucci K. Chemical Looping Combustion and Gasification: A Review and a Focus on European Research Projects. Ind Eng Chem Res 2022;61:14403–32. https://doi.org/10.1021/ACS.IECR.2C02677.

[48] Bhavsar S, Najera M, Solunke R, Veser G. Chemical looping: To combustion and beyond. Catal Today 2014;228:96–105. https://doi.org/10.1016/J.CATTOD.2013.12.025.

[49] Voitic G, Hacker V. Recent advancements in chemical looping water splitting for the production of hydrogen. RSC Adv 2016;6:98267–96. https://doi.org/10.1039/C6RA21180A.

[50] Wang B, Yan R, Lee DH, Liang DT, Zheng Y, Zhao H, et al. Thermodynamic Investigation of Carbon Deposition and Sulfur Evolution in Chemical Looping Combustion with Syngas. Energy and Fuels 2008;22:1012–20. https://doi.org/10.1021/EF7005673.

[51] Yu Z, Yang Y, Yang S, Zhang Q, Zhao J, Fang Y, et al. Iron-based oxygen carriers in chemical

looping conversions: A review. Carbon Resour Convers 2019;2:23–34. https://doi.org/10.1016/J.CRCON.2018.11.004.

[52] Hu Z, Miao Z, Wu J, Jiang E. Nickel-iron modified natural ore oxygen carriers for chemical looping steam methane reforming to produce hydrogen. Int J Hydrogen Energy 2021;46:39700–18. https://doi.org/10.1016/J.IJHYDENE.2021.09.242.

[53] Das S, Biswas A, Tiwary CS, Paliwal M. Hydrogen production using chemical looping technology: A review with emphasis on H2 yield of various oxygen carriers. Int J Hydrogen Energy 2022;47:28322–52. https://doi.org/10.1016/J.IJHYDENE.2022.06.170.

[54] Luo M, Yi Y, Wang S, Wang Z, Du M, Pan J, et al. Review of hydrogen production using chemical-looping technology. Renew Sustain Energy Rev 2018;81:3186–214. https://doi.org/10.1016/j.rser.2017.07.007.

[55] Isarapakdeetham S, Kim-Lohsoontorn P, Wongsakulphasatch S, Kiatkittipong W, Laosiripojana N, Gong J, et al. Hydrogen production via chemical looping steam reforming of ethanol by Ni-based oxygen carriers supported on CeO2 and La2O3 promoted Al2O3. Int J Hydrogen Energy 2020;45:1477–91. https://doi.org/10.1016/J.IJHYDENE.2019.11.077.

[56] Jiang B, Li L, Bian Z, Li Z, Othman M, Sun Z, et al. Hydrogen generation from chemical looping reforming of glycerol by Ce-doped nickel phyllosilicate nanotube oxygen carriers. Fuel 2018;222:185–92. https://doi.org/10.1016/J.FUEL.2018.02.096.

[57] Li L, Jiang B, Tang D, Zheng Z, Zhao C. Hydrogen Production from Chemical Looping Reforming of Ethanol Using Ni/CeO2 Nanorod Oxygen Carrier. Catal 2018, Vol 8, Page 257 2018;8:257. https://doi.org/10.3390/CATAL8070257.

[58] Huang Z, Deng Z, Chen D, Wei G, He F, Zhao K, et al. Exploration of Reaction Mechanisms on Hydrogen Production through Chemical Looping Steam Reforming Using NiFe2O4 Oxygen Carrier. ACS Sustain Chem Eng 2019;7:11621–32. https://doi.org/10.1021/ACSSUSCHEMENG.9B01557/ASSET/IMAGES/MEDIUM/SC-2019-015572_0012.GIF.

[59] Das S, Biswas A, Tiwary CS, Paliwal M. Hydrogen production using chemical looping technology: A review with emphasis on H2 yield of various oxygen carriers. Int J Hydrogen Energy 2022. https://doi.org/10.1016/J.IJHYDENE.2022.06.170.

[60] Jiang B, Li L, Bian Z, Li Z, Sun Y, Sun Z, et al. Chemical looping glycerol reforming for hydrogen production by Ni@ZrO2 nanocomposite oxygen carriers. Int J Hydrogen Energy 2018;43:13200–11. https://doi.org/10.1016/J.IJHYDENE.2018.05.065.

[61] Silvester L, Antzara A, Boskovic G, Heracleous E, Lemonidou AA, Bukur DB. NiO supported on Al2O3 and ZrO2 oxygen carriers for chemical looping steam methane reforming. Int J Hydrogen Energy 2015;40:7490–501. https://doi.org/10.1016/J.IJHYDENE.2014.12.130.

[62] Cho P, Mattisson T, Lyngfelt A. Defluidization Conditions for a Fluidized Bed of Iron Oxide-, Nickel Oxide-, and Manganese Oxide-Containing Oxygen Carriers for Chemical-Looping Combustion 2006. https://doi.org/10.1021/ie050484d.

[63] Zhu M, Chen S, Soomro A, Hu J, Sun Z, Ma S, et al. Effects of supports on reduction activity and carbon deposition of iron oxide for methane chemical looping hydrogen generation. Appl Energy 2018;225:912–21. https://doi.org/10.1016/J.APENERGY.2018.05.082.

[64] De Vos Y, Jacobs M, Van Driessche I, Van Der Voort P, Snijkers F, Verberckmoes A. Processing and characterization of Fe-based oxygen carriers for chemical looping for hydrogen production. Int J Greenh Gas Control 2018;70:12–21.

https://doi.org/10.1016/J.IJGGC.2018.01.007.

[65] Li M, Qiu Y, Ma L, Cui D, Zhang S, Zeng D, et al. Chemical looping hydrogen storage and production: use of binary ferrite-spinel as oxygen carrier materials. Sustain Energy Fuels 2020;4:1665–73. https://doi.org/10.1039/C9SE01104H.

[66] Qiu Y, Zhang S, Cui D, Li M, Zeng J, Zeng D, et al. Enhanced hydrogen production performance at intermediate temperatures through the synergistic effects of binary oxygen carriers. Appl Energy 2019;252:113454. https://doi.org/10.1016/J.APENERGY.2019.113454.

[67] Hafizi A, Rahimpour MR, Hassanajili S. Hydrogen production by chemical looping steam reforming of methane over Mg promoted iron oxygen carrier: Optimization using design of experiments. J Taiwan Inst Chem Eng 2016;62:140–9. https://doi.org/10.1016/J.JTICE.2016.01.023.

[68] Ismail M, Liu W, Dunstan MT, Scott SA. Development and performance of iron based oxygen carriers containing calcium ferrites for chemical looping combustion and production of hydrogen. Int J Hydrogen Energy 2016;41:4073–84. https://doi.org/10.1016/J.IJHYDENE.2015.11.066.

[69] Chen C, Lee HH, Chen W, Chang YC, Wang E, Shen CH, et al. Study of an Iron-Based Oxygen Carrier on the Moving Bed Chemical Looping System. Energy and Fuels 2018;32:3660–7. https://doi.org/10.1021/ACS.ENERGYFUELS.7B03721/ASSET/IMAGES/LARGE/EF-2017-03721A_0013.JPEG.

[70] Chen S, Xiang W, Xue Z, Sun X. Experimental investigation of chemical looping hydrogen generation using iron oxides in a batch fluidized bed. Proc Combust Inst 2011;33:2691–9. https://doi.org/10.1016/J.PROCI.2010.08.010.

[71] Voitic G, Nestl S, Malli K, Wagner J, Bitschnau B, Mautner FA, et al. High purity pressurised hydrogen production from syngas by the steam-iron process. RSC Adv 2016;6:53533–41. https://doi.org/10.1039/C6RA06134F.

[72] Xu L, Schwebel GL, Knutsson P, Leion H, Li Z, Cai N. Performance of Industrial Residues as Low Cost Oxygen Carriers. Energy Procedia 2017;114:361–70. https://doi.org/10.1016/J.EGYPRO.2017.03.1178.

[73] Hildor F, Mattisson T, Leion H, Linderholm C, Rydén M. Steel converter slag as an oxygen carrier in a 12 MWth CFB boiler – Ash interaction and material evolution. Int J Greenh Gas Control 2019;88:321–31. https://doi.org/10.1016/J.IJGGC.2019.06.019.

[74] Moldenhauer P, Linderholm C, Rydén M, Lyngfelt A. Experimental investigation of chemical-looping combustion and chemical-looping gasification of biomass-based fuels using steel converter slag as oxygen carrier. Undefined 2018.

[75] Yin K, Wang H, Veksha A, Dou X, Khairunnisa Binte Mohamed D, Heberlein S, et al. Oxygen carriers from incineration bottom ash for chemical looping combustion of syngas: Effect of composition on combustion efficiency. Chem Eng J 2021;405:127068. https://doi.org/10.1016/J.CEJ.2020.127068.

[76] Cho WC, Lee D, Kim CH, Cho HS, Kim SD. Feasibility study of the use of by-product iron oxide and industrial off-gas for application to chemical looping hydrogen production. Appl Energy 2018;216:466–81. https://doi.org/10.1016/J.APENERGY.2018.02.078.

[77] Rai C, Bhui B, V P. Techno-economic analysis of e-waste based chemical looping reformer as hydrogen generator with co-generation of metals, electricity and syngas. Int J Hydrogen Energy 2022;47:11177–89. https://doi.org/10.1016/J.IJHYDENE.2022.01.159.

[78] Ma S, Cheng F, Lu P, Song T. Enhanced performance of hematite oxygen carrier by CeO2 for chemical looping hydrogen generation. Int J Hydrogen Energy 2022;47:5130–41. https://doi.org/10.1016/J.IJHYDENE.2021.11.189.

[79] Gu H, Shen L, Xiao J, Zhang S, Song T, Chen D. Iron ore as oxygen carrier improved with potassium for chemical looping combustion of anthracite coal. Combust Flame 2012;159:2480–90. https://doi.org/10.1016/J.COMBUSTFLAME.2012.03.013.

[80] Wang L, Shen L, Jiang S, Liu W. Inhibition of carbon deposition using iron ore modified by K and Cu in chemical looping hydrogen generation. Int J Energy Res 2019;43:167–80. https://doi.org/10.1002/ER.4246.

[81] Wang K, Zhao H, Tian X, Fang Y, Ma J, Zheng C. Chemical-Looping with Oxygen Uncoupling of Different Coals Using Copper Ore as an Oxygen Carrier. Energy and Fuels 2015;29:6625–35. https://doi.org/10.1021/ACS.ENERGYFUELS.5B01377/ASSET/IMAGES/LARGE/EF-2015-01377Y_0010.JPEG.

[82] Chen L, Liu F, S NH, Fan Z, Liu K. Coal Char-fueled Chemical Looping Combustion Use Different Iron-Based Oxygen Carriers. Energy Procedia 2014;63:73–9. https://doi.org/10.1016/J.EGYPRO.2014.11.008.

[83] Huang Z, Zhang Y, Fu J, Yu L, Chen M, Liu S, et al. Chemical looping gasification of biomass char using iron ore as an oxygen carrier. Int J Hydrogen Energy 2016;41:17871–83. https://doi.org/10.1016/J.IJHYDENE.2016.07.089.

[84] Gu Z, Zhang L, Lu C, Qing S, Li K. Enhanced performance of copper ore oxygen carrier by red mud modification for chemical looping combustion. Appl Energy 2020;277:115590. https://doi.org/10.1016/J.APENERGY.2020.115590.

[85] Sridhar D, Tong A, Kim H, Zeng L, Li F, Fan L-S. Syngas Chemical Looping Process: Design and Construction of a 25 kW th Subpilot Unit 2012. https://doi.org/10.1021/ef202039y.

[86] Tong A, Bayham S, Kathe M V., Zeng L, Luo S, Fan LS. Iron-based syngas chemical looping process and coal-direct chemical looping process development at Ohio State University. Appl Energy 2014;113:1836–45. https://doi.org/10.1016/J.APENERGY.2013.05.024.

[87] Chen C, Chen CH, Chang MH, Lee HH, Chang YC, Wen TW, et al. A 30-kWth moving-bed chemical looping system for hydrogen production. Int J Greenh Gas Control 2020;95:102954. https://doi.org/10.1016/J.IJGGC.2019.102954.

[88] Cho WC, Lee DY, Seo MW, Kim SD, Kang KS, Bae KK, et al. Continuous operation characteristics of chemical looping hydrogen production system. Appl Energy 2014;113:1667–74. https://doi.org/10.1016/J.APENERGY.2013.08.078.

[89] Xue Z, Chen S, Wang D, Xiang W. Design and fluid dynamic analysis of a three-fluidized-bed reactor system for chemical-looping hydrogen generation. Ind Eng Chem Res 2012;51:4267–78. https://doi.org/10.1021/IE201052R/ASSET/IMAGES/LARGE/IE-2011-01052R_0007.JPEG.

[90] Herguido J, Peña JA, Carazo E. Experimental assessment of hydrogen separation from H2/CH4 mixtures by the “steam-iron process” in an interconnected circulating fluidized bed reactor. Int J Hydrogen Energy 2014;39:14050–60. https://doi.org/10.1016/J.IJHYDENE.2014.07.006.

[91] Plou J, Durán P, Herguido J, Peña JA. Hydrogen from synthetic biogas by catalyzed MDR and SIP: Screening of catalyst and iron oxide mixtures. Fuel 2015;140:470–6. https://doi.org/10.1016/J.FUEL.2014.09.116.

[92] Herrer M, Plou J, Durán P, Herguido J, Peña JA. Hydrogen from synthetic biogas via SIP using

NiAl2O4 catalyst: Reduction stage. Int J Hydrogen Energy 2015;40:5244–50. https://doi.org/10.1016/J.IJHYDENE.2015.01.063.

[93] Nestl S, Voitic G, Lammer M, Marius B, Wagner J, Hacker V. The production of pure pressurised hydrogen by the reformer-steam iron process in a fixed bed reactor system. J Power Sources 2015;280:57–65. https://doi.org/10.1016/J.JPOWSOUR.2015.01.052.

[94] Xu T, Xiao B, Fu G, Yang S, Wang X. Chemical looping hydrogen production with modified iron ore as oxygen carriers using biomass pyrolysis gas as fuel. RSC Adv 2019;9:39064–75. https://doi.org/10.1039/c9ra08936e.

[95] Xu T, Xiao B, Fu G, Yang S, Wang X. Chemical looping hydrogen production with modified iron ore as oxygen carriers using biomass pyrolysis gas as fuel 2019. https://doi.org/10.1039/c9ra08936e.

[96] Zeng DW, Xiao R, Huang ZC, Zeng JM, Zhang HY. Continuous hydrogen production from non-aqueous phase bio-oil via chemical looping redox cycles. Int J Hydrogen Energy 2016;41:6676–84. https://doi.org/10.1016/J.IJHYDENE.2016.03.052.

[97] Zeng DW, Xiao R, Zhang S, Zhang HY. Bio-oil heavy fraction for hydrogen production by iron-based oxygen carrier redox cycle. Fuel Process Technol 2015;139:1–7. https://doi.org/10.1016/J.FUPROC.2015.08.007.

[98] Tsai YC, Liu LH, Chen DH. Hydrothermal generation of compressed hydrogen gas by iron powders. RSC Adv 2016;6:8930–4. https://doi.org/10.1039/C5RA24274F.

[99] Michiels K, Spooren J, Meynen V. Production of hydrogen gas from water by the oxidation of metallic iron under mild hydrothermal conditions, assisted by in situ formed carbonate ions. Fuel 2015;160:205–16. https://doi.org/10.1016/J.FUEL.2015.07.061.

[100] Cormos CC. Biomass direct chemical looping for hydrogen and power co-production: Process configuration, simulation, thermal integration and techno-economic assessment. Fuel Process Technol 2015;137:16–23. https://doi.org/10.1016/J.FUPROC.2015.04.001.

[101] Cormos CC. Renewable hydrogen production concepts from bioethanol reforming with carbon capture. Int J Hydrogen Energy 2014;39:5597–606. https://doi.org/10.1016/J.IJHYDENE.2014.01.114.

[102] Gopaul SG, Dutta A, Clemmer R. Chemical looping gasification for hydrogen production: A comparison of two unique processes simulated using ASPEN Plus. Int J Hydrogen Energy 2014;39:5804–17. https://doi.org/10.1016/J.IJHYDENE.2014.01.178.

[103] Yan L, Yue G, He B. Thermodynamic analyses of a biomass–coal co-gasification power generation system. Bioresour Technol 2016;205:133–41. https://doi.org/10.1016/J.BIORTECH.2016.01.049.

[104] Edrisi A, Mansoori Z, Dabir B. Using three chemical looping reactors in ammonia production process – A novel plant configuration for a green production. Int J Hydrogen Energy 2014;39:8271–82. https://doi.org/10.1016/J.IJHYDENE.2014.03.119.

[105] Yang Q, Qian Y, Wang Y, Zhou H, Yang S. Development of an Oil Shale Retorting Process Integrated with Chemical Looping for Hydrogen Production 2015. https://doi.org/10.1021/acs.iecr.5b00999.

[106] Zeng L, He F, Li F, Fan LS. Coal-direct chemical looping gasification for hydrogen production: Reactor modeling and process simulation. Energy and Fuels 2012;26:3680–90. https://doi.org/10.1021/EF3003685/ASSET/IMAGES/LARGE/EF-2012-003685_0013.JPEG.

[107] Chen S, Xue Z, Wang D, Xiang W. Hydrogen and electricity co-production plant integrating steam-iron process and chemical looping combustion. Int J Hydrogen Energy 2012;37:8204–16. https://doi.org/10.1016/J.IJHYDENE.2012.02.098.

[108] Sanz A, Nieva D, Dufour J. Steam-Iron process as an alternative to Water Gas Shift reaction in biomass gasification. Int J Hydrogen Energy 2015;40:5074–80. https://doi.org/10.1016/J.IJHYDENE.2015.02.043.

[109] Chen S, Xue Z, Wang D, Xiang W. An integrated system combining chemical looping hydrogen generation process and solid oxide fuel cell/gas turbine cycle for power production with CO2 capture. J Power Sources 2012;215:89–98. https://doi.org/10.1016/J.JPOWSOUR.2012.04.087.

[110] Kathe M V., Empfield A, Na J, Blair E, Fan LS. Hydrogen production from natural gas using an iron-based chemical looping technology: Thermodynamic simulations and process system analysis. Appl Energy 2016;165:183–201. https://doi.org/10.1016/j.apenergy.2015.11.047.

[111] Kang KS, Kim CH, Bae KK, Cho WC, Jeong SU, Kim SH, et al. Modeling a counter-current moving bed for fuel and steam reactors in the TRCL process. Int J Hydrogen Energy 2012;37:3251–60. https://doi.org/10.1016/J.IJHYDENE.2011.11.021.

[112] Sanfilippo D. One-step hydrogen through water splitting with intrinsic CO2 capture in chemical looping. Catal Today 2016;272:58–68. https://doi.org/10.1016/J.CATTOD.2016.02.021.

[113] Yan L, Lim CJ, Yue G, Fang B, He B, Grace JR. Insights into the redox reactivity of an inexpensive Fe-based oxygen carrier. Thermochim Acta 2017;648:52–61. https://doi.org/10.1016/J.TCA.2016.12.003.

[114] Hua X, Wang W, Wang F. Performance and kinetics of iron-based oxygen carriers reduced by carbon monoxide for chemical looping combustion. Front Environ Sci Eng 2015 96 2015;9:1130–8. https://doi.org/10.1007/S11783-015-0821-Y.

[115] Zhu J, Wang W, Hua XN, Wang F, Xia Z, Deng Z. Phase distribution and stepwise kinetics of iron oxides reduction during chemical looping hydrogen generation in a packed bed reactor. Int J Hydrogen Energy 2015;40:12097–107. https://doi.org/10.1016/J.IJHYDENE.2015.07.028.

[116] Hertel C, Heidebrecht P, Sundmacher K. Experimental quantification and modelling of reaction zones in a cyclic watergas shift reactor. Int J Hydrogen Energy 2012;37:2195–203. https://doi.org/10.1016/J.IJHYDENE.2011.10.085.

[117] Ksepko E, Sciazko M, Babinski P. Studies on the redox reaction kinetics of Fe2O3-CuO/Al2O3 and Fe2O3/TiO2 oxygen carriers. Appl Energy 2014;115:374–83. https://doi.org/10.1016/J.APENERGY.2013.10.064.

[118] Jeong MH, Lee DH, Bae JW. Reduction and oxidation kinetics of different phases of iron oxides. Int J Hydrogen Energy 2015;40:2613–20. https://doi.org/10.1016/J.IJHYDENE.2014.12.099.

[119] Murugan A, Thursfield A, Metcalfe IS. A chemical looping process for hydrogen production using iron-containing perovskites. Energy Environ Sci 2011;4:4639–49. https://doi.org/10.1039/c1ee02142g.

[120] Xu T, Xiao B, Fu G, Yang S, Wang X. Chemical looping hydrogen production with modified iron ore as oxygen carriers using biomass pyrolysis gas as fuel. RSC Adv 2019;9:39064. https://doi.org/10.1039/C9RA08936E.

[121] Bleeker MF, Veringa HJ, Kersten SRA. Deactivation of iron oxide used in the steam-iron process to produce hydrogen. Appl Catal A Gen 2009;357:5–17. https://doi.org/10.1016/J.APCATA.2008.12.032.

[122] Fumoto E, Sato S, Takanohashi T. Iron Oxide-Based Catalyst for Catalytic Cracking of Heavy Oil. Iron Ores Iron Oxide Mater 2018. https://doi.org/10.5772/INTECHOPEN.72719.

[123] Zhang Y, Song Z, Yan Y, Zhao X, Sun J, Mao Y, et al. Performance of Fe/SiC catalysts for cracking of toluene under microwave irradiation. Int J Hydrogen Energy 2018;43:7227–36. https://doi.org/10.1016/J.IJHYDENE.2018.02.158.

[124] Phillips VA, Kolbe JL, Opperhauser H. Effect of pH on the growth of Mg(OH)2 crystals in an aqueous environment at 60°C. J Cryst Growth 1977;41:228–34. https://doi.org/10.1016/0022-0248(77)90050-1.

[125] Ciambelli P, Cimino S, Lasorella G, Lisi L, De Rossi S, Faticanti M, et al. CO oxidation and methane combustion on LaAl1−xFexO3 perovskite solid solutions. Appl Catal B Environ 2002;37:231–41. https://doi.org/10.1016/S0926-3373(02)00004-8.

[126] Lloreda-Jurado PJ, Hernández-Saz J, Chicardi E, Paúl A, Sepúlveda R. Pore morphology evolution and atom distribution of doped Fe2O3 foams developed by freeze-casting after redox cycling. J Mater Res Technol 2021;13:1887–98. https://doi.org/10.1016/J.JMRT.2021.06.008.

[127] Graulis S, Chateigner D, Downs RT, Yokochi AFT, Quirós M, Lutterotti L, et al. Crystallography Open Database - An open-access collection of crystal structures. J Appl Crystallogr 2009;42:726–9. https://doi.org/10.1107/S0021889809016690.

[128] Spreitzer D, Schenk J. Reduction of Iron Oxides with Hydrogen—A Review. Steel Res Int 2019;90. https://doi.org/10.1002/SRIN.201900108.

[129] Park J, Zhu RS, Lin MC. Thermal Decomposition of Ethanol. 1. Ab Initio MO/RRKM Prediction of Rate Constant and Product Branching Ratios n.d.

[130] Hormilleja E, Durán P, Plou J, Herguido J, Peña JA. Hydrogen from ethanol by steam iron process in fixed bed reactor. Int J Hydrogen Energy 2014;39:5267–73. https://doi.org/10.1016/j.ijhydene.2014.01.002.

[131] Ibrahim AA, Fakeeha AH, Al-Fatesh AS, Abasaeed AE, Khan WU. Methane decomposition over iron catalyst for hydrogen production. Int J Hydrogen Energy 2015;40:7593–600. https://doi.org/10.1016/j.ijhydene.2014.10.058.

[132] Wang H, Li G, Ma J, Zhao D. The effect of methane decomposition on the formation and magnetic properties of iron carbide prepared from oolitic hematite. RSC Adv 2017;7:3921–7. https://doi.org/10.1039/c6ra26166c.

[133] Zhong Y, Gao J, Wang Z, Guo Z. Influence of Particle Size Distribution on Agglomeration/defluidization of Iron Powders at Elevated Temperature. Undefined 2017;57:649–55. https://doi.org/10.2355/ISIJINTERNATIONAL.ISIJINT-2016-487.

[134] Fang H, Haibin L, Zengli Z. Advancements in development of chemical-looping combustion: A review. Int J Chem Eng 2009;2009. https://doi.org/10.1155/2009/710515.

[135] Stobbe ER, De Boer BA, Geus JW. The reduction and oxidation behaviour of manganese oxides. Catal Today 1999;47:161–7. https://doi.org/10.1016/S0920-5861(98)00296-X.

[136] Sesen FE. Practical reduction of manganese oxide. J Chem Technol Appl 2017;01:3–4. https://doi.org/10.35841/chemical-technology.1.1.26-27.

[137] Lin H, Chen D, Liu H, Zou X, Chen T. Effect of MnO2 crystalline structure on the catalytic oxidation of formaldehyde. Aerosol Air Qual Res 2017;17:1011–20. https://doi.org/10.4209/aaqr.2017.01.0013.

[138] Alizadeh R, Jamshidi E, Zhang G. Transformation of methane to synthesis gas over metal oxides without using catalyst. J Nat Gas Chem 2009;18:124–30. https://doi.org/10.1016/S1003-9953(08)60105-X.

[139] Anacleto N, Ostrovski O, Ganguly S. Reduction of manganese oxides by methane-containing gas. ISIJ Int 2004;44:1480–7. https://doi.org/10.2355/isijinternational.44.1480.

[140] Zhou H, Wei G, Yi Q, Zhang Z, Zhao Y, Zhang Y, et al. Reactivity investigation on chemical looping gasification of coal with Iron-Manganese based oxygen carrier. Fuel 2022;307. https://doi.org/10.1016/J.FUEL.2021.121772.

[141] Hafizi A, Rahimpour MR, Hassanajili S. Hydrogen production via chemical looping steam methane reforming process: Effect of cerium and calcium promoters on the performance of Fe2O3/Al2O3 oxygen carrier. Appl Energy 2016;165:685–94. https://doi.org/10.1016/J.APENERGY.2015.12.100.

[142] Lorente E, Peña JA, Herguido J. Separation and storage of hydrogen by steam-iron process: Effect of added metals upon hydrogen release and solid stability. J Power Sources 2009;192:224–9. https://doi.org/10.1016/J.JPOWSOUR.2008.12.116.

[143] Cui D, Qiu Y, Li M, Ma L, Zhang S, Zeng D, et al. Cu–Fe–Al–O mixed spinel oxides as oxygen carrier for chemical looping hydrogen generation. Int J Hydrogen Energy 2020;45:11908–15. https://doi.org/10.1016/J.IJHYDENE.2020.02.145.

[144] Lorente E, Peña JA, Herguido J. Cycle behaviour of iron ores in the steam-iron process. Int J Hydrogen Energy 2011;36:7043–50. https://doi.org/10.1016/J.IJHYDENE.2011.03.069.

[145] Ma L, Qiu Y, Li M, Cui D, Zhang S, Zeng D, et al. Efficient hydrogen production through the chemical looping redox cycle of YSZ supported iron oxides. Green Energy Environ 2020. https://doi.org/10.1016/j.gee.2020.06.023.

[146] Goula MA, Kontou SK, Tsiakaras PE. Hydrogen production by ethanol steam reforming over a commercial Pd/γ-Al2O3 catalyst. Appl Catal B Environ 2004;49:135–44. https://doi.org/10.1016/j.apcatb.2003.12.001.

[147] Roy S, Mpourmpakis G, Hong DY, Vlachos DG, Bhan A, Gorte RJ. Mechanistic study of alcohol dehydration on γ-Al 2O 3. ACS Catal 2012;2:1846–53. https://doi.org/10.1021/cs300176d.

[148] Hua W, Jin L, He X, Liu J, Hu H. Preparation of Ni/MgO catalyst for CO2 reforming of methane by dielectric-barrier discharge plasma. Catal Commun 2010;11:968–72. https://doi.org/10.1016/J.CATCOM.2010.04.007.

[149] Park Y, Ku H, An JY, Han J, Shin CH, Jeon JK. Effect of MgO promoter on Ru/γ-Al2O3 catalysts for tricyclopentadiene hydrogenation. Catal Today 2020;352:308–15. https://doi.org/10.1016/J.CATTOD.2020.01.003.

[150] Menegazzo F, Pizzolitto C, Ghedini E, Di Michele A, Cruciani G, Signoretto M. Development of La Doped Ni/CeO2 for CH4/CO2 Reforming. C 2018;4:60. https://doi.org/10.3390/c4040060.

[151] Usman M, Daud WMAW. An investigation on the influence of catalyst composition, calcination and reduction temperatures on Ni/MgO catalyst for dry reforming of methane. RSC Adv 2016;6:91603–16. https://doi.org/10.1039/C6RA15256B.

[152] Aziz MAA, Jalil AA, Wongsakulphasatch S, Vo DVN. Understanding the role of surface basic

sites of catalysts in CO2 activation in dry reforming of methane: A short review. Catal Sci Technol 2020;10:35–45. https://doi.org/10.1039/c9cy01519a.

[153] Qi X, Flytzani-Stephanopoulos M. Activity and stability of Cu-CeO2 catalysts in high-temperature water-gas shift for fuel-cell applications. Ind Eng Chem Res 2004;43:3055–62. https://doi.org/10.1021/ie0306170.

[154] Si Z, Weng D, Wu X, Ma Z, Ma J, Ran R. Lattice oxygen mobility and acidity improvements of NiO-CeO 2-ZrO2 catalyst by sulfation for NOx reduction by ammonia. Catal Today 2013;201:122–30. https://doi.org/10.1016/j.cattod.2012.05.001.

[155] Sivaramakrishnan R, Su MC, Michael J V., Klippenstein SJ, Harding LB, Ruscic B. Rate constants for the thermal decomposition of ethanol and its bimolecular reactions with OH and D: Reflected shock tube and theoretical studies. J Phys Chem A 2010;114:9425–39. https://doi.org/10.1021/jp104759d.

[156] Wells RH, Skodje RT. Pathway-Switching Mechanism for Water-Catalyzed Ethanol Decomposition on Cu(111). J Phys Chem C 2020;124:9385–93. https://doi.org/10.1021/acs.jpcc.0c01304.

[157] Zhang H, Wang Z, Li S, Jiao Y, Wang J, Zhu Q, et al. Correlation between structure, acidity and activity of Mo-promoted Pt/ZrO2-TiO2-Al2O3 catalysts for n-decane catalytic cracking. Appl Therm Eng 2017;111:811–8. https://doi.org/10.1016/j.applthermaleng.2016.10.006.

[158] DeWilde JF, Chiang H, Hickman DA, Ho CR, Bhan A. Kinetics and mechanism of ethanol dehydration on γ-Al 2O3: The critical role of dimer inhibition. ACS Catal 2013;3:798–807. https://doi.org/10.1021/cs400051k.

[159] Dajiang M, Yaoqiang C, Junbo Z, Zhenling W, Di M, Maochu G. Catalytic Partial Oxidation of Methane over Ni/CeO2 -ZrO2 -Al2O3. J Rare Earths 2007;25:311–5. https://doi.org/10.1016/S1002-0721(07)60428-1.

[160] Laosiripojana N, Sutthisripok W, Assabumrungrat S. Reactivity of high surface area CeO2 synthesized by surfactant-assisted method to ethanol decomposition with and without steam. Chem Eng J 2007;127:31–8. https://doi.org/10.1016/j.cej.2006.09.020.

[161] Bulfin B, Lowe AJ, Keogh KA, Murphy BE, Lübben O, Krasnikov SA, et al. Analytical model of CeO2 oxidation and reduction. J Phys Chem C 2013;117:24129–37. https://doi.org/10.1021/jp406578z.

[162] Maensiri S, Sangmanee M, Wiengmoon A. Magnesium ferrite (MgFe 2O 4) nanostructures fabricated by electrospinning. Nanoscale Res Lett 2009;4:221–8. https://doi.org/10.1007/s11671-008-9229-y.

[163] Valigi M, Pepe F, Schiavello M. Structure and catalytic activity of iron oxide and magnesium oxide solid solutions. Part 1. - Structural and magnetic investigations. J Chem Soc Faraday Trans 1 Phys Chem Condens Phases 1975;71:1631–41. https://doi.org/10.1039/F19757101631.

[164] Tsvigunov AN, Apolenis A V., Annikov VÉ, Raikova VM. Synthesis of iron aluminates and a new modification of aluminum oxide under shock waves from explosives (Review). Glas Ceram (English Transl Steklo i Keramika) 2007;64:429–36. https://doi.org/10.1007/s10717-007-0106-4.

[165] Amadine O, Essamlali Y, Fihri A, Larzek M, Zahouily M. Effect of calcination temperature on the structure and catalytic performance of copper-ceria mixed oxide catalysts in phenol hydroxylation 2017. https://doi.org/10.1039/c7ra00734e.

[166] Marturano M, Aglietti EF, Ferretti O. α-Al2O3 Catalyst supports for synthesis gas production: influence of different alumina bonding agents on support and catalyst properties. Mater Chem Phys 1997;47:252–6. https://doi.org/10.1016/S0254-0584(97)80060-0.

[167] Liu W, Ismail M, Dunstan MT, Hu W, Zhang Z, Fennell PS, et al. Inhibiting the interaction between FeO and Al 2 O 3 during chemical looping production of hydrogen 2015. https://doi.org/10.1039/c4ra11891j.

[168] Ma S, Chen S, Soomro A, Xiang W. Effects of CeO2, ZrO2, and Al2O3 Supports on Iron Oxygen Carrier for Chemical Looping Hydrogen Generation. Energy and Fuels 2017;31:8001–13. https://doi.org/10.1021/ACS.ENERGYFUELS.7B01141.

[169] Wang Q, Li W, Hung I, Mentink-Vigier F, Wang X, Qi G, et al. Mapping the oxygen structure of γ-Al2O3 by high-field solid-state NMR spectroscopy. Nat Commun 2020 111 2020;11:1–9. https://doi.org/10.1038/s41467-020-17470-4.

[170] Spray-dried Fe/Al2O3 as a carbon carrier for COx-free hydrogen production via methane cracking in a fluidized bed process. Chem Eng J 2020;398:125612. https://doi.org/10.1016/J.CEJ.2020.125612.

[171] Kidambi PR, Cleeton JPE, Scott SA, Dennis JS, Bohn CD. Interaction of Iron Oxide with Alumina in a Composite Oxygen Carrier during the Production of Hydrogen by Chemical Looping. Energy Fuels 2012;26:603–17. https://doi.org/10.1021/ef200859d.

[172] Elrefaie FA, Smeltzer WW. Thermodynamics of the system iron-aluminum-oxygen between 1073 K and 1573 K. Metall Trans B 1983 141 1983;14:85–93. https://doi.org/10.1007/BF02654055.

[173] Shafiefarhood A, Hamill JC, Neal LM, Li F. Methane partial oxidation using FeOx@La0.8Sr0.2FeO3−δ core–shell catalyst – transient pulse studies. Phys Chem Chem Phys 2015;17:31297–307. https://doi.org/10.1039/C5CP05583K.

[174] de Diego LF, Ortiz M, Adánez J, García-Labiano F, Abad A, Gayán P. Synthesis gas generation by chemical-looping reforming in a batch fluidized bed reactor using Ni-based oxygen carriers. Chem Eng J 2008;144:289–98. https://doi.org/10.1016/J.CEJ.2008.06.004.

[175] Doğu TI. The Importance of Pore Structure and Diffusion in the Kinetics of Gas-Solid Non-catalytic Reactions: Reaction of Calcined Limestone with SO2. Chem Eng J 1981;21:213–22. https://doi.org/10.1016/0300-9467(81)80005-6.

[176] Monazam ER, Siriwardane R. Hydrogen Production by Steam Oxidation of Reduced CaFe2O4 during Chemical Looping Coal Gasification: Equilibrium and Kinetic Analysis. Energy and Fuels 2018;32:10398–407. https://doi.org/10.1021/ACS.ENERGYFUELS.8B01650/ASSET/IMAGES/LARGE/EF-2018-01650P_0015.JPEG.

[177] Sarkar R, Sohn HY. Interaction of ferrous oxide with alumina refractory under flash ironmaking conditions. Ceram Int 2019;45:15417–28. https://doi.org/10.1016/j.ceramint.2019.05.040.

[178] Liu W, Ismail M, Dunstan MT, Hu W, Zhang Z, Fennell PS, et al. Inhibiting the interaction between FeO and Al2O3 during chemical looping production of hydrogen. RSC Adv 2015;5:1759–71. https://doi.org/10.1039/C4RA11891J.

[179] Al-Shankiti IA, Bayon A, Weimer AW. Reduction kinetics of hercynite redox materials for solar thermochemical water splitting. Chem Eng J 2020;389:124429. https://doi.org/10.1016/j.cej.2020.124429.

[180] Bachirou GL, Shuai Y, Zhang J, Huang X, Yuan Y, Tan H. Syngas production by simultaneous splitting of H2O and CO2 via iron oxide (Fe3O4) redox reactions under high-pressure. Int J Hydrogen Energy 2016;41:19936–46. https://doi.org/10.1016/J.IJHYDENE.2016.09.053.

[181] Yüzbasi NS, Armutlulu A, Huthwelker T, Abdala PM, Müller CR. Na-β-Al2O3 stabilized Fe2O3 oxygen carriers for chemical looping water splitting: correlating structure with redox stability. J Mater Chem A 2022;2:10692–700. https://doi.org/10.1039/d1ta10507h.

[182] Chiu P-C, Ku Y, Wu Y-L, Wu H-C, Kuo Y-L, Tseng Y-H. Characterization and Evaluation of Prepared Fe 2 O 3 /Al 2 O 3 Oxygen Carriers for Chemical Looping Process. Aerosol Air Qual Res 2014;14:981–90. https://doi.org/10.4209/aaqr.2013.04.0135.

[183] Voitic G, Hacker V. Recent advancements in chemical looping water splitting for the production of hydrogen 2016. https://doi.org/10.1039/c6ra21180a.

[184] Yüzbasi NS, Kierzkowska A, Müller C. Development of Fe2O3-based, Al2O3-stabilized Oxygen Carriers using Sol-gel Technique for H2 Production via Chemical Looping. Energy Procedia 2017;114:436–45. https://doi.org/10.1016/J.EGYPRO.2017.03.1186.

[185] Carabineiro SAC, Bogdanchikova N, Pestryakov A, Tavares PB, Fernandes LSG, Figueiredo JL. Gold nanoparticles supported on magnesium oxide for CO oxidation. Nanoscale Res Lett 2011;6:1–6. https://doi.org/10.1186/1556-276X-6-435.

List of abbreviations

AR : Air Reactor

BDCL: Biomass Direct Chemical Looping

BPG: Biomass Pyrolysis Gas

CLC: Chemical Looping Combustion

CLH: Chemical Looping Hydrogen

CLR : Chemical Looping Reforming

CLWS: Chemical Looping Water Splitting

COP26: 26th UN Climate Change Conference of the Parties

FC : Freeze-Casting

FBR : Fixed bed reactor

FR : Fuel Reactor

GH_2: gaseous hydrogen

GHG: greenhouse gases emissions

GOD : Gas Oxidation Degree

IBA :Incineration Bottom Ashes

IEA: International Energy Agency

IPCC: International panel of Climate Change

ITRI: Industrial Technology Research Institute

LH_2: liquid hydrogen

MBR : Moviment Bed Reactor

OCs : Oxygen Carriers

PEMFC: Proton Exchange Membrane Fuel Cells

PSA: Pressure Swing Adsorption

Ro : Oxygen Transport Capacity

SIP : Steam Iron Process

SMR : Steam Methane Reforming

TGA: Thermogravimetric Analysis

TPR: Temperature Programmed Reduction

TWh : terawatt hour

WGS : Water Gas Shift

13. List of Figures

List of Tables